120
44

Characterization and Modeling of Magnetic Materials and Structures

by

Abdulhameed Yousef Al-Mazroo

Dissertation submitted to the Faculty of the

Virginia Polytechnic Institute and State University

in partial fulfillment of the requirements for the degree of

Ph.D.

in

Electrical Engineering

APPROVED:

Aicha A. Elshabini-Riad,
Chairperson

Ioannis M. Besieris

Werner E. Kohler

Sedki M. Riad

Vatche Vorperian

December, 1988

Blacksburg, Virginia

Characterization and Modeling of Magnetic Materials and Structures

by

Abdulhameed Yousef Al-Mazroo

Aicha A. Elshabini-Riad, Chairperson

Electrical Engineering

(ABSTRACT)

This dissertation presents methods for wideband characterization and modeling of magnetic materials and structures over a wide frequency range (dc to a few GHz). A method for modeling the thick film inductor structures at high frequencies is presented in this dissertation. The thick film inductor under test is printed and located in shunt connection at the end of a reference transmission line. Time Domain Reflectometry (TDR) technique is used to measure the response waveform from the inductor under test. The response from a short circuit at the location of the inductor is acquired as the reference waveform. The two acquired waveforms are then transformed into the frequency domain using the Fast Fourier Transform algorithm (FFT). The reflection coefficient is then computed as the ratio between the Fourier Transforms of the response and reference waveforms. From the information contained, the complex impedance of the structure under study can be calculated. This information is used for modeling that structure by fitting the data to the network model using the computer network analysis program. Experimental and simulated response waveforms are compared and brought to a close match by changing the model components values.

A cavity-like sample holder filled with ferrite material is proposed in this dissertation to measure the complex permeability of the magnetic material filling this cavity. The cavity walls are deposited on a coaxially shaped sample using thick film techniques. The reflection coefficient from the cavity under study is measured by adapting the cavity to the end of a transmission line. The full field analysis of this proposed configuration is used to determine a relationship between the complex permeability of the ferrite material and the measured reflection coefficient. The method of moments is used to achieve this task. Computer simulation experiments are performed to test the sensitivity of the technique and to predict the performance over the desired frequency range. Actual experimentation as well as verifications of these measurements are conducted to verify the merit of the proposed technique.

Acknowledgements

All gratitudes are due to the creator (Allah) for all what I have accomplished in this life.

I would like to thank Dr. A. Elshabini-Riad for the time she spent offering help, suggestions, and information throughout this work. Thanks are due to the members of my advisory committee, Dr. S. Riad, Dr. I. Besieris, Dr. V. Vorperian, and Dr. W. Kohler, for their comments. Special gratitudes are due to Dr. S. Riad for his help and assistance in the area of Time Domain. Thanks are also due to Dr. M. Saed for the discussions regarding the field analysis.

I would like to thank my father and mother for their love, moral help, and prayers. Also thanks are due to my brothers and sisters for their love and support.

Finally, I would like to thank my wife who spent 7 years away from her family and relatives during my graduate study.

Table of Contents

CHAPTER I

INTRODUCTION

Wideband characterization and modeling of thick film magnetic materials and structures at high frequencies are discussed in this dissertation. A review covering the development of the techniques used to characterize and model thick film magnetic materials and structures is also discussed. This review covers about 5 decades of techniques development to measure the relative complex permeability of materials in the frequency range 100 MHz - 15 GHz.

During the last decade and half, thick film inductors became the focus of many researchers with the goal to improve the performance of these inductors. At high frequencies, particularly those in the upper radio frequency (RF) range, the use of thick film printed inductors becomes an attractive alternative to the use of discrete wire coils. The single layer coil (spiral) constructed on ceramic substrate is the most common structure of thick film inductors. Enhancement of the inductor's properties dictates the use of ferromagnetic paste. In such structure, coils are stacked vertically with intervening ferrite layers to yield these improved properties. Lack of accurate knowledge of specifications and characteristics of available ferrite pastes limits their useful usage.

Modeling and characterization of thick film inductor structures at high frequencies is presented in this research. Time Domain Reflectometry (TDR) technique is used in the electrical characterization and modeling of thick film inductors under test over the frequency range from DC to a few GHz. The thick film inductor under test is printed and located at the end of a reference transmission line. The Modified Transient Circuit Analysis Program (MTCAP) is used to obtain a simulated response waveform. Experimental and simulated response waveforms are compared and brought to a close match by changing the model components values.

A cavity-like sample holder filled with ferrite material is proposed in this dissertation. This cavity is used for the wideband characterization of some ferrite materials. The cavity walls are deposited on a coaxially shaped sample. In this new proposed configuration, there is no need to cut or shape the sample precisely to fit in an existing structure which is a problem many conventional configurations found in the literature has suffered from. The proposed structure is adapted to the end of a transmission line and the reflection coefficient, $S_{11}(j\omega)$, is measured. The relative complex permeability, μ_r^*, is then derived from the measured reflection coefficient.

The full field analysis of this new configuration is used to find a relationship between the complex permeability of the ferrite and the reflection coefficient. The method of moments is used to achieve this task. Computer simulation of the cavity is performed and presented. Experiments are performed to verify the technique and the computer program used to get the characterization results. Characterization results for two ferrite materials are also presented. These results are obtained using Time Domain measurements and Frequency Domain measurements.

This dissertation is includes five chapters, chapter I, is an introductory chapter. The next chapter, chapter II, presents a review covering the development of the techniques used to characterize and model thick film magnetic materials and structures. Chapter III discusses the use of TDR techniques in modeling thick film inductor structures. In chapter VI, the concept of the coaxial cavity adapted to the end of a transmission line is presented. Finally, chapter V summarizes the major findings of the dissertation.

CHAPTER II

REVIEW OF CHARACTERIZATION AND MODELING OF MAGNETIC MATERIALS AND STRUCTURES

2.1 CHARACTERIZATION OF MAGNETIC MATERIALS

2.1.1 INTRODUCTION

This review will cover about 5 decades of development in the techniques used to measure the relative complex permeability of materials in the frequency range 100 MHz - 15 GHz. Some of the methods to be surveyed are used to measure the relative complex permittivity of materials as well. Materials are characterized by their relative complex permeability and permittivity μ_r^* and ε_r^*, respectively.

$$\mu_r^*(j\omega) = \mu'_r - j\mu''_r \tag{2.1}$$

and

$$\varepsilon_r^*(j\omega) = \varepsilon'_r - j\varepsilon''_r \tag{2.2}$$

In these equations , the real parameters μ', (relative permeability) and permittivity (dielectric constant) ε', describe the storage of magnetic energy and electric energy, respectively. The loss factors μ'', and ε'', represent the dissipation. They are measured in reference to vacuum.

Methods of characterization are categorized according to the type of the sample holder. The following is a summary of the methods investigated,

1. Transmission line methods, which includes
    - Frequency domain, sweep measurements
    - Frequency domain, single measurements
    - Time domain
2. Resonator method

The next subsection will cover the transmission line methods, while the last subsection will explain the resonator method.

2.1.2 TRANSMISSION LINE METHODS

(1) INTRODUCTION

Transmission lines in their different forms are used in the characterization of the permeability of materials. Material under test is placed at different locations

along the line for different methods. Voltage Standing Wave Ratio, VSWR, impedance, and reference and response waveforms are some of the parameters measured to obtain μ_r^*. Most of the methods are performed in the frequency domain, while one method investigated is performed in the time domain.

(2) FREQUENCY DOMAIN, SWEEP MEASUREMENTS

Weir [1] used a computer controlled network analyzer to measure the permeability of a network consisting of ferrite material under test. Using this method measurements can be done in the band 100 MHz to 18 GHz with steps of 20 KHz or less. The transmission line section may either be a waveguide or a TEM transmission line. The network is illustrated schematically in Figure (2.1). The reflection coefficient, S_{11}, at the air to ferrite interface and the transmission coefficient, S_{21}, through the material, are found at reference planes 1 and 2. From the complex reflection and transmission coefficients, the computer associated with the network analyzer determines the real and imaginary parts of the permeability of the ferrite.

Referring to Figure (2.1), the propagation factor for a wave propagating through the material is defined as [2],

$$P = e^{-(\alpha+j\beta)l} \tag{2.1}$$

where α is the attenuation constant, β is the phase constant given by,

$$\beta = \frac{2\pi}{\lambda_g} \tag{2.2}$$

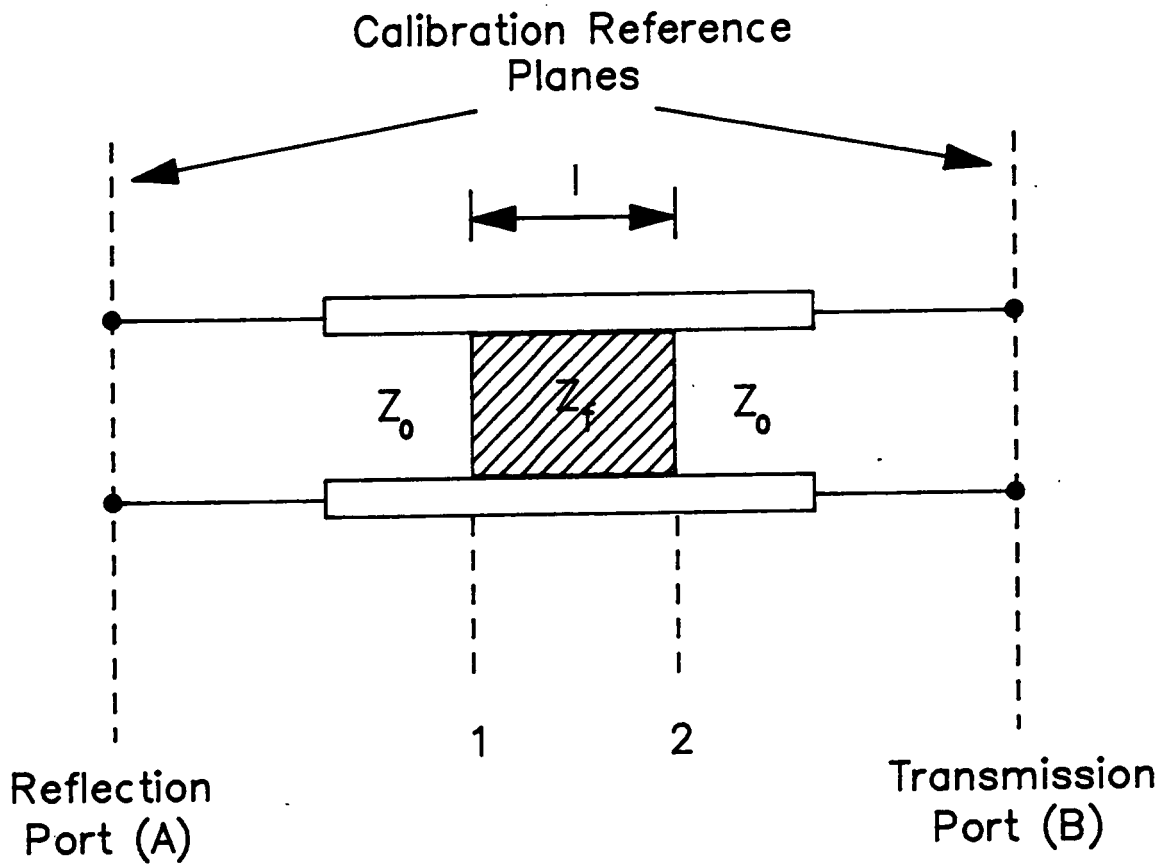

Figure (2.1). Transmission line section containing ferrite material.

The reflection coefficient, Γ, at the interface between the air-filled transmission line and the ferrite-filled line when the material sample is infinite in length may be found from the measured reflection, S_{11}, and transmission, S_{21}, coefficients for a sample of finite length, l, as,

$$\Gamma = \chi \pm \sqrt{\chi^2 - 1} \tag{2.3}$$

where

$$\chi = \frac{S_{11}^2 - S_{21}^2 + 1}{2S_{11}} \tag{2.4}$$

The propagation factor, P, can, in turn, be found from S_{11}, S_{21}, and Γ as,

$$P = \frac{S_{11} + S_{21} - \Gamma}{1 - (S_{11} + S_{21})\Gamma} \tag{2.5}$$

The complex permeability, μ_r^*, can be determined from P and Γ as,

$$\mu_r^* = \frac{1 + \Gamma}{\Lambda(1 - \Gamma)\sqrt{\frac{1}{\lambda_0^2} - \frac{1}{\lambda_c^2}}} \tag{2.6}$$

where

$$\frac{1}{\Lambda^2} = -\left[\frac{1}{2\pi l}\ln\left(\frac{1}{P}\right)\right]^2 \tag{2.7}$$

where λ_0 is the free space wavelength and λ_c is the cutoff wavelength of the transmission line section ($\lambda_c = \infty$ for a TEM line). Equation (2.7) has an infinite number of roots since the imaginary part of the logarithm of a complex quantity is equal to the angle of the complex value plus $2\pi n$, where n is equal to the integer of (l/λ_g).

Equation (2.7) is ambiguous because the phase of the propagation factor P does not change when the length of the material is increased by a multiple of wavelength. Weir [1] in his same paper described a method to resolve the ambiguity.

Barry [3] used the same general method introduced by Weir [1] with strip transmission line as the fixture into which blocks of the material to be measured may be inserted easily. The measurement technique was developed to characterize accurately the electromagnetic properties of certain ceramic ferrites in the 0.5 to 5.5 GHz frequency band. Figure (2.2) represents a strip transmission line of length $2l + t$ loaded in the center with ferrite of length t. Region II of the stripline, loaded with the sample material has a characteristic impedance of Z given by,

$$Z = Z_0\sqrt{\frac{\overset{*}{\mu_r}}{\overset{*}{\varepsilon_r}}} \tag{2.8}$$

where Z_0 is the characteristic impedance of the free space regions I and III. Similarly, the propagation constant in region II is given by,

$$k = k_0\sqrt{\overset{*}{\mu_r}\overset{*}{\varepsilon_r}} \tag{2.9}$$

The complex reflection coefficient at the plane boundaries between regions I and II, R, is given by,

$$R = \frac{Z - Z_0}{Z + Z_0} \tag{2.10}$$

Equations (2.8)-(2.10) are solved to yield

$$\overset{*}{\mu_r} = \frac{k}{k_0}\left(\frac{1+R}{1-R}\right) \tag{2.11}$$

Thus, knowing k and R enables μ'_r to be calculated. The values of k and R are evaluated using the measured scattering parameters, S_{11} and S_{21}, as

$$kt = \cos^{-1}\left(\frac{e^{-j4k_0l} + S_{21}^2 - S_{11}^2}{2e^{-j2k_0l}S_{21}} \right) \tag{2.12}$$

and

$$R = \frac{S_{11}}{\left(e^{-j2k_0l} - S_{21}e^{-jkt}\right)} \tag{2.13}$$

Knowing t, the length of the material sample, equation (2.11) is used to evaluate the relative complex permeability of the ferrite under test.

(3) FREQUENCY DOMAIN, SINGLE MEASUREMENTS

Rado [4] used a short circuited coaxial line as the sample holder. A thin toroidal ferrite specimen of rectangular cross section was inserted into the coaxial line at a position of large H (and small E) adjacent to the short circuited termination. Measurements using this method were done over the frequency range (~ 10 MHz to 10 GHz). By solving the appropriate boundary value problem, it can be shown that for a TEM type propagation,

$$\mu'_r = 1 + (s/d) \tag{2.14}$$

and

$$\mu''_r = \left(\frac{1}{\xi} - \frac{1}{\xi'} \right) \frac{\lambda_0}{2\pi d} \tag{2.15}$$

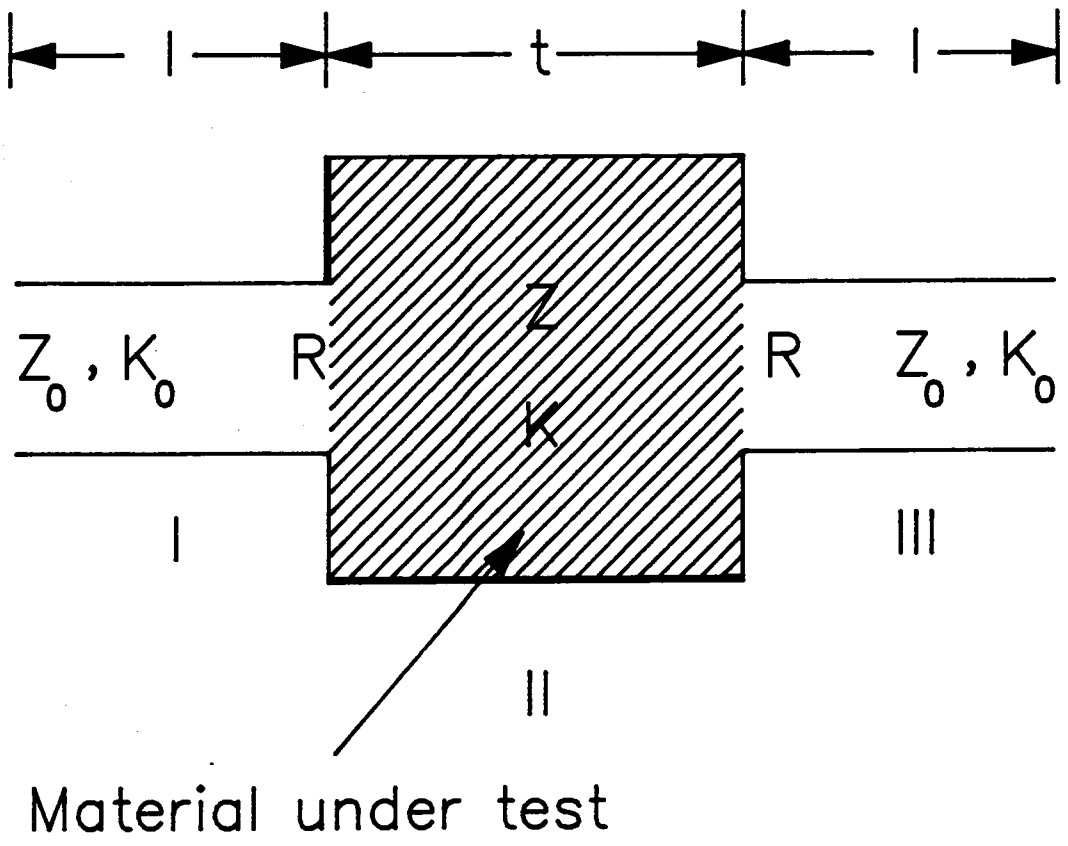

Figure (2.2). Strip transmission line loaded with the material under test.

where d is the thickness of the sample, λ_0 is the free space wavelength, and s is the displacement of the voltage minimum from it's (previously observed) location in the shorted empty line. The quantities ξ and ξ' denote the voltage standing wave ratio of the actual line and the empty line, respectively. Equations (2.14) and (2.15) apply only if the relation

$$|\varepsilon_r^* \mu_r^*|^{1/2}(2\pi d/\lambda_0) << 1 \tag{2.16}$$

is satisfied, and if the coaxial conductors are highly conducting.

(4) TIME DOMAIN

Nicolson and Ross [5] presented in their paper a method for determining the relative complex permeability, μ_r^*, of linear materials in the frequency domain by a single time domain measurement. Their method is based upon the measurement of the totally reflected voltage waveform and the totally transmitted waveform of a sample of material inserted in coaxial transmission line. Measurements using this method were achieved in the range 400 MHz - 10 GHz with 400 MHz resolution. Figure (2.3) illustrates the coaxial line with the material sample inserted. If the thickness of the sample, d, was infinite, then the reflection coefficient of a wave incident on the interface from the air-filled line would be given by,

$$\Gamma = \frac{\sqrt{\mu_r^*/\varepsilon_r^*} - 1}{\sqrt{\mu_r^*/\varepsilon_r^*} + 1} \tag{2.17}$$

For finite d, the transmission coefficient between faces A and B of the slab may be written as,

$$z = \exp[-j(\omega d/c)\sqrt{\mu_r^* \varepsilon_r^*}] \tag{2.18}$$

The scattering coefficients S_{21} and S_{11} of the slab can be obtained from the Fourier analysis of the reflected, transmitted, and reference waveforms as,

$$S_{21} = \frac{(1-\Gamma^2)z}{1-\Gamma^2 z^2} \tag{2.19}$$

and

$$S_{11} = \frac{(1-z^2)\Gamma}{1-\Gamma^2 z^2} \tag{2.20}$$

Equations (2.19) and (2.20) are solved for μ_r^* to obtain the following results,

$$\mu_r^* = \sqrt{c_1 c_2} \tag{2.21}$$

where

$$c_1 = \left(\frac{1+\Gamma}{1-\Gamma}\right)^2 \tag{2.22}$$

$$c_2 = -\left\{\frac{c}{\omega d}\ln\left(\frac{1}{z}\right)\right\}^2 \tag{2.23}$$

2.1.3 RESONATOR METHOD

Courtney [6] presented in his paper a method that utilizes a resonant post technique for characterizing magnetic materials at microwave frequencies. The structure used was a finite length of a cylindrical ferrite rod waveguide shorted by

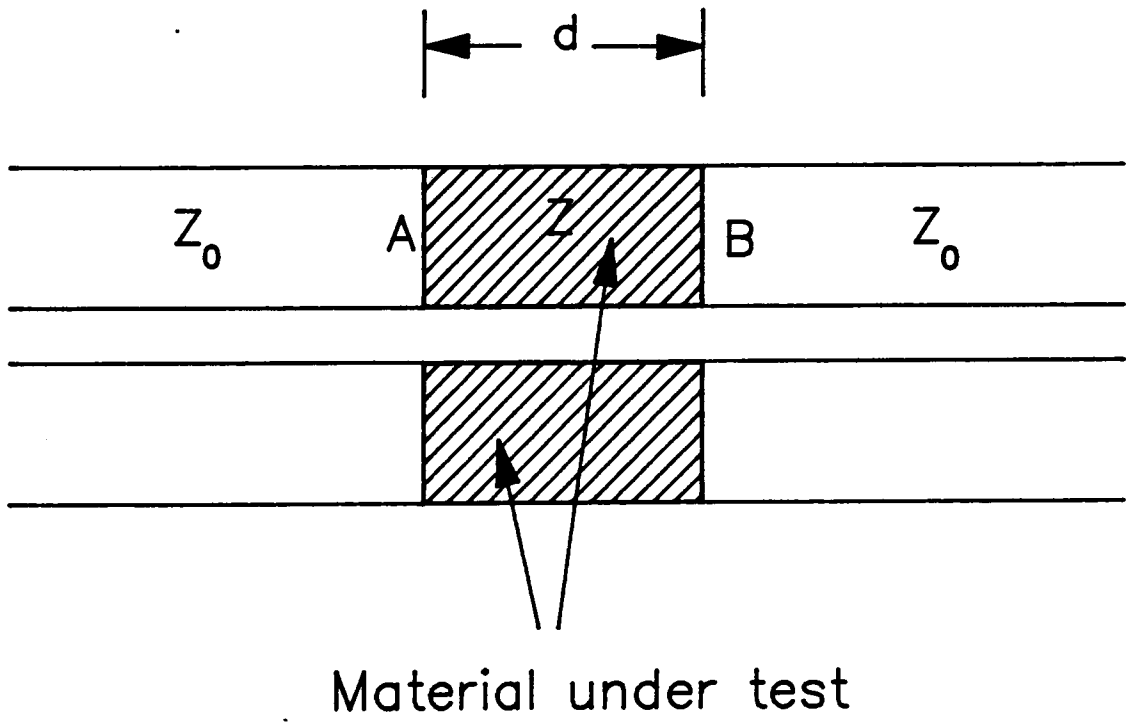

Figure (2.3). A coaxial line with annular disk of material to be measured inserted.

placing conducting plates at each end of the rod and turning the transmission line into a resonator, Figure (2.4). This method is good for measurements up to 8 GHz. Since the TE_{011} mode is easier to identify, it was proposed that this mode be used for the permeability measurements. The characteristic equation for the TE_{011} mode becomes,

$$\frac{\alpha_m J_0(\alpha_m)}{J'_0(\alpha_m)} = -\mu_r^* \beta_m \frac{K_0(\beta_m)}{K'_0(\beta_m)} \tag{2.24}$$

where J_0 and K_0 are Bessel functions of the first and second kind, respectively, and

$$\alpha_m = \frac{\pi D f_m}{c} \left[\mu_r^* \varepsilon_r^* - (c/2Lf_m)^2\right]^{1/2} \tag{2.25}$$

and

$$\beta_m = \frac{\pi D f_m}{c} \left[(c/2Lf_m)^2 - 1\right]^{1/2} \tag{2.26}$$

where f_m is the resonant frequency of the TE_{011} mode, D is the diameter, L is the length of the ferrite specimen, and α_m and β_m are the first roots of the characteristic equation.

2.2 MODELING OF MAGNETIC STRUCTURES

Ahmed et. al. [7] presented in their paper a method for wideband modeling of thick film printed components. The method used for such modeling is based on time domain measurement techniques. Frequency dependent parameters of microstrip and coplanar transmission line structures printed on ceramic substrates are calculated and physically based models of printed resistors and capacitors (for the coplanar geometry) are obtained. Time domain techniques applied to model thick

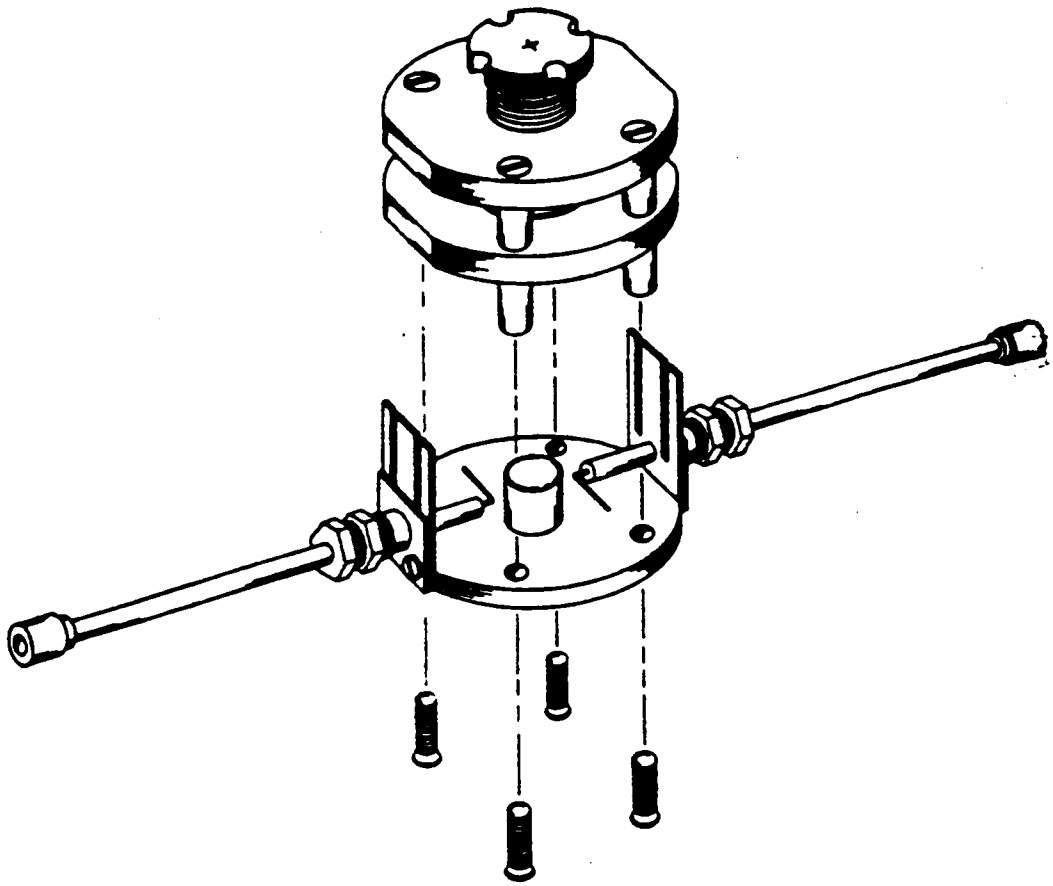

Figure (2.4). Exploded view of the ferrite post resonator showing the sample and the probes in position.

film printed components involve either of the two methods, namely, the Time Domain Reflection (TDR) and the Time Domain Transmission (TDT). In the TDR method, the reflection from the component's input port is observed as the response waveform and is used to calculate input port's reflection-transfer-function of the component under test. While for the TDT method, the response waveform is the transmitted one observed at the output port of the component and is used to calculate it's through-transmission-transfer-function.

Riad and Toscano [8] dealt in their paper with the modeling of the thick film inductors at high frequencies. A 50 ohm thick film coplanar transmission line is constructed such that the inductor is connected in shunt with the line. They used Time Domain Reflectometry, TDR, in acquiring reference and response waveforms, $v_{ref}(t)$ and $v_{resp}(t)$, respectively. The TDR response waveform is used to construct the initial model. The rest of the modeling process is achieved in the frequency domain, where some more information are acquired and more components are added to the model. The information can be obtained by examining other waveforms, such as the phase and magnitude of the reflection coefficient.

The reference and response waveforms are transformed into the frequency domain using the Fast Fourier Transform algorithm, FFT. The reflection coefficient of the line termination $\rho(j\omega)$ is computed as the ratio between the two Fourier Transforms,

$$\rho(j\omega) = \frac{V_{resp}(j\omega)}{V_{ref}(j\omega)} \tag{2.27}$$

The impedance of the line termination, $Z(j\omega)$, is computed as,

$$Z(j\omega) = Z_o \frac{1+\rho(j\omega)}{1-\rho(j\omega)} \tag{2.28}$$

where Z_o is the reference line's characteristic impedance.

Next, they used the response waveform to get an estimate of the series inductance and resistance. The following two equations are used,

$$L = (R_{dc} + Z_0)\,\tau \tag{2.29}$$

where τ is the time constant of the response waveform and R_{dc}, the dc-resistance of the inductor, is given by,

$$R_{dc} = Z_o \frac{1+\rho(0)}{1-\rho(0)} \tag{2.30}$$

where $\rho(0)$ is the reflection coefficient at dc. The following equation is used to get an estimate of a shunt capacitance, C,

$$C = \frac{1}{2\pi f_o L} \tag{2.31}$$

where f_o is the self resonance frequency of the coil. These initial values are used to compute the model impedance which is compared to the measured one of the inductor. If a good match between the computed and measured impedances occurs, then these initial values of the model components are the final ones. Otherwise, the initial value(s) of one or more component(s) are changed until a match occurs.

CHAPTER III

CHARACTERIZATION AND MODELING OF MULTILAYER INDUCTORS

3.1 INTRODUCTION

During the last decade and half, thick film inductors became the focus of many researchers [19 - 24]. The goal of these researchers is to improve the performance of thick film inductors. At high frequencies, particularly those in the upper radio frequency (RF) range, the use of thick film printed inductors becomes an attractive alternative to the use of discrete wire coils. At these frequencies, thick film inductors have low parasitics and they also have short lead lengths, satisfying a favorable component function. Limited usage of thick film inductors can be attributed to many factors. These factors include limited layer thickness achievable in one print, lack of tunability, large physical size, lack of accurate knowledge of the characteristics of multilayer printed inductor, lack of accurate knowledge of specifications and characteristics of available ferrite pastes, and relatively low permeability of commercially available ferrite pastes.

The single layer coil (spiral) constructed on ceramic substrate is the most known structure of thick film inductors. The flat spiral can be either square or circular in shape. An increase in the inductance value of the element necessitates a corresponding increase in the number of turns. As a result, the coil occupies a fairly large area on the substrate surface.

Current designs involve two or more layers of spiral coils stacked vertically with a dielectric layer in between for isolation. An opened window in the isolation material permits the proper connection between the two coils. Such structure has proven to yield improved properties of thick film inductors. Further enhancement of the inductor's properties dictates the use of ferromagnetic paste. In such structure, coils are stacked vertically with intervening ferrite layers to yield these improved properties [25]. The effect is further enhanced using thicker ferrite layers.

This chapter deals with the modeling and characterization of three thick film inductor structures at high frequencies. The first structure is the single layer coil, the second structure is the multilayer coil separated by dielectric material, and the third structure is the multilayer coil separated by ferrite material. Modeling procedures and final results of the first two structures will be presented, while modeling procedures and results of the third structure will be examined thoroughly. Observing the progress of the modeling work, one can notice the increasing complexity of the electrical network as inductor structure becomes more complex.

In this work, the Time Domain Reflectometry (TDR) technique will be used in the electrical characterization and modeling of thick film inductors over the frequency range from DC to a few GHz. The thick film inductor under test will be printed and

located at the end of a reference transmission line. For the first inductor structure, the TDR waveforms will be acquired and used to calculate the termination's reflection coefficient $\rho(j\omega)$. And, a model will be constructed and compared to the experimental measurements.

For the second and third inductor structures, the TDR waveforms will be acquired and the response waveform will be used to develop an equivalent model for the inductor under test. The Modified Transient Circuit Analysis Program (MTCAP) will be used to obtain a simulated response waveform. Experimental and simulated response waveforms will be compared and brought to a close match by changing the model components values. Frequency domain measurements are used to analyze the accuracy of the model developed in the time domain. For verification purposes, the driving point impedance of the final inductor model will be computed and compared to its value as measured using a Vector Impedance Meter.

This chapter consists of six sections, with Section 3.1 being the introduction. Section 3.2 explains the construction process of the three inductor structures as well as it describes the equipment and materials used in the experimentation. The Time Domain Reflectometry technique is described in section 3.3. In section 3.4, the modeling techniques of the three structures are explained. Section 3.5 presents the results of the modeling of the three inductor structures. Accuracy as well as validity of the modeling technique are discussed in section 3.5. Finally, a concluding section, section 3.6, summarizes the main findings of the chapter.

3.2 EQUIPMENT, MATERIALS, AND ELEMENTS STRUCTURE

Thick film technology equipment and materials used in the construction of the thick film inductor is the subject of the first subsection. The next subsection discusses the structure and mount of the thick film inductor on the transmission line for wideband characterization and modeling.

3.2.1 EQUIPMENT AND MATERIALS

An AMI Presco automatic screen printer machine model 435 is used in the printing operation using the single print mode. A screen breakaway distance of 20 mils is used in the printing process. The transmission line as well as the coils are printed using a 325 screen mesh size with a 90° angle, and overall dimensions of 8″ × 10″. The ferrite and dielectric layers are printed using a 250 screen mesh size, with a 90° angle, and overall dimensions of 8″ × 10″ . The samples are dried in a Blue M oven POM-206B-1 for 15 minutes at 150° C, and then they are fired in a BTU four-zone belt furnace. The total firing cycle is of the order of 60 minutes, with a 10 minutes at a peak temperature of 850°C.

DuPont Silver-Palladium (Ag-Pd) 6134 conductor paste is used in the printing of the single layer coil. DuPont Gold (Au) conductor paste 4019, and DuPont 5704 dielectric paste are used in the printing of the multilayer coil separated by dielectric material. In addition, Electro Scientific Laboratories (ESL) ferrite paste EX-2000, used in the cavity construction to be discussed in the next chapter, and Silver (Ag) conductor paste D9912-F are also used in the printing of the multilayer coil separated by

ferrite material. 3″ × 3″ × 0.025″ , 96% alumina substrates manufactured by Coors Porcelain are used to produce these inductor structures.

The HP-4193A Vector Impedance Meter is used to measure the impedance of each inductor in the frequency range 0.5 MHz - 100 MHz. Time domain measuring equipment are fully described in section 3.3.

3.2.2 INDUCTOR STRUCTURE AND MOUNT

The construction of the single layer coil is achieved by depositing one conductor layer directly onto the substrate. The conductor film is allowed to settle, dry, and fire. In order to form the multilayer coil separated by dielectric material, the first coil is deposited. Then two dielectric layers are deposited on the lower spiral coil. The dielectric material is allowed to be dried and fired. One more conductor layer is printed on top of the dielectric layers, then it is dried and fired. The dielectric layers possess an opening to allow for the interconnection between the bottom and top coils. The winding of each coil is achieved in such a manner so as the resultant magnetic fluxes are superimposed.

The structure of the multilayer coil separated by ferrite material consists of the following,

1. Two ferrite layers are deposited directly on the substrate. Each ferrite layer is dried and fired separately after deposition.

2. The first conductor layer forming the lower coil is printed on top of the two ferrite layers. The film is dried and fired.

3. Two more ferrite layers are added on top of the first conductor layer. Drying and firing is achieved in a similar way to step 1. Both ferrite layers possess an opening to allow for the interconnection between the bottom and top coils.

4. The second conductor layer is printed last, thus forming the top coil. The coil is dried and fired.

The coils are 3 turns each with an inner diameter of 80 mils and an outer diameter of 400 mils. The conductor width is 30 mils and the separation gap between the turns is 10 mils wide. Figure (3.1) illustrates the multilayer inductor structure.

A 50 ohm thick film coplanar transmission line is constructed such that the inductor is connected in shunt with the line. For the single coil structure, the connection is achieved by connecting the line's central strip to one end of the inductor, while the other end of the inductor is connected to the ground planes of the line with gold wire bonds. For the multilayer structures using dielectric and ferrite materials, this can be achieved by connecting the central strip of the line to the outside end of the bottom coil, and the split ground of the line to the outside end of the top coil, Figure (3.2). The line is printed at the same time as the lower coil for the multilayer structures, while for the single layer case, it is printed at the same time as the coil itself.

The coplanar line ground is 200 mils wide, while the center conductor is 30 mils wide. Finally, to make this structure feasible for measurement, the coplanar line

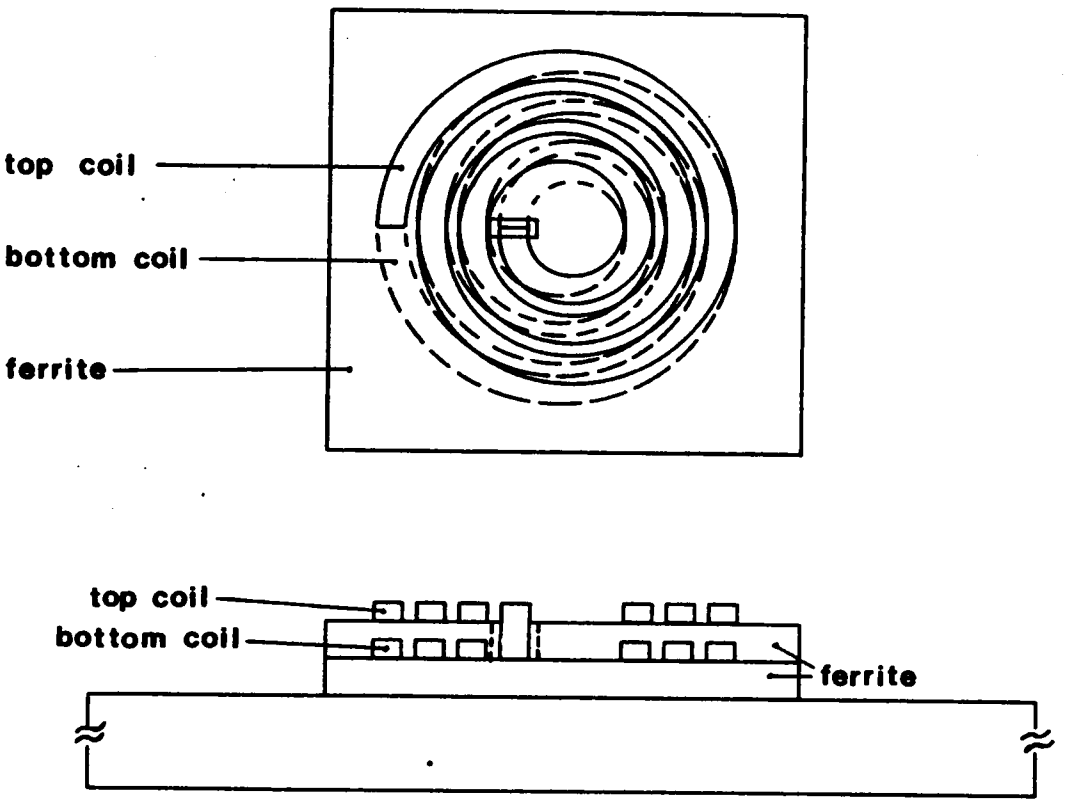

Figure (3.1). Multilayer inductor structure.

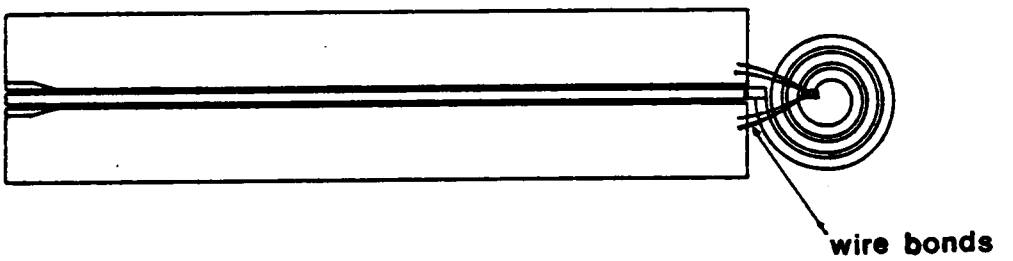

Figure (3.2). Top view of multilayer inductor.

is adapted to any coaxial line via a modified omni spectra SMA End Launch Jack (MELJ).

3.3 TIME DOMAIN REFLECTOMETRY TECHNIQUE

Time Domain Reflectometry techniques are used in this work to characterize and model thick film inductor structures. Figure (3.3) illustrates the TDR setup used for the measurement of the reference and reflected waveforms. This setup consists of an oscilloscope interfaced for data acquisition to a personal computer, a feedthrough sampling head, and a pulse generator. A 50 ohm reference coaxial transmission line is connected between the feedthrough sampling head and the MELJ end of the inductor. The pulse generator used is a tunnel diode with spectral contents covering the band from DC to about 12 GHz.

In order to measure the reflection coefficient $\rho(j\omega)$, two waveforms are acquired, a response waveform and a reference waveform. The response waveform $v_{resp}(t)$ is the reflection from the multilayer inductor terminating the line. The reference waveform $v_{ref}(t)$ is the negative of the reflection from a short circuit located in front of the inductor (at the connection between the inductor and the coplanar line). The negative sign results from the fact that an ideal short circuit has a reflection coefficient $\rho(j\omega)$ equals to -1. A copper wedge is used to implement the required short. Both the reference and response waveforms are stored in a form suitable for later use in the computer simulation program. Figure (3.4) shows both $v_{ref}(t)$ and $v_{resp}(t)$ of the multilayer inductor separated by dielectric material in a 10 ns display window.

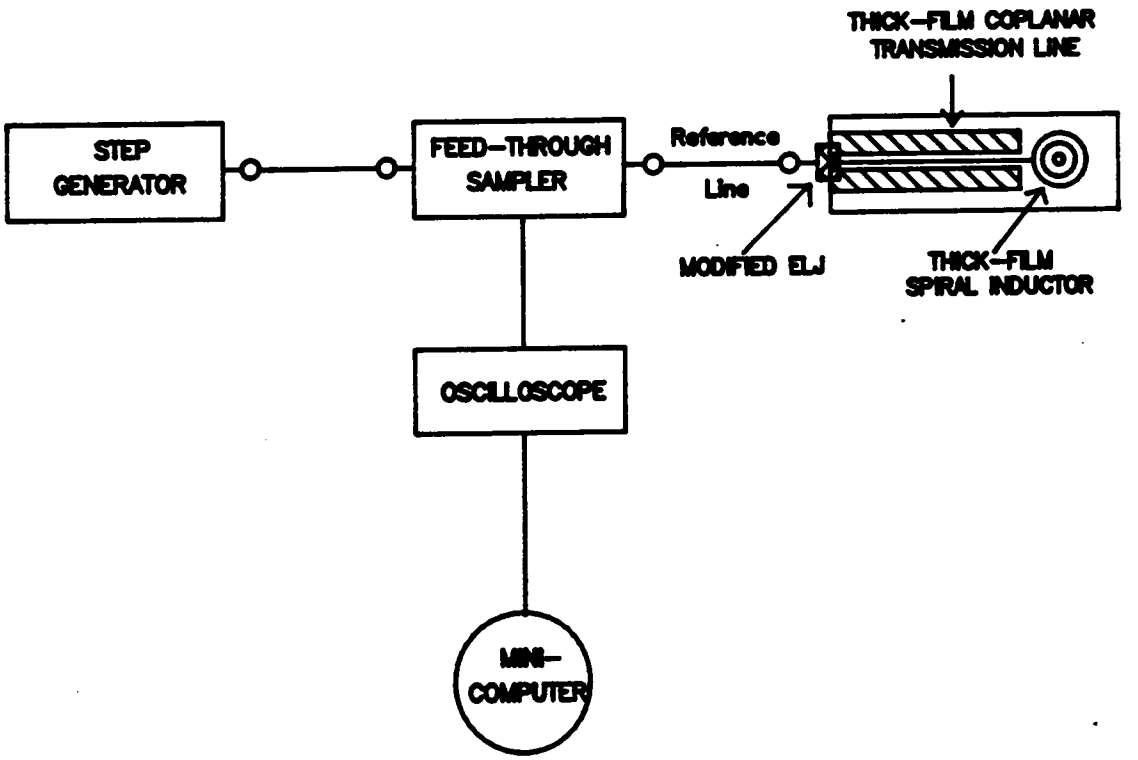

Figure (3.3). TDR setup.

Figure (3.5) shows the same waveforms for the multilayer inductor separated by ferrite material. Both inductors are modeled in section (3.4).

The termination's reflection impulse response, $h_\rho(t)$, is related to $v_{ref}(t)$ and $v_{resp}(t)$ by the following equation,

$$v_{resp}(t) = v_{ref}(t) * h_\rho(t) \tag{3.1}$$

where (*) denotes the convolution operation. The two acquired waveforms are then transformed into the frequency domain using the Fast Fourier Transform algorithm, FFT. The reflection coefficient, $\rho(j\omega)$, which is the Fourier Transform of $h_\rho(t)$, is then computed as the ratio between the Fourier Transforms of the response and reference waveforms,

$$\rho(j\omega) = \frac{V_{resp}(j\omega)}{V_{ref}(j\omega)} \tag{3.2}$$

When an incident pulse in a TDR setup encounters a discontinuity, the pulse reflects back and the magnitude and polarity of the reflected pulse depends upon the type of that discontinuity. This means that the TDR response waveform provides a relevant information about every discontinuity in a transmission system. This last fact results in the use of TDR in the modeling of the inductor structures. Examining the TDR response, the waveforms dips, peaks, oscillations, and relaxations are recognized as reflections caused by distributed and/or lumped discontinuities on the transmission line. In order to model these discontinuities, one has to be familiar with the behavior of ideal component discontinuities and their combinations in a similar TDR setup.

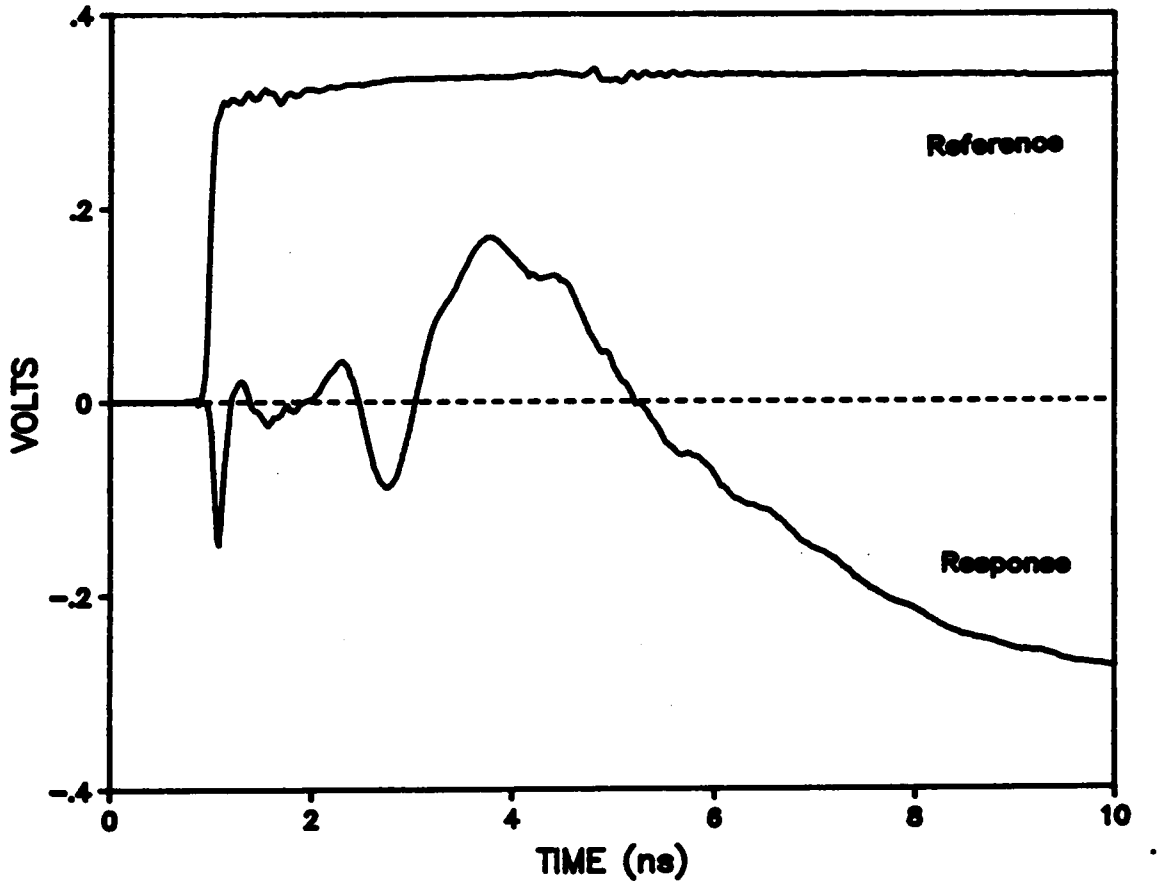

Figure (3.4). Reference and response waveforms for a multilayer inductor separated by dielectric material.

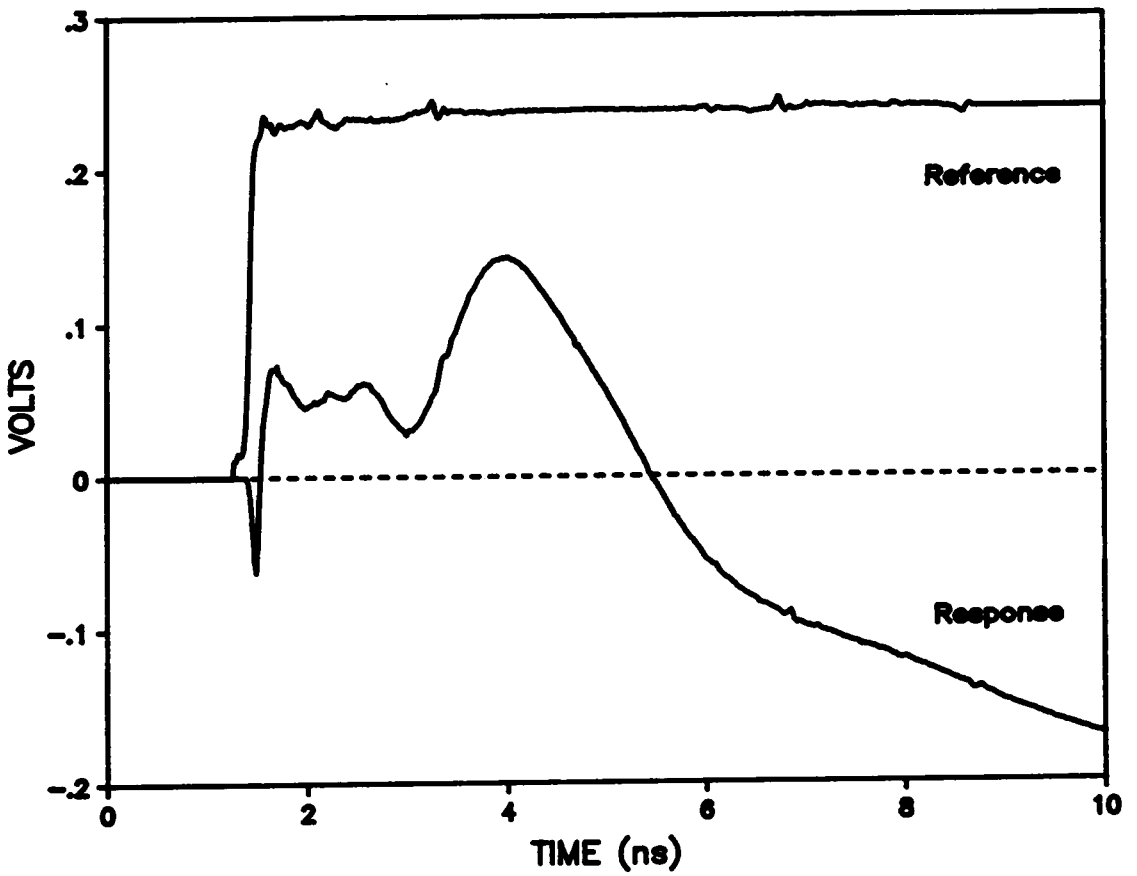

Figure (3.5). Reference and response waveforms for a multilayer inductor separated by ferrite material.

A series inductive discontinuity, for example, causes the incident pulse to initially see an open circuit, so that the pulse is reflected. Shortly after, the inductor starts charging and causing the reflected pulse to come down to the transmission line's characteristic impedance level. Figure (3.6a) illustrates the reflected pulse from a typical inductive discontinuity. On the other hand, if the incident pulse encounters a capacitive discontinuity, the pulse initially sees a short circuit, and as the capacitor starts charging the pulse magnitude decays to the transmission line's characteristic impedance level. A reflected pulse from a typical capacitive discontinuity is illustrated in Figure (3.6b).

3.4 COMPONENT MODELING

3.4.1 INTRODUCTION AND DESCRIPTION OF PROCESS

The aim of this section is to present the process used for modeling both single layer as well as multilayer coils. The next subsection is concerned with the single layer coil modeling. And, the last subsection presents the modeling procedure of the multilayer inductor in it's two types, dielectric filled form and ferrite filled form. For the single layer coil, TDR is used in acquiring reference and response waveforms, $v_{ref}(t)$ and $v_{resp}(t)$, respectively. The TDR response waveform $v_{resp}(t)$ is used to construct the initial model. The rest of the modeling process is achieved in the frequency domain, where some more information can be acquired and more components can be added to the model. The information can be obtained by examining other waveforms, such as the phase and magnitude of the reflection coefficient. For the multilayer inductor, TDR is used in acquiring the reference and response waveforms. The TDR

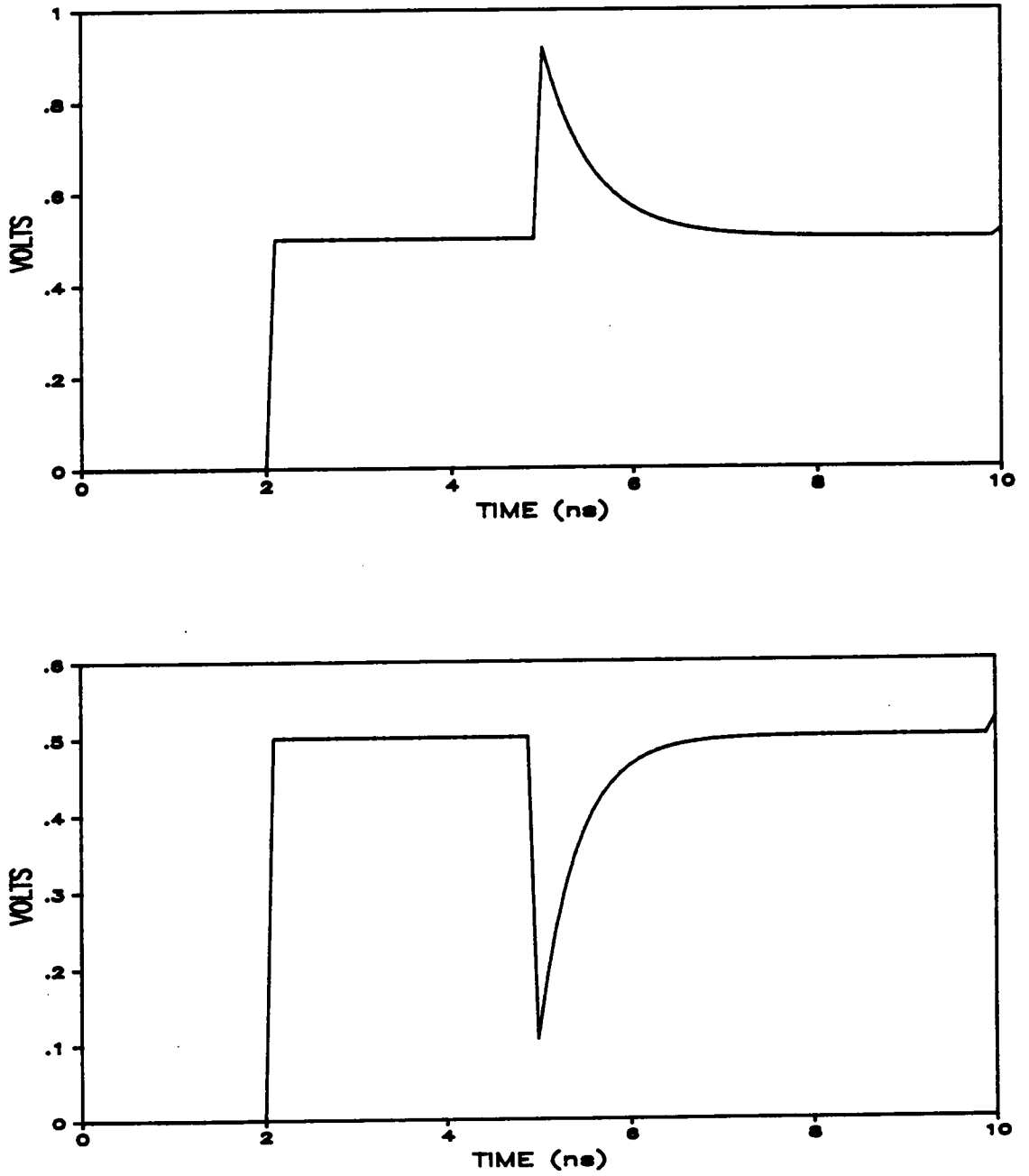

Figure (3.6). Reflected waveform from (a) inductive discontinuity (b) capacitive discontinuity.

response waveform, $v_{resp}(t)$, is used in deducing the initial inductor model. The TDR reference and response waveforms are used in obtaining the final model.

3.4.2 MODELING OF THE SINGLE LAYER COIL

The modeling process for the single layer coil starts with the TDR measurements conducted where $v_{ref}(t)$ and $v_{resp}(t)$ are acquired. Then both waveforms are transformed into the frequency domain using the Fast Fourier Transform algorithm, FFT. The reflection coefficient of the line termination $\rho(j\omega)$ is computed as the ratio between the two Fourier Transforms, equation (3.2),

$$\rho(j\omega) = \frac{V_{resp}(j\omega)}{V_{ref}(j\omega)} \tag{3.2}$$

$\rho(j\omega)$ can be expressed as,

$$\rho(j\omega) = \frac{Z(j\omega) - Z_o}{Z(j\omega) + Z_o} e^{j\phi} \tag{3.3}$$

where, $Z(j\omega)$ is the impedance of the line termination, Z_o is the reference line's characteristic impedance, and ϕ is an arbitrary phase constant. This arbitrary phase is due to arbitrary time delays present in the TDR measurement. This can result from either time drifts in the TDR system and/or from the difference in the physical location of the electrical planes of reflection of the reference and the response waveforms. To compute $Z(j\omega)$ without errors, one has to account for and correct that delay. This can be achieved by shifting the response waveform until the reflections from the

connectors occur at the same time for both the reference and response waveforms [10]. Thus, one can write,

$$Z(j\omega) = Z_o \frac{1 + \rho_{corrected}(j\omega)}{1 - \rho_{corrected}(j\omega)} \tag{3.4}$$

where $\rho_{corrected}(j\omega)$ is the reflection coefficient after the correction of the delay.

Analyzing the response waveform, $v_{resp}(t)$, one can determine the dominant elements forming the inductor model. One can add more components to this initial model by examining other waveforms. As an example, the real and imaginary parts of the inductor impedance, $Z(j\omega)$, may suggest one more component because of a resonance that is occurring at some frequency. The model stays the same as far as it's components are concerned. Values of these components are to be changed until a good match between the model impedance $Z_{model}(j\omega)$ and $Z(j\omega)$ of the inductor has been accomplished.

When a final model is obtained, the next step is to assign initial values to the model components. Typically, equations (3.5), (3.6), (3.7), and (3.8) are used to assign these initial values. A series inductance, L, is given by,

$$L = \frac{Z_i(f_l)}{2\pi f_l} \tag{3.5}$$

where $Z_i(f_l)$ is the imaginary component of the inductor impedance at the lowest frequency data point, f_l. A series resistance, R, has two components, a dc resistance, R_{dc}, and skin effect resistance, R_{se}. The dc resistance is given by,

$$R_{dc} = Z_o \frac{1 + \rho_{corrected}(0)}{1 - \rho_{corrected}(0)} \tag{3.6}$$

where $\rho_{corrected}(0)$ is the reflection coefficient at dc. The skin effect resistance is given by,

$$R_{se} = \frac{n\,a\,\pi}{W} \sqrt{\frac{\pi f \mu}{\sigma}} \tag{3.7}$$

where n is the number of turns, W is the width of the single coil in mils, a is the average radius in mils, μ is the permeability in Henries per meter, f is the frequency in Hertz, and σ is the conductivity in S/m. A shunt capacitance, C, is given by,

$$C = \frac{1}{2\pi f_o L} \tag{3.8}$$

where f_o is the self resonance frequency of the coil.

The real part of the model impedance is computed, using the initial values, and plotted together with the measured real part of the impedance of the inductor being modeled. The same is done to the imaginary part of the impedance. If a good match between the computed and measured real and imaginary parts of the impedance occurs, then these initial values of the model components are the final ones. Otherwise, the initial value(s) of one or more component(s) are changed until a match occurs.

3.4.3 MODELING OF THE MULTILAYER COIL

From the TDR measurements as well as any knowledge of the physical nature and structure of the inductor, one can deduce the initial model. From the shape of $v_{resp}(t)$, the response waveform, one can assume that each dip, peak, or relaxation is being a result of a distributed and/or lumped discontinuity the incident pulse has encountered. One or more component(s) connected in series or in shunt with the transmission line can model any type of a discontinuity. So it is suggested that one has to be familiar with the responses of ideal discontinuities as well as the response of their combinations. Figure (3.6) illustrates the behavior of some of the ideal components of a model.

The attractive feature of modeling in the time domain is that, modeling of one discontinuity does not affect the modeling of a second one that takes place at a later time. Thus, one can model each discontinuity individually. The fact mentioned previously has one exception noticed by the author. This exception is that, if a transmission line is added to model a particular delay between two discontinuities, the line's addition to the model may affect the accuracy of modeling the preceding discontinuity.

After the construction of the model, one has to assign initial values to the model components. These initial values can be estimated using some approximate relations which have been developed for modeling simple discontinuities. These relations can be applied provided that one can assume that 1) the test pulse can be approximated by a step with a ramp leading edge; 2) the discontinuity component values are small; and 3) the measurements of the TDR waveforms are not band-

limited [26]. For a small series inductive discontinuity, L, or a small shunt capacitive discontinuity, C, on a transmission line of characteristic resistance of R_o, these approximate relations are of the form [26],

$$L = 2\, e_L\, R_o\, m \tag{3.9}$$

and

$$C = \frac{2\, e_C}{R_o\, m} \tag{3.10}$$

where m is the slope of the test pulse's leading edge and e_L and e_C are the amplitudes of the inductive and capacitive reflections, respectively.

The final step in the modeling process is to simulate the measured response waveform. The initial values of the model constructed previously are assigned using equations (3.9) and (3.10). The model with these values is then used in the Modified Transient Circuit Analysis Program, (MTCAP), to simulate the inductor under test [27]. The acquired reference waveform, $v_{ref}(t)$, is used to excite the model so as to get a simulated TDR response waveform. The simulated and experimental response waveforms are then plotted together. Starting with the first discontinuity any discrepancy between the two waveforms at any discontinuity is corrected by changing the value of the model parameter at that discontinuity. More components may be added to fit a small part of the simulated response waveform to it's corresponding part of the inductor response waveform. Values of the model components are changed in an iterative fashion until a close match between the experimental and the simulated response waveforms takes place.

3.5 MODELING RESULTS, ACCURACY, AND VALIDITY

3.5.1 INTRODUCTION

In this section, examples of modeling actual single layer and multilayer coils are presented. Results of the modeling, including; the electrical model, final values of the model components, and the closest match possible between the corresponding waveforms are illustrated and/or tabulated. The fourth subsection discusses the accuracy of the modeling process. The validity of the modeling process is the subject of the last subsection.

3.5.2 RESULTS OF SINGLE LAYER COILS MODELING

A typical response waveform from a single layer coil, illustrated in Figure (3.7), suggests that the model consists of a series inductance and a series resistance. Figures (3.8) and (3.9) illustrate the magnitude and the phase components of $\rho(j\omega)$ for the response waveform shown in Figure (3.7) for the single layer coil. The phase components suggests that a shunt capacitor must be added to the model. Thus, the final model of the inductor is illustrated in Figure (3.10). Initial values of the model components are computed using equations (3.4), (3.5), (3.6), and (3.7). Final values of the model components tabulated in Table (3.1) are obtained after achieving the close match needed between both components of the impedance. These results are illustrated in Figures (3.11) and (3.12), has been accomplished.

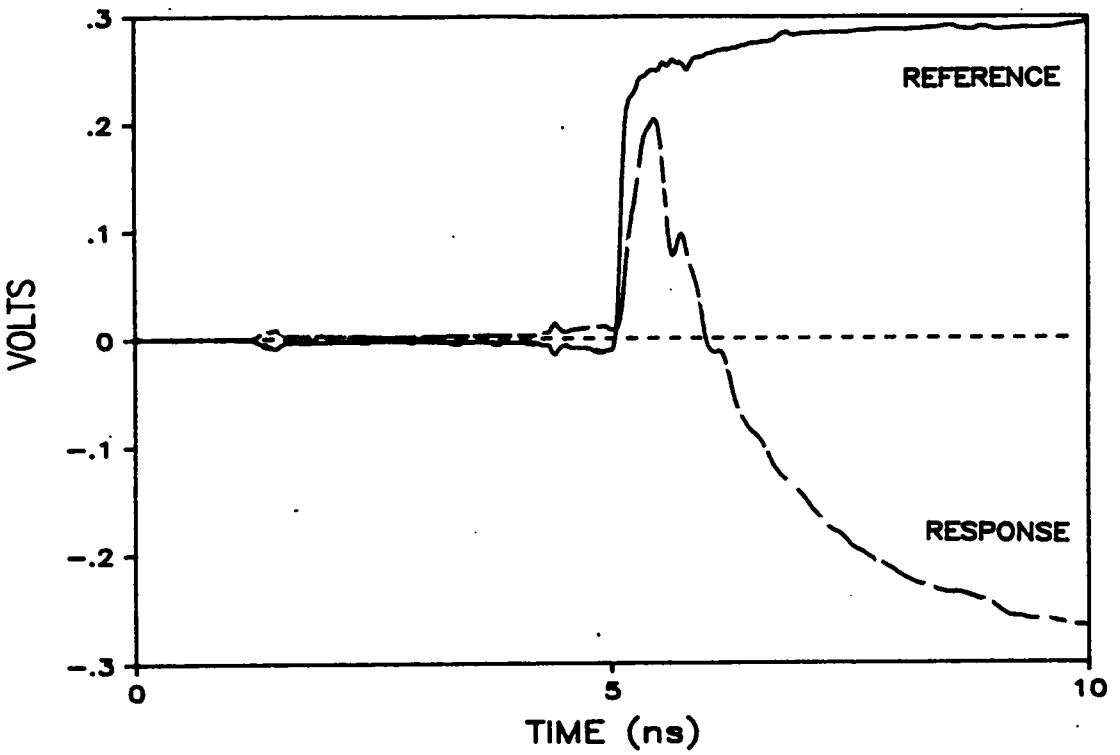

Figure (3.7). Reference and response waveforms for a single layer coil.

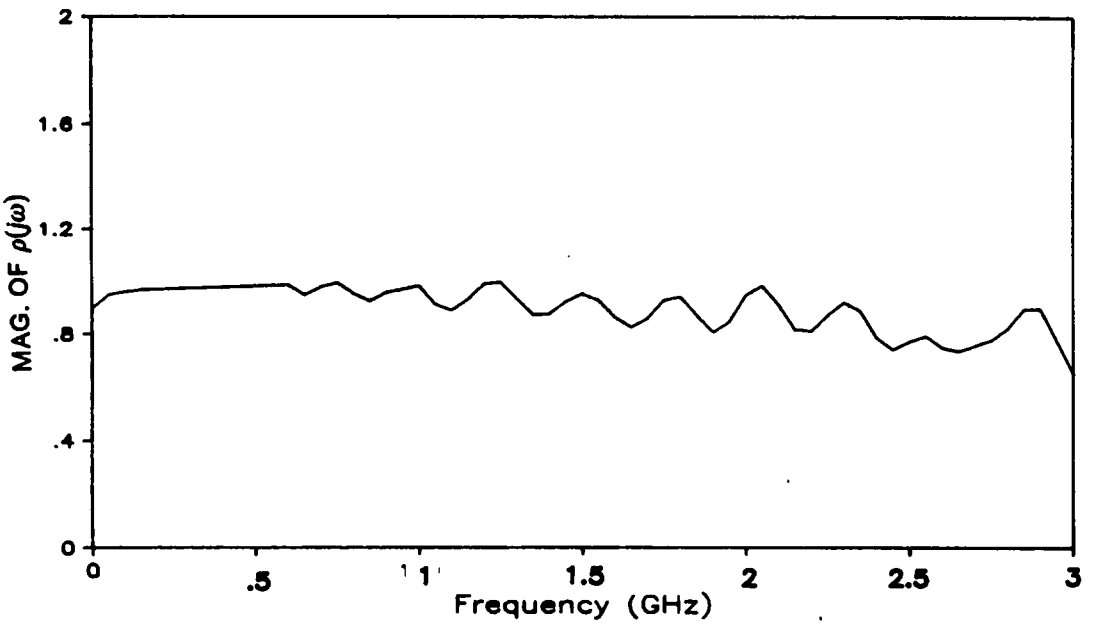

Figure (3.8). Magnitude of $\rho(j\omega)$ from the response waveform shown in Figure (3.7).

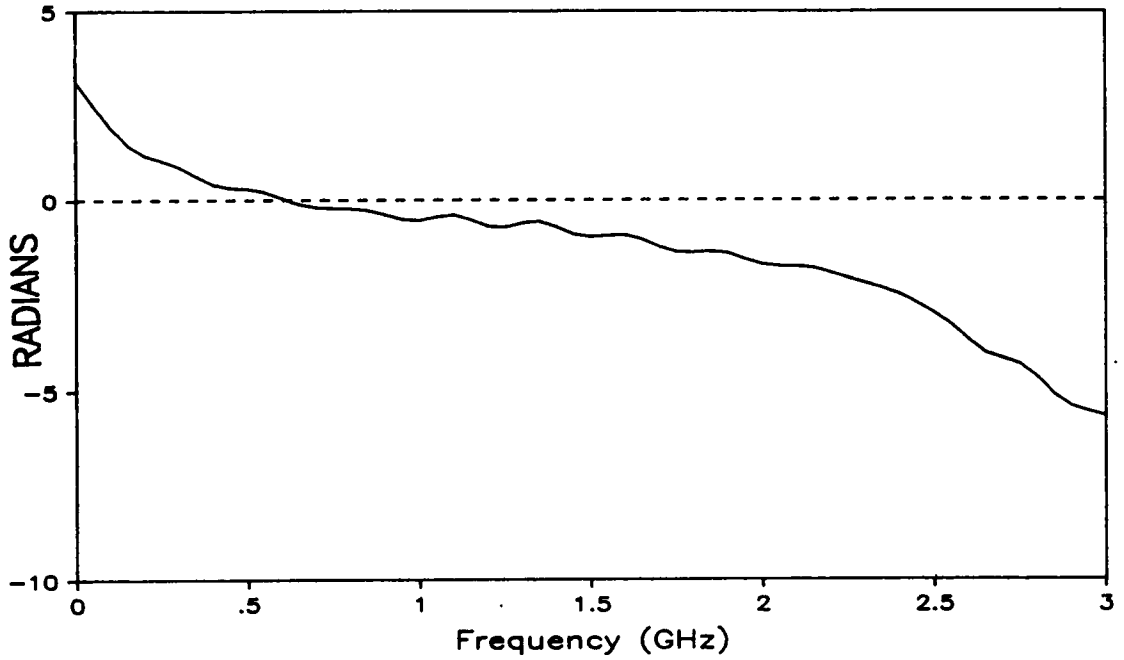

Figure (3.9). Phase of $\rho(j\omega)$ from the response waveform shown in Figure (3.7).

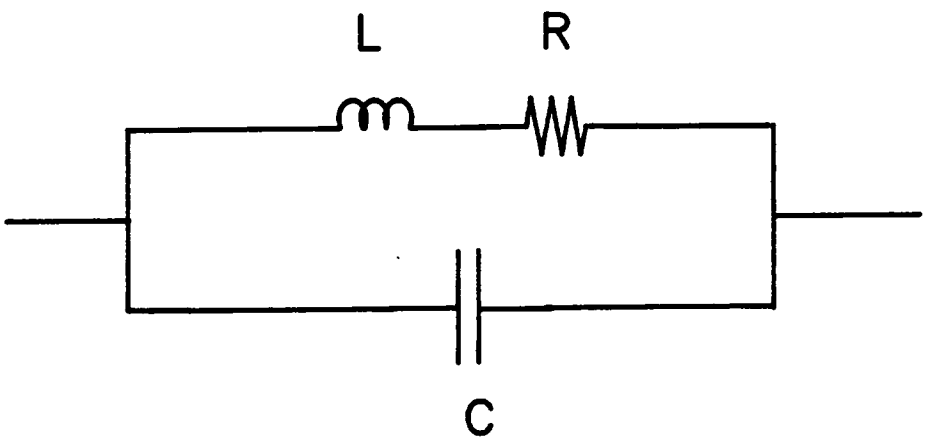

Figure (3.10). Single layer coil electrical model.

Table (3.1). Final values for different single layer coil thick film inductors [28]

Inductor Configuration	*L* (*nH*)	*C* (*pF*)	R_{dc} (Ω)
DuPont-6134 01	52.79	1.16	2.74
Remex-2034 01	50.0	1.04	4.42
Remex-2034 21	70.0	0.86	5.34
Remex-2034 012	65.0	0.92	5.73
Remex-2550 01	61.0	0.98	1.62
Remex-2550 21	67.9	1.04	2.73
Remex-2550 012	62.5	1.13	2.68
ESL D9912-F 01	51.0	1.25	1.22
ESL D9912-F 21	56.2	1.12	1.69
ESL D9912-F 012	56.1	1.11	1.66

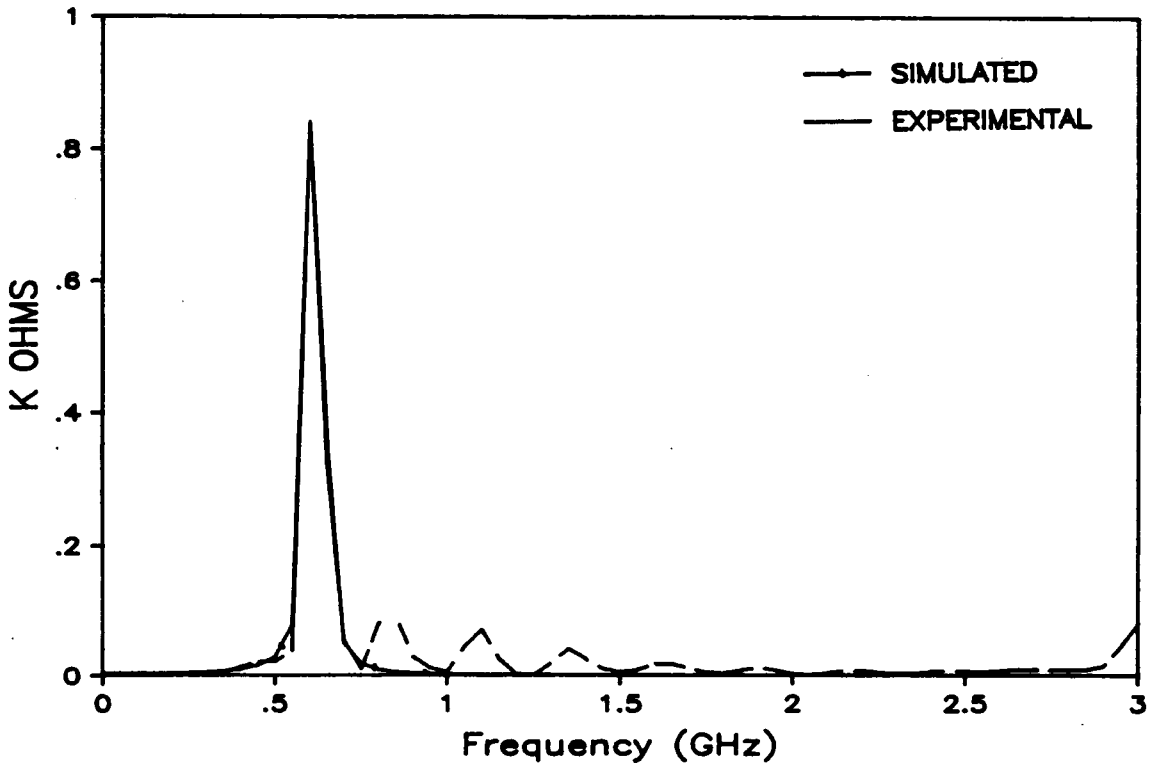

Figure (3.11). Comparison between the impedance real components of the single layer coil and it's model.

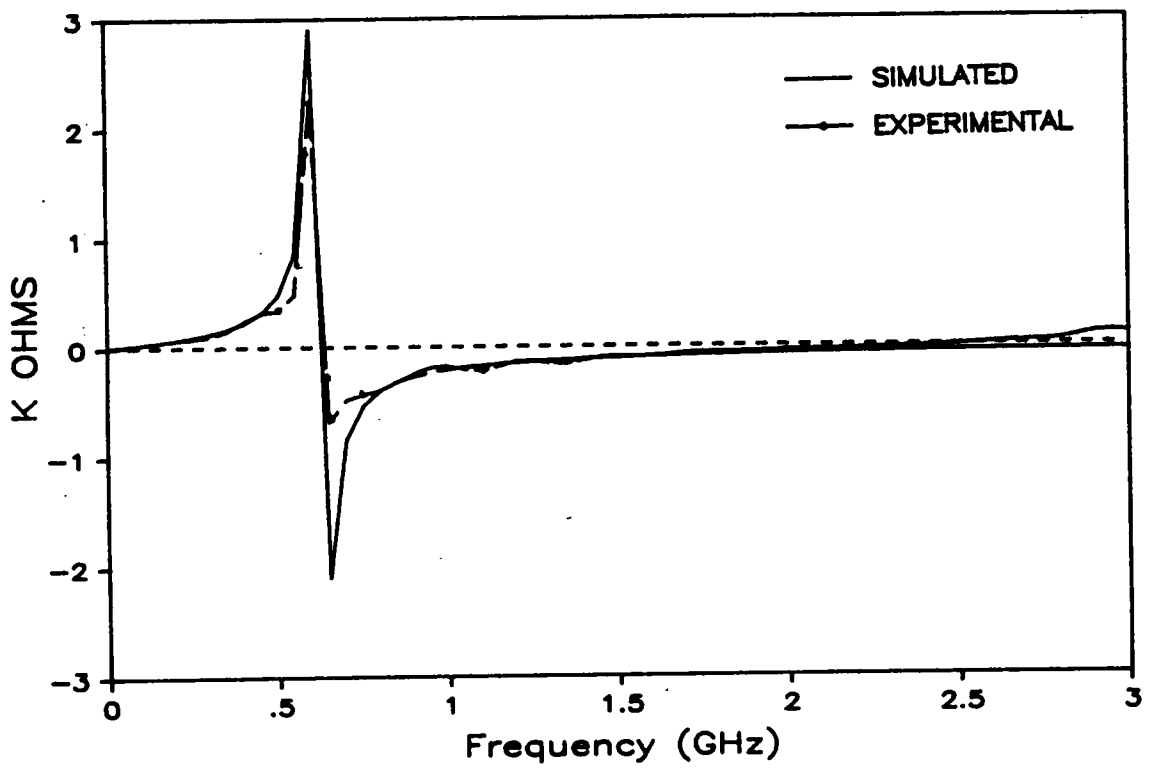

Figure (3.12). Comparison between the impedance imaginary components of the single layer coil and it's model.

3.5.3 RESULTS OF MULTILAYER COILS MODELING

Figure (3.4) illustrates the TDR reference and response waveforms of a dielectric filled multilayer coil. The structure consists of lower spiral coil, followed by two dielectric layers, and finally an upper spiral coil. The final model illustrated in Figure (3.13) has the initial and final component values tabulated in Table (3.2). One can observe that the model becomes more complex compared to the single layer coil model illustrated in Figure (3.10). The final values, as tabulated in Table (3.2), produce the required match. These results are illustrated in Figure (3.14), for the experimental and simulated response waveforms.

Figure (3.5) illustrates the TDR reference and response waveforms of a ferrite filled multilayer coil. One can observe that the response waveform is more complex than the one for the dielectric filled multilayer coil. Starting from the pulse launch end, the first discontinuity that can be seen in the response waveform can be modeled by two components, a series inductance and a shunt capacitance with the transmission line. After some delay, modeled by a transmission line, the second discontinuity is encountered. This discontinuity can be owed to an inductor in series with the line. Another transmission line is added to the model to account for a very short delay. After the last delay, a discontinuity is encountered. This can be modeled by a shunt capacitor with the line. A third transmission line is added to model one more short delay. The final reflection is a very complicated one as one can devise from the model. That final reflection is modeled by three tank circuits and two transmission lines which can be seen in the final model illustrated in Figure (3.15). The initial and final values of the components of that model are tabulated in Table

(3.3). The final values, shown in Table (3.3), produce the match, illustrated in Figure (3.16), between the experimental and simulated response waveforms.

One can notice that some components are in the final model while they do not have initial values in Table (3.3). These additional components are needed sometimes to fit a small part of the simulated response waveform to it's corresponding part of the inductor response waveform. This demonstrates the difficulty of obtaining the final model in some cases.

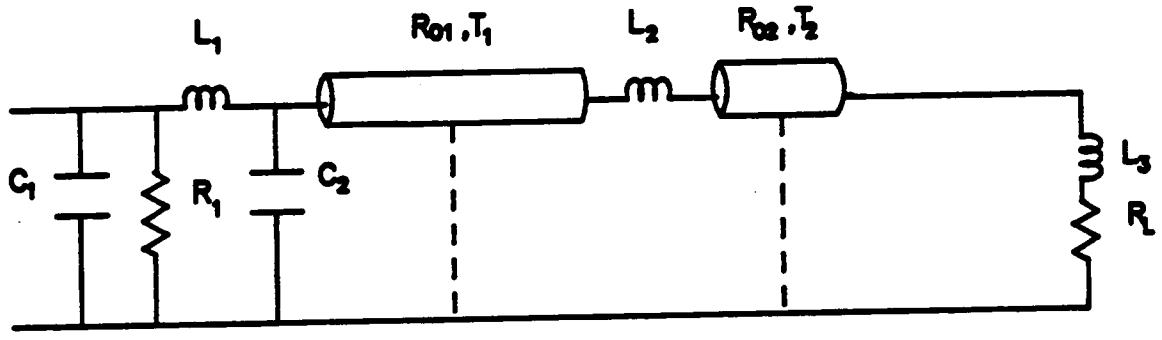

Figure (3.13). Electrical model for the multilayer inductor with dielectric material.

Table (3.2). Initial and final values of the model for the multilayer inductor with dielectric material.

Component	Initial Value	Final Value
C_1 (pF)	0.1	4.0
R_1 ($K\Omega$)	-	15
L_1 (nH)	7.2	5.25
R_{o1} (Ω)	50	45
T_1 (ps)	450	465
L_2 (nH)	9.7	9
R_{o2} (Ω)	50	35
T_2 (ps)	270	200
C_2 (pF)	6.6	6.8
R_2 ($K\Omega$)	-	15
L_3 (nH)	136	131
R_L (Ω)	2.17	1.75

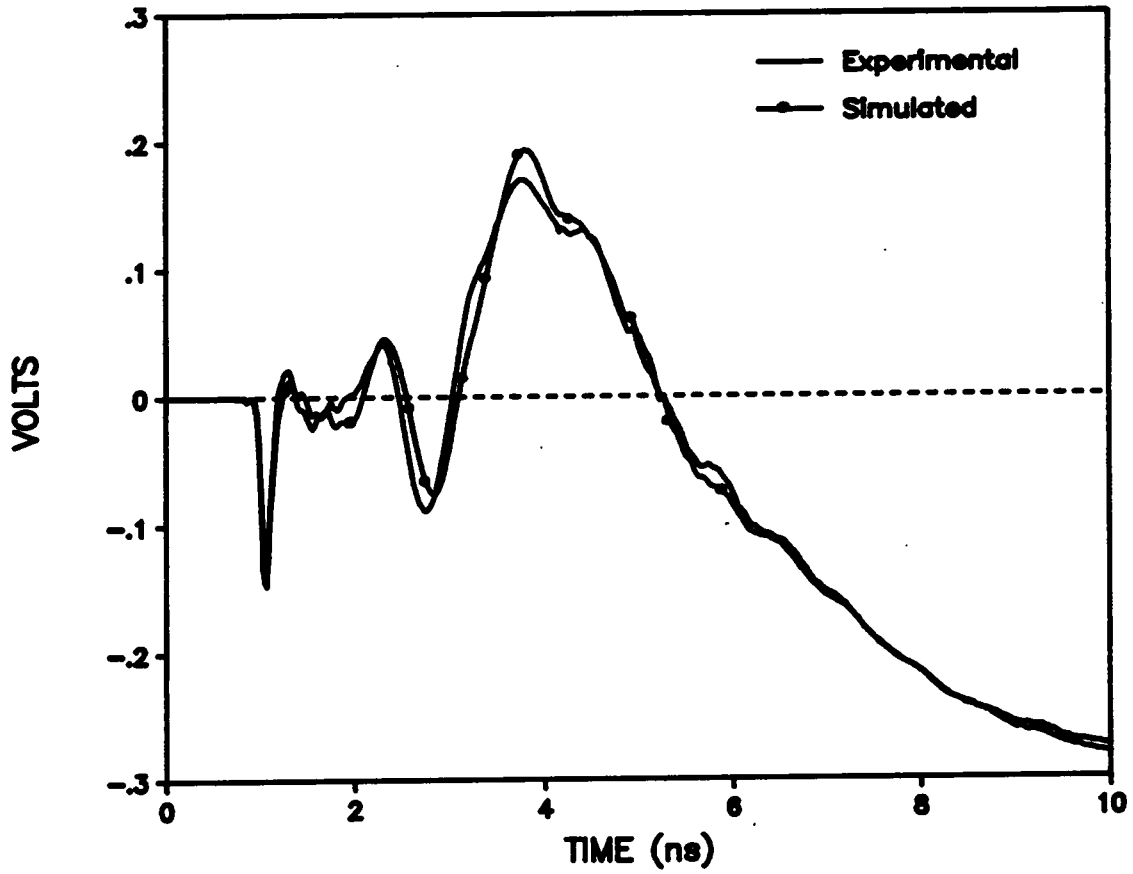

Figure (3.14). Experimental and simulated response waveforms for the multilayer inductor with dielectric material.

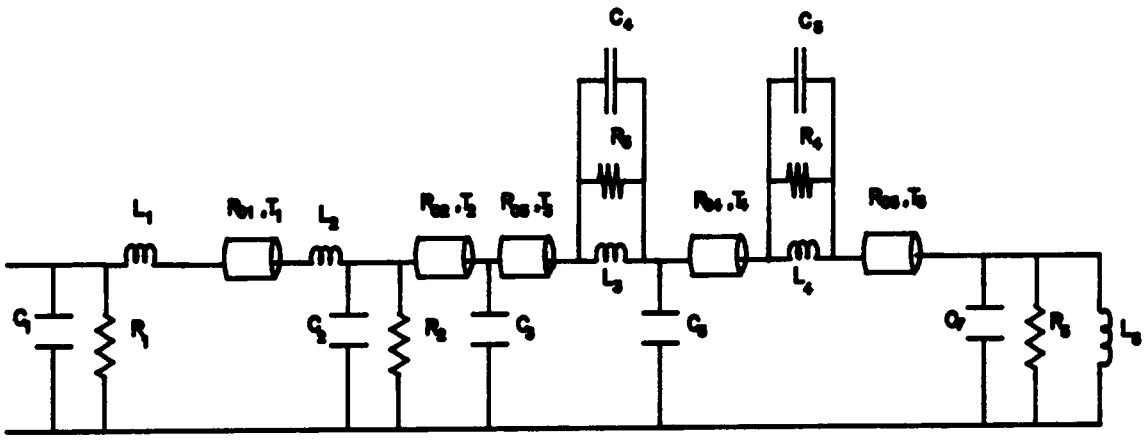

Figure (3.15). Electrical model for the multilayer inductor with ferrite material.

Table (3.3). Initial and final values of model for the multilayer inductor with ferrite material.

Component	Initial Value	Final Value
C_1 (pF)	0.1	2.0
R_1 ($K\Omega$)	-	2
L_1 (nH)	15	9
R_{o1} (Ω)	50	82
T_1 (ps)	450	450
L_2 (nH)	5	6.2
C_2 (pF)	-	1.5
R_2 ($K\Omega$)	-	2
R_{o2} (Ω)	50	150
T_2 (ps)	100	61
C_3 (pF)	2	1.1
R_{o3} (Ω)	100	70
T_3 (ps)	100	115
L_3 (nH)	60	55
C_4 (pF)	-	7
R_3 ($K\Omega$)	-	2
C_5 (pF)	-	1.2
R_{o4} (Ω)	150	200
T_4 (ps)	100	50
L_4 (nH)	60	55
C_6 (pF)	-	2.25
R_4 ($K\Omega$)	-	1
R_{o5} (Ω)	150	190
T_5 (ps)	10	20
L_5 (nH)	30	12
C_7 (pF)	-	1.5
R_5 ($K\Omega$)	-	2

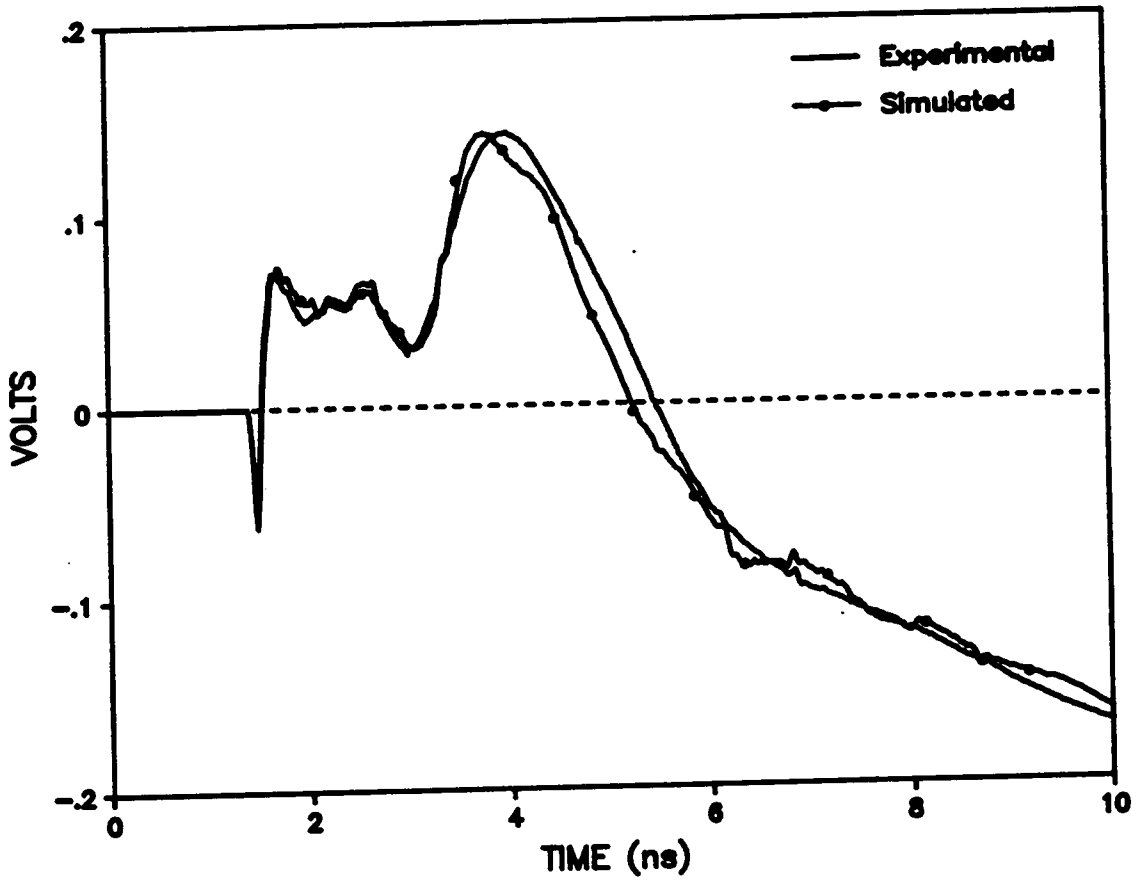

Figure (3.16). Experimental and simulated response waveforms for the multilayer inductor with ferrite material.

3.5.4 MODELING ACCURACY

A verification experiment to check the accuracy of the modeling process is the subject of this subsection. Two driving point impedances are used to perform this experiment. The first driving point impedance is the impedance of the inductor's final model, which is computed using PSPICE. This computation can be done using any network analysis package with frequency domain capability. The other driving point impedance is the inductor impedance measured experimentally using the HP 4193A Vector Impedance Meter (VIM). These measurements are conducted for the frequency range 1 - 110 MHz, with a frequency step of 1 MHz. The VIM is interfaced to an IBM personal computer for the data acquisition. The Radio Frequency measurements setup is illustrated in Figure (3.17). Both impedances mentioned above are plotted together and compared.

The verification experiment is achieved on the results obtained from the modeling of the multilayer inductor with dielectric material. The final model is used as a network in PSPICE, and an AC analysis is performed. The results of the AC analysis are used to calculate the driving point impedance of the model. Figures (3.18) and (3.19) illustrate the real and imaginary components of both driving point impedances, respectively. With little discrepancies, these figures show a good agreement between the calculated model impedance and the measured one. These discrepancies can be attributed to two reasons, the mismatch between the experimental and simulated response waveforms (see Figure (3.14)) and the inaccuracy of the impedance measurement. This experiment and it's results prove that the model obtained is an accurate representation of the inductor. This can be concluded from

the match obtained between the driving point impedances of the inductor and it's model as shown in Figures (3.18) and (3.19).

3.5.5 VALIDITY OF THE MODELING PROCESS

If the insertion impulse response of two networks are equal, then the $S_{21}(s)$ scattering parameters of the two networks are equal assuming that the driving source waveform is the ideal impulse. In practice, the driving source waveform is never an ideal impulse or step. This means that any applied signal can have a slow leading edge. Thus, in the instant near $t = 0^+$, which corresponds to $|s| \rightarrow \infty$, information can be lost or in other words some waveform variations may not appear. As a result of the above discussion, any model based upon an observed physical waveform, like the one shown in Figure (3.4), may not contain information extending endlessly to higher frequencies. A similar argument can be made for low frequencies if it can not be said that for all practical purposes, the waveform has reached it's final value at the end of the chosen time window ($t = 10\,ns$ in Figure (3.4)). Therefore, there can be more than one model that can perform satisfactorily over the frequency band of interest. In other words, the modeling techniques used in this work in the time or frequency domain may not yield a unique model nor provide information for all times or frequencies. The quality of the modeling depends also on the human factor, the person performing the modeling. Such experiment is designed to study the non-uniqueness of the model and its dependence on the human factor.

The experiment started with the acquisition of the response waveform of a particular network, due to a ramp excitation with a 0.39 *ns* transition duration. Figure (3.20) illustrates the original circuit with it's components values, while Figure (3.21)

shows the reference and response waveforms. Next, three individuals were provided with the reference and response waveforms information, and were requested to derive a model that has a response waveform which matches that of the original circuit. The three individuals reached the three models illustrated in Figure (3.22). As one can see, the three models are completely different except for the first two components. The three models produce the close match desired between the original response waveform and the simulated response waveforms illustrated in Figure (3.23). Table (3.4) illustrates the component values of the three models. This experiment and it's results prove that the model is non-unique and different individuals may obtain different valid models for the same original circuit.

To test if the models are dependent on the type of excitation, the original model as well as the the different models were excited with ramps with different transition duration (step, 0.195 *ns*, 0.78 *ns*). A step excitation is used to check the models at a wider band of frequencies. The three models produce response waveforms with close match to the ones from the original model under these different excitations (see Figures (3.24), (3.25), and (3.26)). This experiment and it's results prove the insensitivity of the model derived to the type of the excitation.

To check the accuracy of the three models, the experiment explained in subsection 3.5.5 is applied on the three models. Figures (3.27), (3.28), (3.29), and (3.30) show the comparison between the real part, imaginary part, magnitude, and phase of the impedance, respectively, of the original network with those of models. As one can observe from these figures, at low frequencies there is a close match between the models and the original circuit. At high frequencies (above 9 GHz) the models have some resonances that do not exist in the original network. This is attributed to

the mismatch that exists between the original response waveform and the response waveforms of the three models.

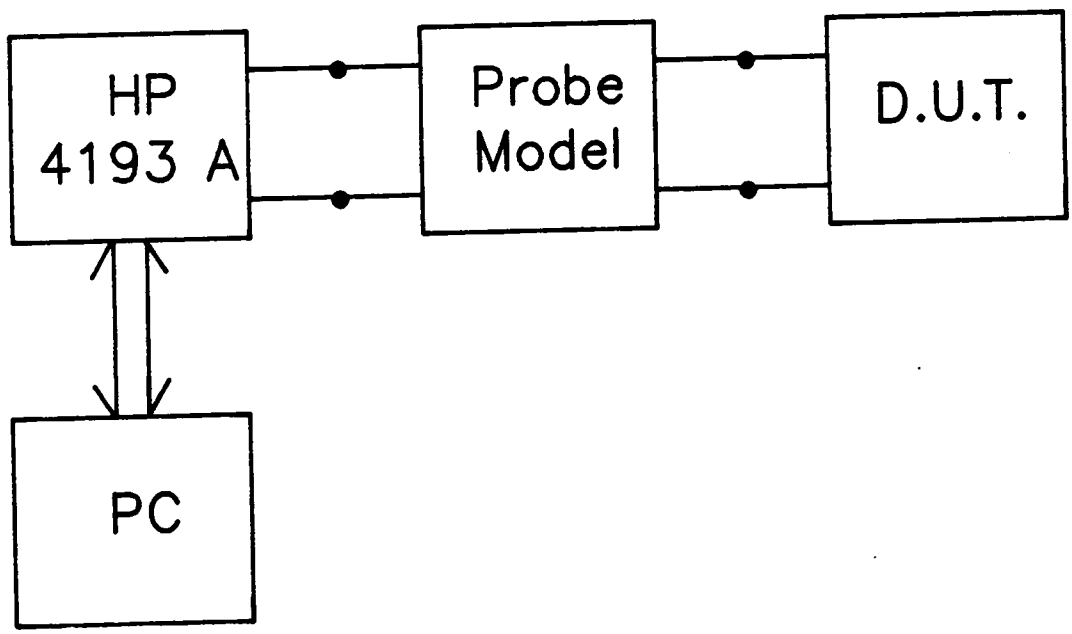

Figure (3.17). RF measurement setup.

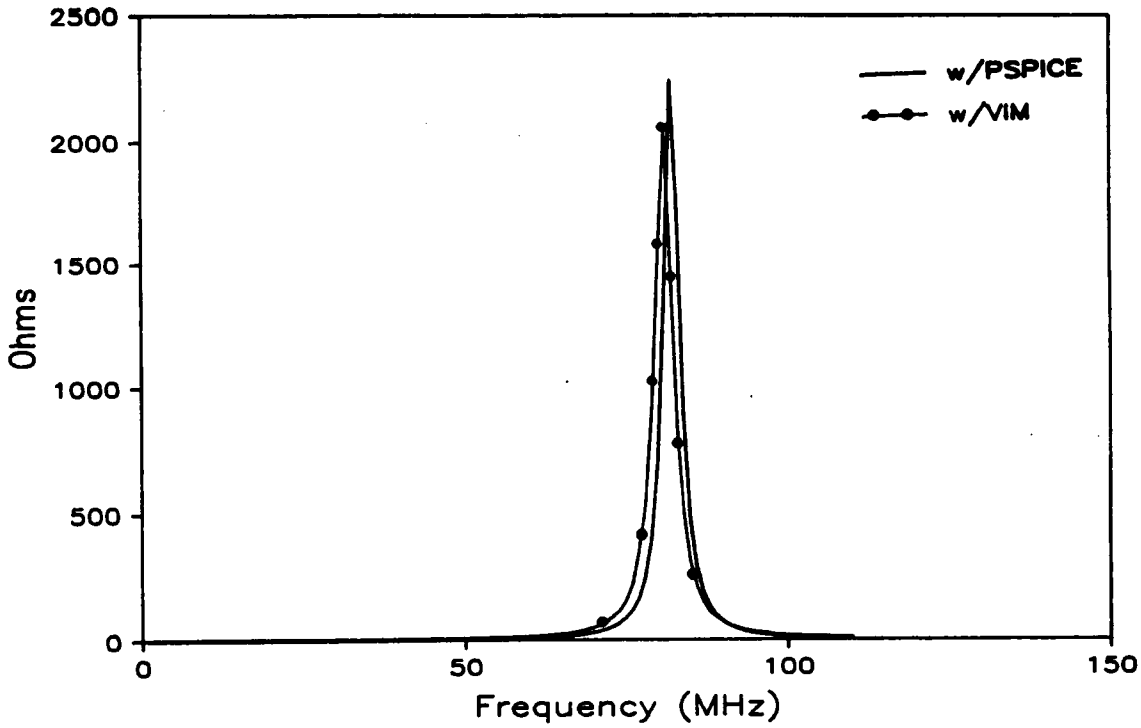

Figure (3.18). Comparison between the real component of impedance calculated from PSPICE and the one measured on the VIM.

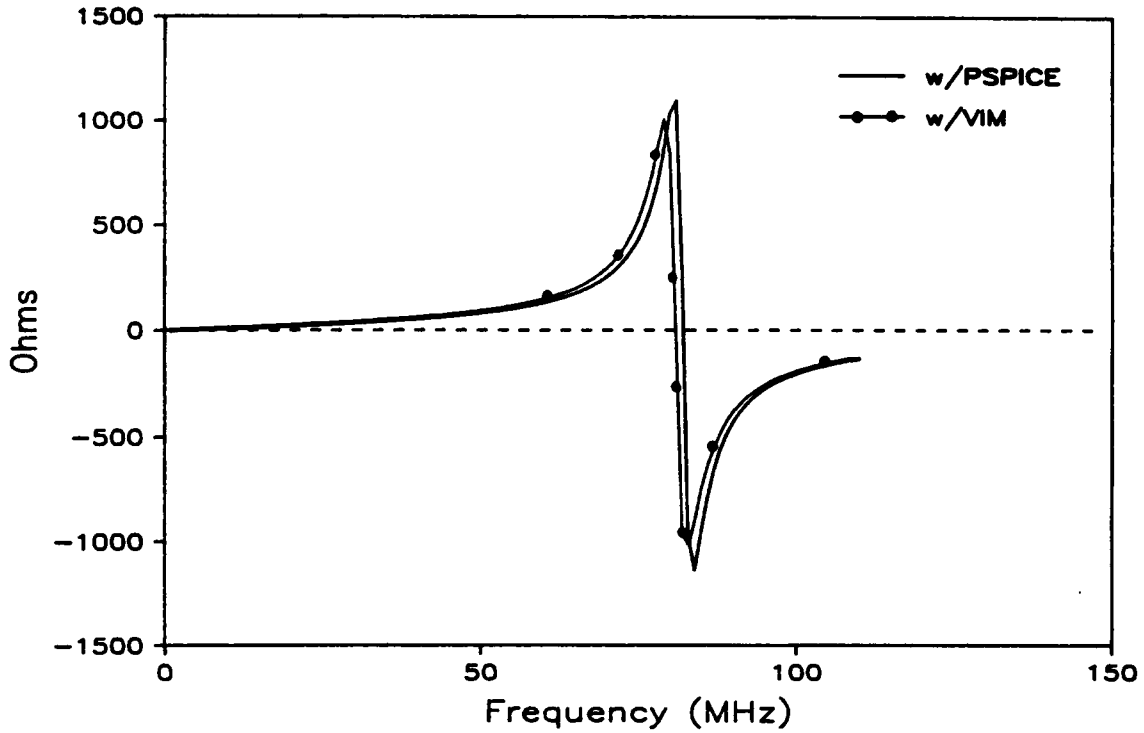

Figure (3.19). Comparison between the imaginary component of impedance calculated from PSPICE and the one measured on the VIM.

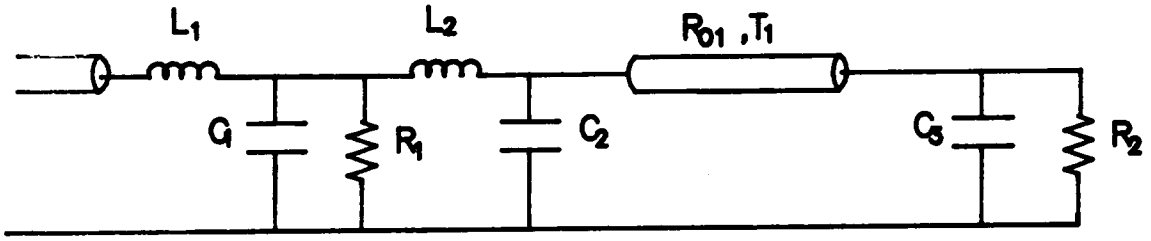

$L_1 = 8.10$ nH
$C_1 = 17.4$ pF
$R_1 = 333.0\ \Omega$
$L_2 = 15.2$ nH
$C_2 = 7.70$ pF
$R_{01} = 25.0\ \Omega$
$T_1 = 0.29$ ns
$R_2 = 75.0\ \Omega$
$C_3 = 24.9$ pF

Figure (3.20). Original circuit model.

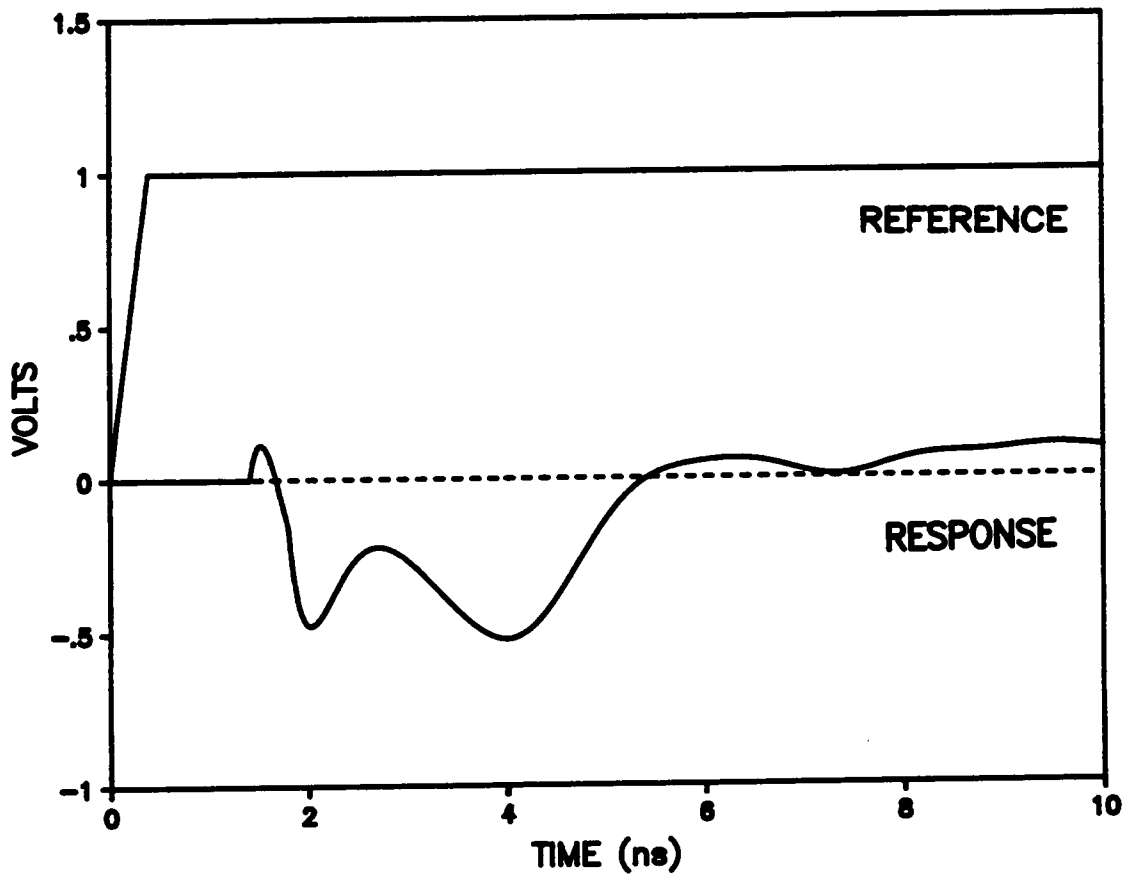

Figure (3.21). Reference and response waveforms of Original circuit.

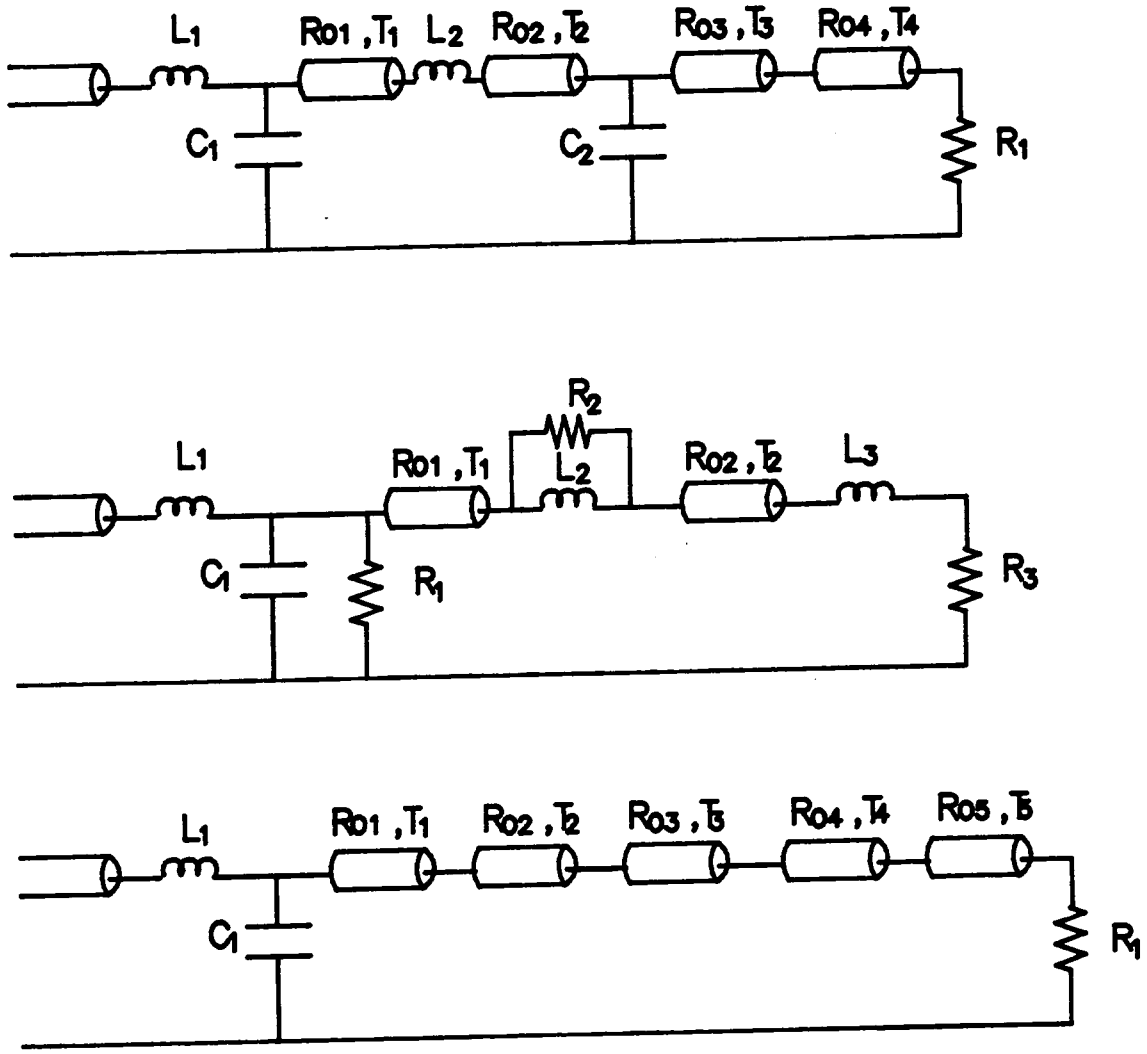

Figure (3.22). Three models of the original circuit.

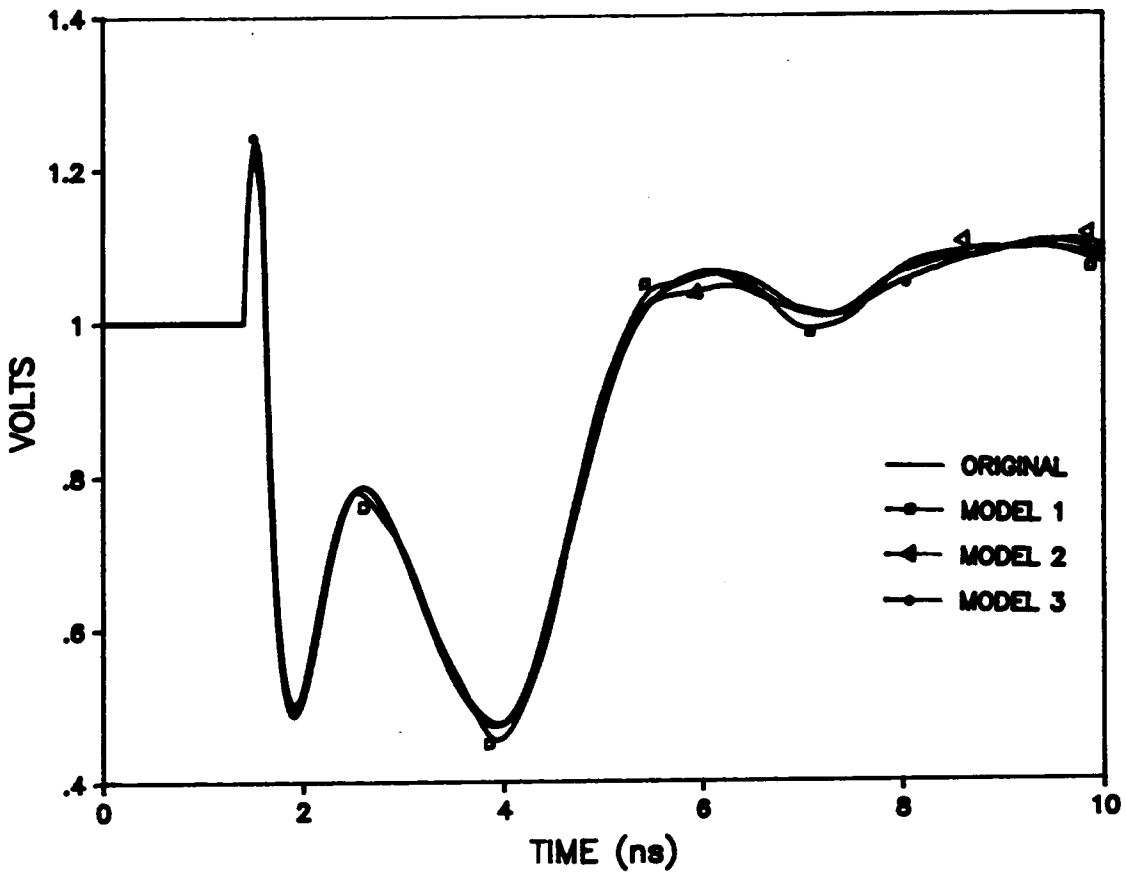

Figure (3.23). Comparison between the original response waveform and the models response waveform. 0.39 *ns* ramp excitation.

Table (3.4). Component values for the three models.

Model 1	Model 2	Model 3
$L_1 = 7.75\ nH$	$L_1 = 7.70\ nH$	$L_1 = 8.5\ nH$
$C_1 = 12.0\ pF$	$C_1 = 12.5\ pF$	$C_1 = 15.0\ pF$
$R_{o1} = 50.0\ \Omega$	$R_1 = 1.5\ K\Omega$	$R_{o1} = 42.0\ \Omega$
$T_1 = 0.21\ ns$	$R_{o1} = 30.0\ \Omega$	$T_1 = 0.36\ ns$
$L_2 = 7.4\ nH$	$T_1 = 0.23\ ns$	$R_{o2} = 17.0\ \Omega$
$R_{o2} = 19.0\ \Omega$	$L_2 = 8.3\ nH$	$T_2 = 0.8\ ns$
$T_2 = 0.6\ ns$	$R_2 = 100.0\ \Omega$	$R_{o3} = 54.0\ \Omega$
$C_2 = 13.3\ pF$	$R_{o2} = 16.5\ \Omega$	$T_3 = 0.5\ ns$
$R_{o3} = 28.0\ \Omega$	$T_2 = 0.9\ ns$	$R_{o4} = 70.0\ \Omega$
$T_3 = 0.2\ ns$	$L_3 = 17.5\ nH$	$T_4 = 0.5\ ns$
$R_{o4} = 64.0\ \Omega$	$R_3 = 65.0\ \Omega$	$R_{o5} = 64.0\ \Omega$
$T_4 = 1.605\ ns$		$T_5 = 0.5\ ns$
$R_1 = 60.0\ \Omega$		$R_1 = 60.0\ \Omega$

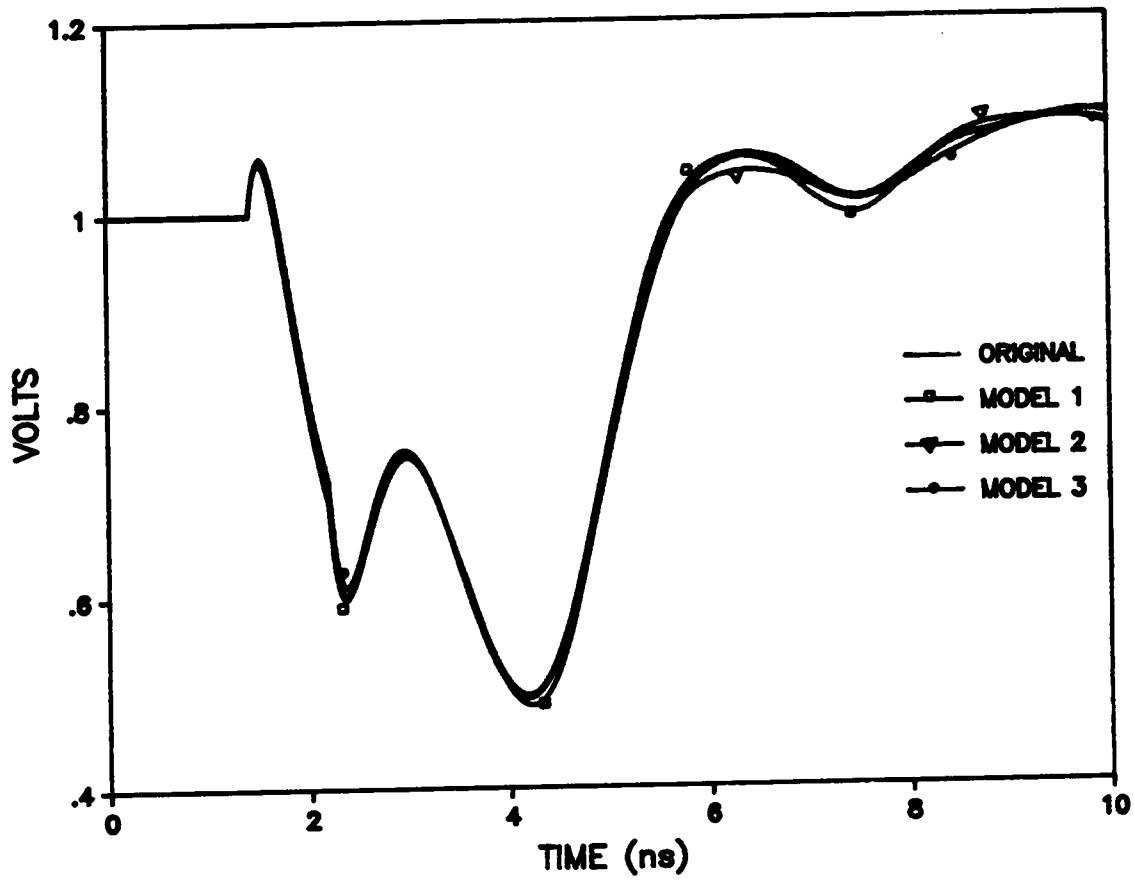

Figure (3.24). comparison between response waveforms. Step excitation.

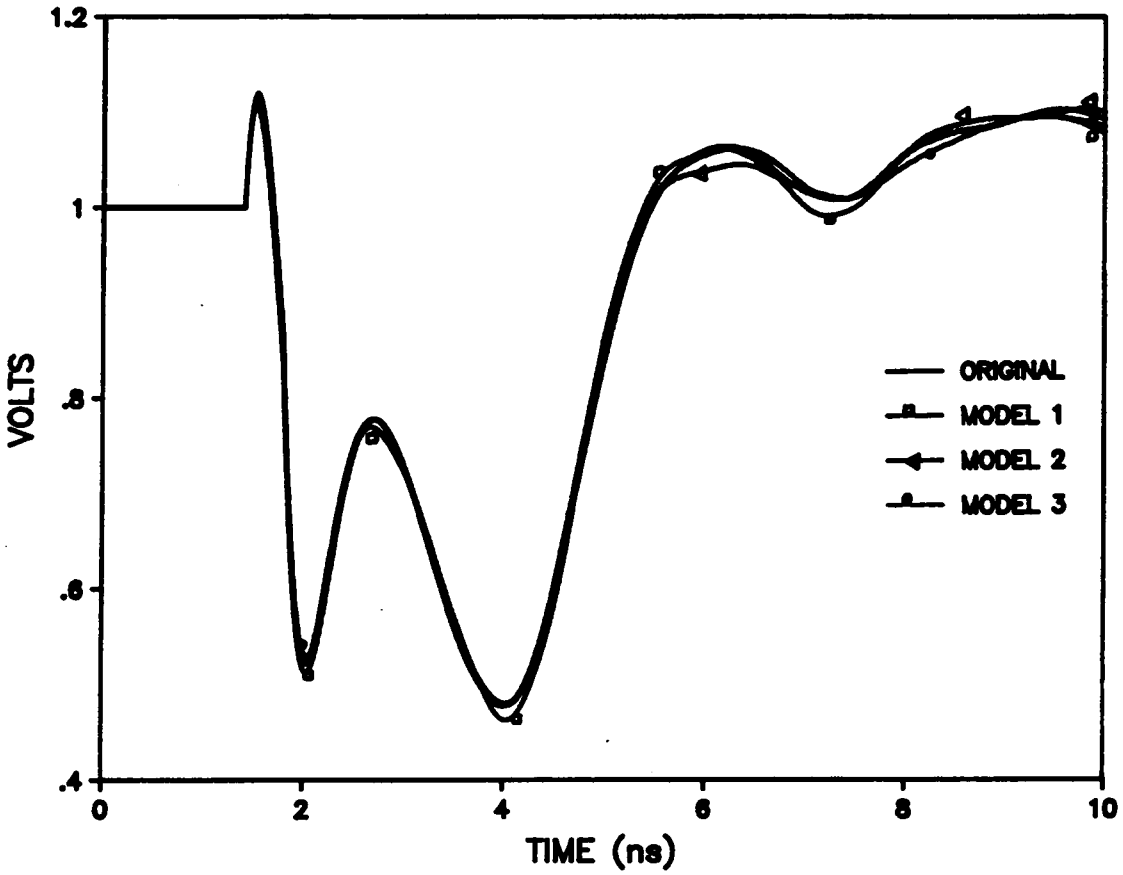

Figure (3.25). Comparison between response waveforms. 0.195 *ns* excitation.

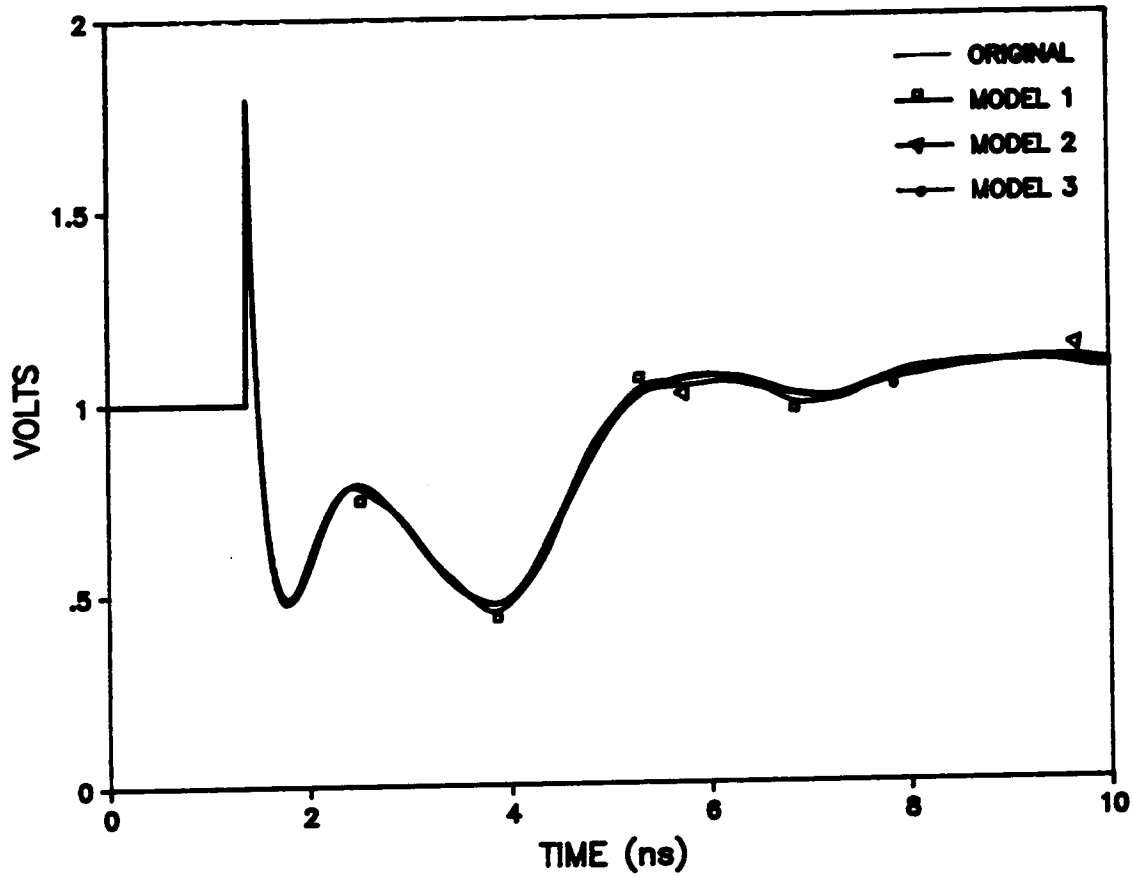

Figure (3.26). Comparison between response waveforms. 0.78 *ns* excitation.

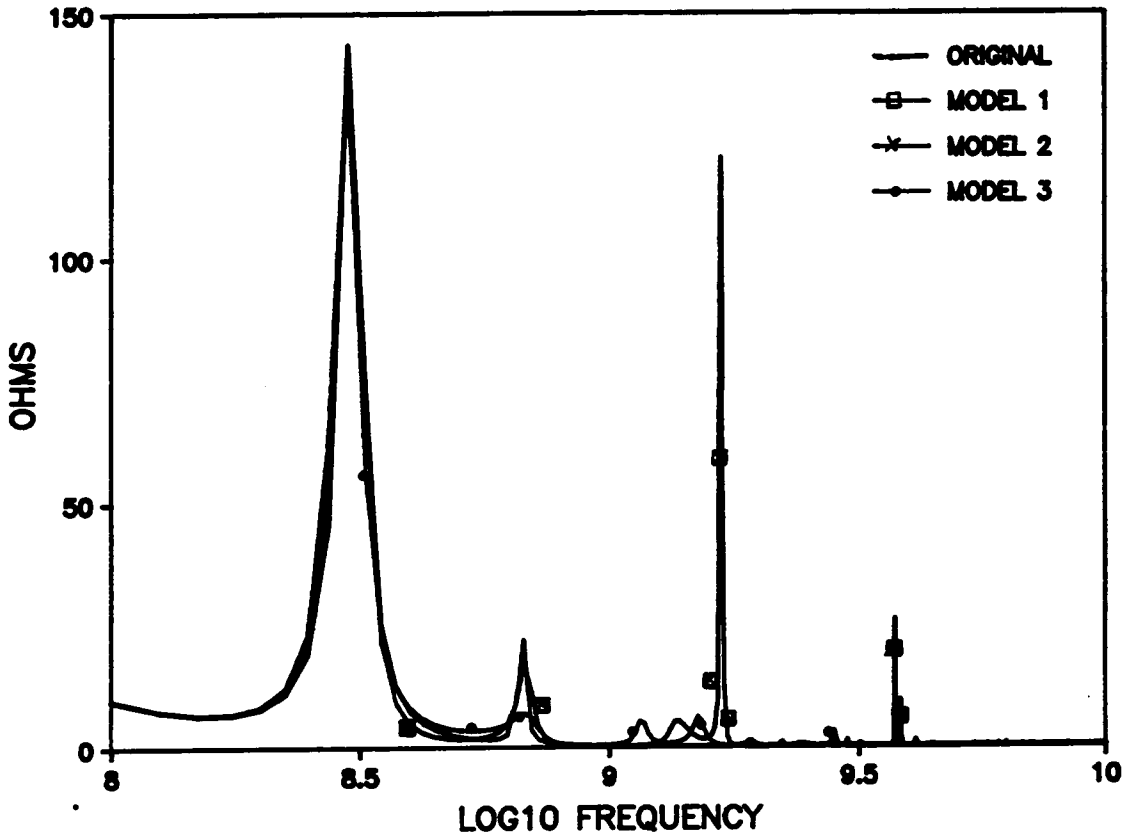

Figure (3.27). Comparison between the impedance real component of the original circuit with the impedance real components of the models.

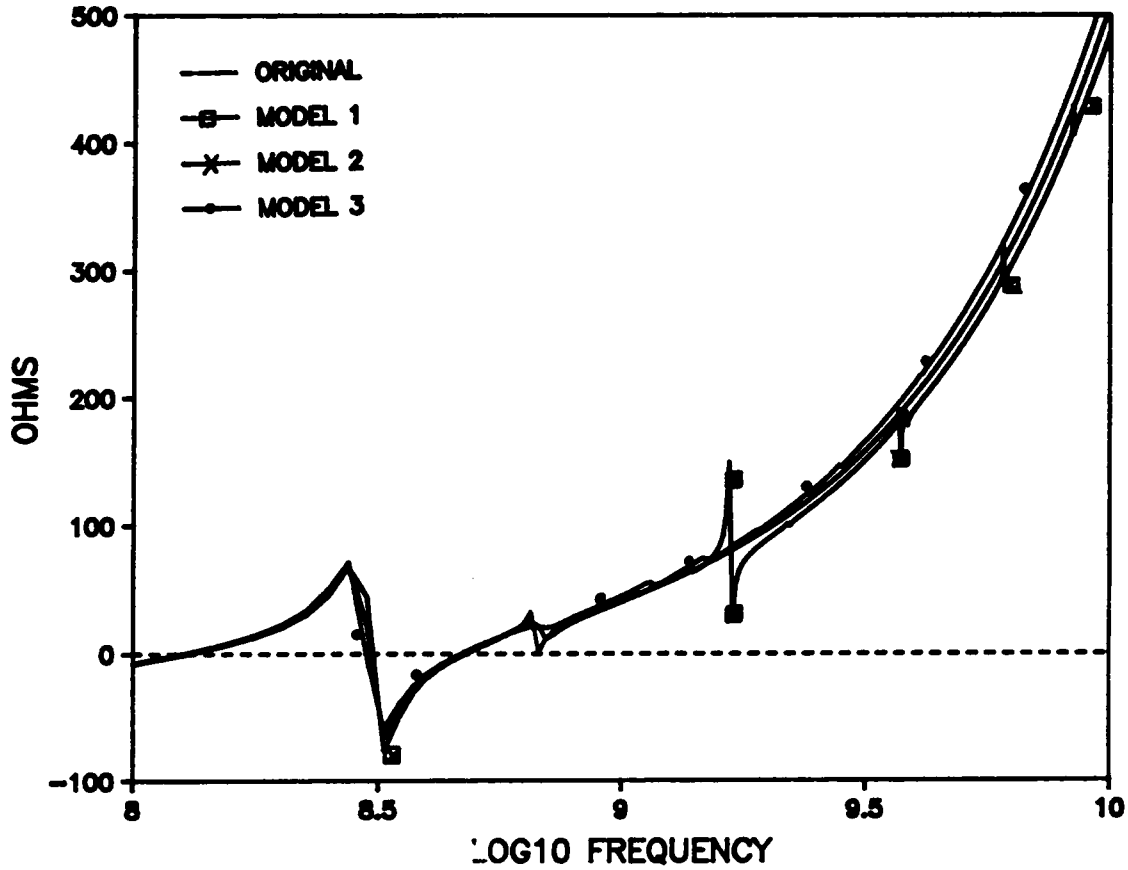

Figure (3.28). Comparison between the impedance imaginary component of the original circuit with the impedance imaginary components of the models.

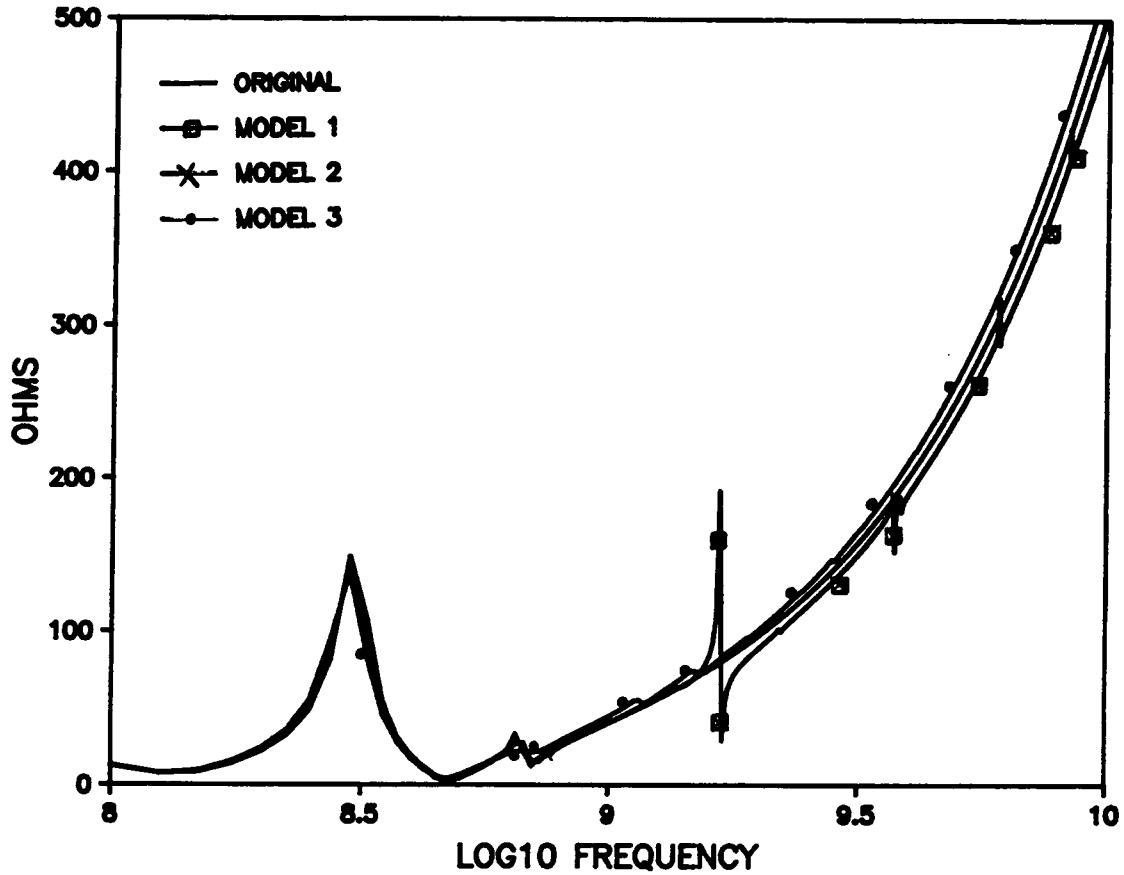

Figure (3.29). Comparison between the magnitude of the impedance of the original circuit with the magnitude of the impedances of the models.

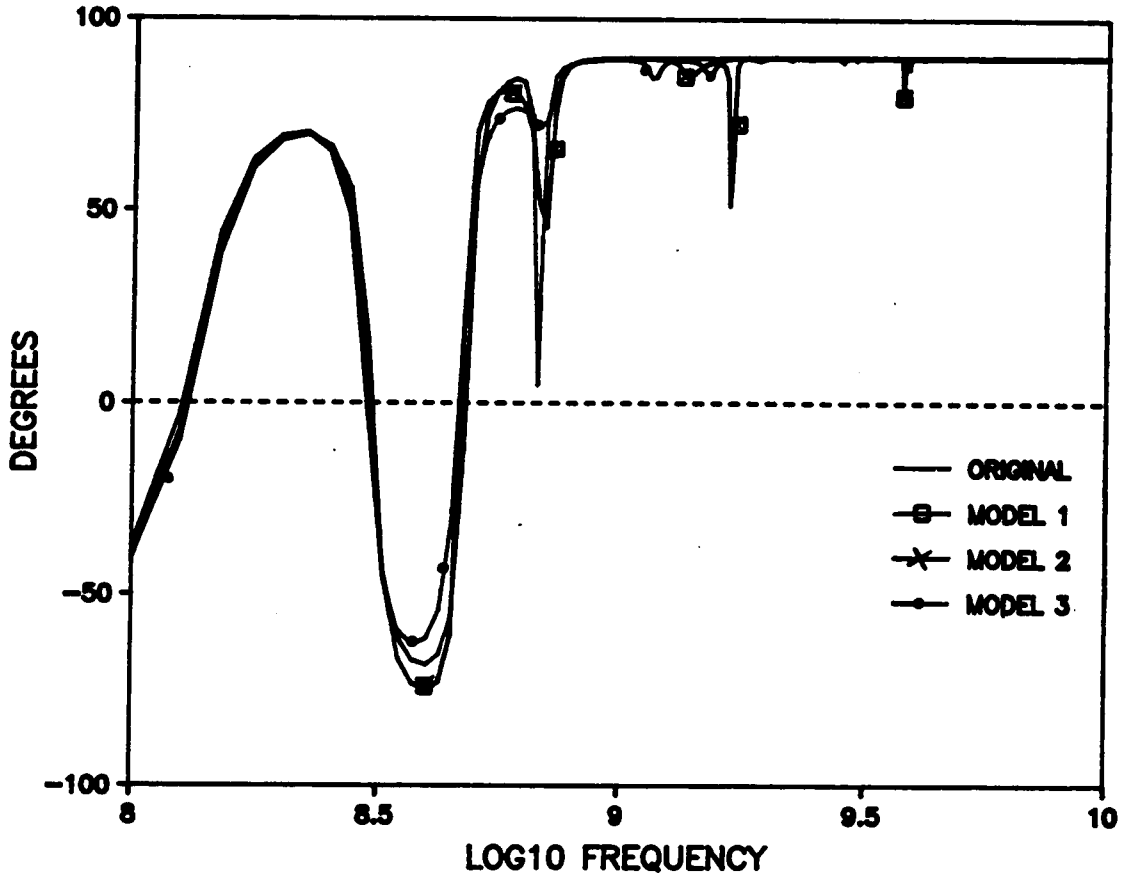

Figure (3.30). Comparison between the phase of the impedance of the original circuit with the phase of the impedances of the models.

3.6 CONCLUSION

Modeling and characterization of three structures of thick film inductors at high frequencies were discussed in this chapter. These three structures were, the single layer coil, the multilayer coil separated with dielectric material, and multilayer coil separated by ferrite material. Modeling procedures and final results of the three structures were presented. It was obvious from these results that the models were getting more complex as the inductor structure became more complex.

TDR technique was used in the data acquisition and modeling of the inductor under test over the frequency range from DC to few GHz. The thick film inductor under test was printed and located at the end of a reference transmission line. For the single layer coil, the model was constructed in the Frequency Domain. The model impedance was compared to an experimentally measured of the inductor under test. For the other two structures, TDR was used to construct a model for the inductor under test. An iterative approach of modeling was presented. Comparison between the measured response waveform and simulated response waveform was performed. Good match between the two previously mentioned waveforms was achieved.

Accuracy of the modeling process was checked by comparing the driving point impedance of the final inductor model and the actual one measured using a Vector Impedance Meter. The conclusion was that the model was accurate enough to create a good match between the two impedances. Validity of the modeling process was also discussed. It was concluded that different valid models for a particular circuit can be reached. It was also concluded that the model is valid for any type of excitation.

CHAPTER IV

WIDEBAND CHARACTERIZATION OF FERRITE MATERIALS USING FERRITE FILLED CAVITY

4.1 INTRODUCTION

As demonstrated in chapter III, the use of ferrite materials in the construction of thick film inductors enhances the inductance value. It was also mentioned that there is a lack of accurate knowledge of the specifications and characteristics of available thick film ferrite pastes. This is due to the lack of studies of ferrite materials in thick film structures. This chapter will deal with the wideband characterization of thick film ferrite pastes. Characterization results of two different ferrite pastes will be presented.

The proposed configuration for the wideband characterization of ferrite pastes is illustrated in Figure (4.1). In the proposed configuration, a cavity like sample holder is attached to the end of a transmission line. In the conventional configuration, the material sample is shaped to a required precision and is inserted inside a transmission line in its different types. This technique creates a problem because the

sample has to be cut very precisely to fit exactly in between the inner and outer conductors of a coaxial air line. As a result, air gaps are created between the sample and the line's conductors. These air gaps lead to erroneous results of μ_r^*, the relative complex permeability.

In the new proposed configuration, there is no need to cut or shape the sample precisely to fit in an existing structure, rather, the cavity walls can be modeled or deposited on a coaxially shaped sample [29]. As explained further in section 4.4, the top metallization is printed on top of the ferrite sample, thus eliminating any chance of air gaps creation. In addition, the new structure is well suited for the thick film technology where the ferrite layer(s) as well as the cavity walls can be printed directly on a ceramic substrate. Lossless transmission line conductors and conductor walls are assumed. Linear material is assumed as well.

This chapter consists of seven sections, with Section 4.1 being an introductory section. In section 4.2, the full field analysis of the proposed structure is carried out. Section 4.3 discusses the results of the analysis carried through computer simulation performed on the cavity to test the proposed technique. Section 4.4 deals with the thick film equipment and materials used in order to achieve the proposed structure. The construction of the structure is also discussed in this section. TDR and FD measurement techniques conducted in the course of study are presented in section 4.5. Section 4.6 presents the experimental results of the characterization of two commercially available ferrite materials. Finally, a concluding section, section 4.7, summarizes the main findings of the chapter.

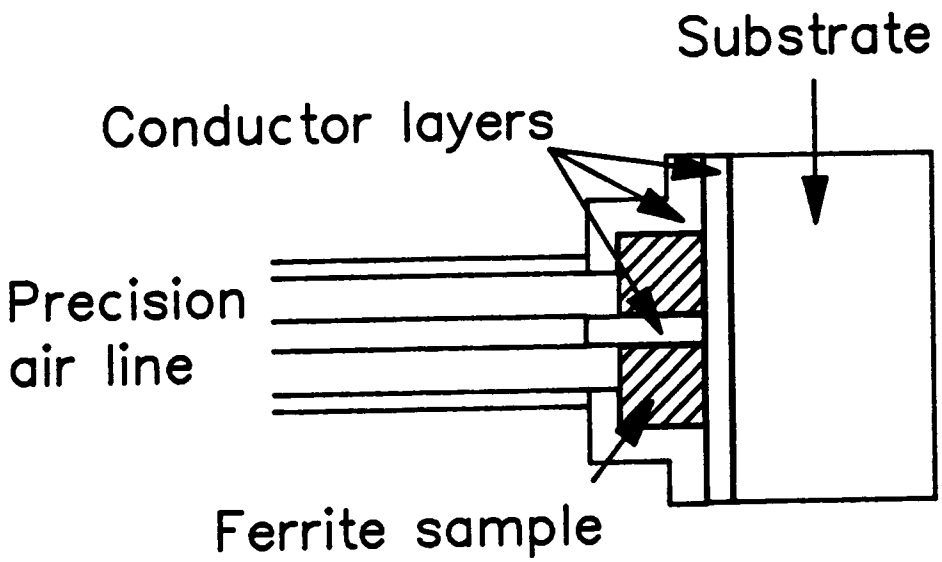

Figure (4.1). The coaxial cavity structure.

4.2 FIELD ANALYSIS OF THE PROPOSED CONFIGURATION

4.2.1 INTRODUCTION

The full field analysis of the proposed configuration is carried out using the method of moments [30]. Throughout the course of the analysis, it is assumed that the material is linear. The relative permittivity of the material, ε_r^*, is taken into consideration during the analysis. Lossless transmission line conductors and conductor walls are also assumed. The analysis is used to establish the functional relationship between the reflection coefficient, $\rho(j\omega)$, and the permeability, $\mu_r^*(j\omega)$, of the ferrite material. First, expression for the reflection coefficient is derived assuming that the ferrite properties are known. This work is carried out in subsection 4.2.2. Then the inverse process, which involves the computation of the complex permeability of the ferrite material given the reflection coefficient, is achieved numerically using an optimization method. The inverse process is the subject of subsection 4.2.3.

4.2.2 DERIVATION OF $S_{11}(j\omega)$ GIVEN μ_r^*

Figure (4.2) illustrates the model for the configuration shown in Figure (4.1). This model was obtained using the equivalence principle [31]. The model consists of two regions, region (a), the transmission line region, and region (b), the cavity region. A perfect electric conductor is assumed to replace the aperture on both regions. On top of the conductor, an equivalent magnetic current source M is imposed. The equivalent magnetic source in region (a) is denoted by M, while it is denoted by $-M$ in region (b), in order to ensure the continuity of the electric field. The current M

is solved for by satisfying the continuity of the magnetic field across the aperture. So the task now is to derive expressions for the magnetic fields in both regions (a) and (b).

Let us define the magnetic fields in regions (a) and (b) as H^a and H^b, respectively. H^a can be written as,

$$H^a = H^i + H^r + H^a(M) \tag{4.1}$$

where H^i and H^r are the incident and reflected magnetic fields, respectively. $H^a(M)$ is the magnetic field due to the source M, it can be computed with a conductor covering the aperture. H^b may be written as $H^b(-M)$ since it is only due to the source M. The minus sign can be taken outside the bracket, to become $-H^b(M)$, because of the linearity of the magnetic field.

From equating the tangential component of the magnetic field over the aperture in both regions, one can write,

$$H_t^a \equiv H^a|_{z=0} = H_t^b \equiv H^b|_{z=0} \tag{4.2}$$

where t stands for tangential. Then from equations (4.1) and (4.2), one can write,

$$H_t^a(M) + H_t^b(M) = -H_t^i - H_t^r = -2H_t^i \tag{4.3}$$

because $H_t^i = H_t^r$. M can be determined from equation (4.3) after obtaining the expressions for the field components in terms of M. This is achieved by solving Helmoltz scalar equation and applying the necessary boundary conditions [31]. Helmoltz equation is, of the form,

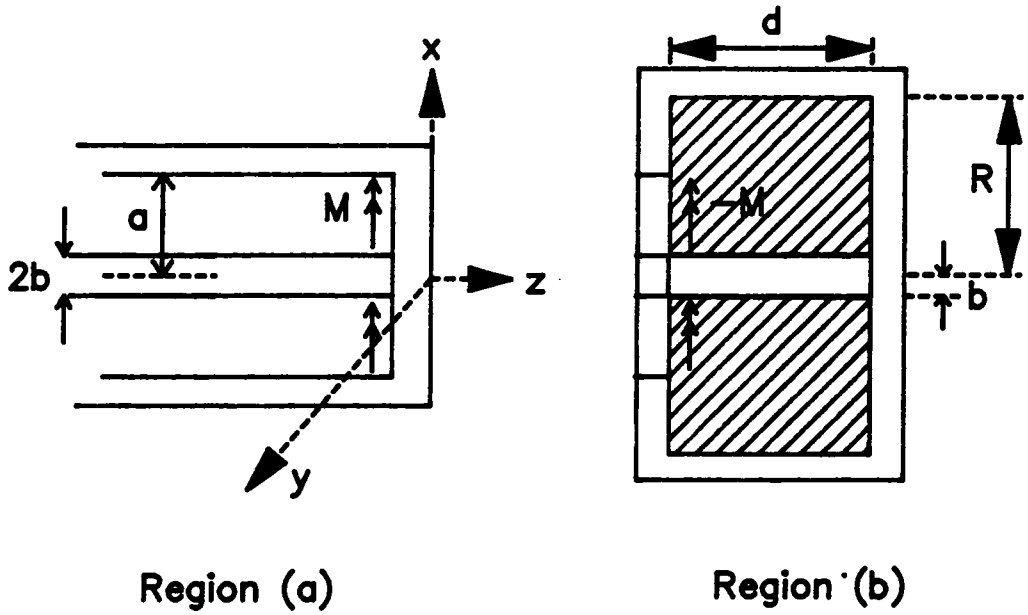

Figure (4.2). Model for the cavity structure after applying the equivalence principle.

$$\nabla^2\Psi + K^2\Psi = 0 \tag{4.4}$$

where $K = \omega\sqrt{\mu\varepsilon}$.

The structure being analyzed is axially symmetric, therefore the only higher order modes generated are the TM_{on} modes (no angular variation) [29]. The modes are given by,

$$E_\rho = \frac{1}{j\omega\varepsilon}\frac{\partial^2\Psi}{\partial z\partial\rho} \tag{4.5}$$

$$E_z = \frac{1}{j\omega\varepsilon}(K^2 + \frac{\partial^2}{\partial z^2})\Psi \tag{4.6}$$

$$H_\phi = -\frac{\partial\Psi}{\partial\rho} \tag{4.7}$$

$$E_\phi = H_\rho = H_z = 0 \tag{4.8}$$

The derivation of the magnetic field components is divided into three parts. The first two parts are one for each region (a) and (b). The third part explains the use of method of moments to achieve the final solution.

(1) Transmission Line Region, (a)

In this region, the TEM mode is the dominant mode [31]. Assuming unity incident power, then the incident field is given by,

$$H^{I} = \frac{1}{\eta_0\sqrt{2\pi \ln(a/b)}} \frac{1}{\rho} e^{-jK_0 z} u_\phi \tag{4.9}$$

where $\eta_0 = \sqrt{\frac{\mu_0}{\varepsilon_0}}$ is the intrinsic impedance. A suitable scalar function, Ψ^a, for finding $H_t^a(M)$ interms of M is the form [31],

$$\Psi^a = (B_0 + C_0 \ln \rho)e^{jK_0 z} + \sum_{n=1}^{\infty}\left[B_n J_0(K_{\rho_n}^a \rho) + C_n N_0(K_{\rho_n}^a \rho)\right]e^{jK_{z_n}^a z} \tag{4.10}$$

where J_0 and N_0 denote zeroth order Bessel functions of the first and second kind, respectively. K_0, $K_{\rho_n}^a$, and $K_{z_n}^a$ are related to each other by the separation equation,

$$(K_{z_n}^a)^2 + (K_{\rho_n}^a)^2 = K_0^2 = \omega^2 \varepsilon_0 \mu_0 \tag{4.11}$$

The constants B_n and C_n can be evaluated by applying the first boundary condition. The tangential component of the electric field should vanish at $\rho = a$ and $\rho = b$. Therefore, for $n > 0$, one can obtain,

$$B_n J_0(K_{\rho_n}^a a) + C_n N_0(K_{\rho_n}^a a) = B_n J_0(K_{\rho_n}^a b) + C_n N_0(K_{\rho_n}^a b) = 0 \tag{4.12}$$

Let us define a new constant, D_n, such that,

$$B_n = D_n N_0(K_{\rho_n}^a b) \tag{4.13}$$

and

$$C_n = -D_n J_0(K_{\rho_n}^a b) \tag{4.14}$$

Using equations (4.12), (4.13), and (4.14), one can write,

$$N_0(K^a_{\rho_n}b)J_0(K^a_{\rho_n}a) - J_0(K^a_{\rho_n}b)N_0(K^a_{\rho_n}a) = 0 \tag{4.15}$$

Equation (4.15) has the same form as the standard equation,

$$N_0(x)J_0(gx) - J_0(x)N_0(gx) = 0 \tag{4.16}$$

with solution, x^a_n. For equation (4.15) to be true, let $g = \frac{a}{b}$, then the wave number in region (a), $K^a_{\rho_n}$, must be given by,

$$K^a_{\rho_n} = \frac{x^a_n}{b} \quad , \quad n > 0 \tag{4.17}$$

The scalar function, Ψ^a, given in equation (4.10), can now be rewritten using equations (4.13) and (4.14) as,

$$\Psi^a = (B_0 + C_0 \ln \rho)e^{jK_0z} + \sum_{n=1}^{\infty}\left[D_nN_0(K^a_{\rho_n}b)J_0(K^a_{\rho_n}\rho) - J_0(K^a_{\rho_n}b)N_0(K^a_{\rho_n}\rho)\right]e^{jK^a_{z_n}z} \tag{4.18}$$

Using equations (4.5), (4.7), and (4.18), the electric and magnetic fields due to M can be written as,

$$E^a_\rho(M) = \frac{A^a_0}{\rho}e^{jk_0z} + \sum_{n=1}^{\infty}A^a_nf^a_n(\rho)e^{jK^a_{z_n}z} \tag{4.19}$$

and

$$H^a_\phi(M) = -\frac{A^a_0}{\eta^a_0\rho}e^{jk_0z} - \sum_{n=1}^{\infty}\frac{A^a_n}{\eta^a_n}f^a_n(\rho)e^{jK^a_{z_n}z} \tag{4.20}$$

where $A_0^a = \eta_0^a C_0$, $A_n^a = \dfrac{K_{\rho_n}^a K_{z_n}^a D_n}{\omega\varepsilon_0}$, $\eta_n^a = \dfrac{K_{z_n}^a}{\omega\varepsilon_0}$, and

$$f_n^a(\rho) = J_0(K_{\rho_n}^a b)N_1(K_{\rho_n}^a \rho) - N_0(K_{\rho_n}^a b)J_1(K_{\rho_n}^a \rho) \tag{4.21}$$

where J_1 and N_1 are the first order Bessel functions of the first and second kind, respectively. Note that $f_n^a(\rho)$ is orthogonal to $f_m^a(\rho)$ for $n > 0$. To make the computation easier, let us normalize $f_n^a(\rho)$ for unity power and define it as,

$$f_n^a(\rho) = \frac{e_n^a(\rho)}{P_n^a} \tag{4.22}$$

where $e_n^a(\rho)$ satisfies the orthonormality relationship

$$\iint_{\text{line-cross section}} e_n^a(\rho) \cdot e_m^a(\rho) ds = \begin{cases} 1 & , \quad n = m \\ 0 & , \quad n \neq m \end{cases} \tag{4.23}$$

The normalizing constant, P_n^a, is evaluated from the following equation,

$$(P_n^a)^2 \int_0^{2\pi} \int_b^a (f_n^a(\rho))^2 \rho \, d\rho d\phi = 1 \tag{4.24}$$

or,

$$\begin{aligned} 2\pi(P_n^a)^2 \int_b^a [J_0^2(K_{\rho_n}^a b)N_1^2(K_{\rho_n}^a \rho) + N_0^2(K_{\rho_n}^a b)J_1^2(K_{\rho_n}^a \rho) \\ - 2J_0(K_{\rho_n}^a b)N_1(K_{\rho_n}^a \rho)N_0(K_{\rho_n}^a b)J_1(K_{\rho_n}^a \rho)]\rho d\rho = 1 \end{aligned} \tag{4.25}$$

Equation (4.25) has three integrals to be evaluated,

$$I_1 = \int_b^a N_1^2(K_{\rho_n}^a \rho)\rho d\rho \ , \tag{4.26}$$

$$I_2 = \int_b^a J_1^2(K_{\rho_n}^a \rho)\rho d\rho \ , \tag{4.27}$$

and

$$I_3 = \int_b^a N_1(K_{\rho_n}^a \rho)J_1(K_{\rho_n}^a \rho)\rho d\rho \tag{4.28}$$

These integrals can be computed using the following general formulas [32],

$$\int_{a1}^{a2} X_1^2(K\rho)\rho d\rho = \frac{\rho^2}{2}\left[X'^2_1(K\rho) + (1 - \frac{1}{K^2\rho^2})X_1^2(K\rho)\right]_{a1}^{a2} \tag{4.29}$$

and

$$\int_{a1}^{a2} X_1(K\rho)Y_1(K\rho)\rho d\rho = \frac{\rho^2}{2}\left[X'_1(K\rho)Y'_1(K\rho) + (1 - \frac{1}{K^2\rho^2})X_1(K\rho)Y_1(K\rho)\right]_{a1}^{a2} \tag{4.30}$$

where X and/or Y can be a first and/or a second kind Bessel function, K is a non-zero constant, and prime denotes differentiation with respect to the argument, or,

$$X'_1(K\rho) = X_0(K\rho) - \frac{1}{K\rho}X_1(K\rho) \tag{4.31}$$

Using equations (4.29) - (4.31) integrals I_1, I_2, and I_3 will have the following results,

$$I_1 = \frac{a^2}{2}\left[N_0^2(K_{\rho_n}^a a) - \frac{2}{K_{\rho_n}^a a} N_1(K_{\rho_n}^a a)N_0(K_{\rho_n}^a a) + N_1^2(K_{\rho_n}^a a)\right] - \frac{b^2}{2}\left[N_0^2(K_{\rho_n}^a b) - \frac{2}{K_{\rho_n}^a b} N_1(K_{\rho_n}^a b)N_0(K_{\rho_n}^a b) + N_1^2(K_{\rho_n}^a b)\right] \tag{4.32}$$

$$I_2 = \frac{a^2}{2}\left[J_0^2(K_{\rho_n}^a a) - \frac{2}{K_{\rho_n}^a a} J_1(K_{\rho_n}^a a)J_0(K_{\rho_n}^a a) + J_1^2(K_{\rho_n}^a a)\right] - \frac{b^2}{2}\left[J_0^2(K_{\rho_n}^a b) - \frac{2}{K_{\rho_n}^a b} J_1(K_{\rho_n}^a b)J_0(K_{\rho_n}^a b) + J_1^2(K_{\rho_n}^a b)\right] \tag{4.33}$$

and

$$\begin{aligned} I_3 = {} & \frac{a^2}{2}\left[J_0(K_{\rho_n}^a a)N_0(K_{\rho_n}^a a) + J_1(K_{\rho_n}^a a)N_1(K_{\rho_n}^a a)\right] \\ & - \frac{a}{2K_{\rho_n}^a}\left[J_0(K_{\rho_n}^a a)N_1(K_{\rho_n}^a a) + J_1(K_{\rho_n}^a a)N_0(K_{\rho_n}^a a)\right] \\ & - \frac{b^2}{2}\left[J_0(K_{\rho_n}^a b)N_0(K_{\rho_n}^a b) + J_1(K_{\rho_n}^a b)N_1(K_{\rho_n}^a b)\right] \\ & + \frac{b}{2K_{\rho_n}^a}\left[J_0(K_{\rho_n}^a b)N_1(K_{\rho_n}^a b) + J_1(K_{\rho_n}^a b)N_0(K_{\rho_n}^a b)\right] \end{aligned} \tag{4.34}$$

Using equations (4.25) and (4.32) - (4.34) and after some algebraic manipulation, the normalizing constant P_n^a can be evaluated as,

$$P_n^a = \frac{1}{\left\{\pi\left[(\alpha_n^a)^2 - (\beta_n^a)^2\right]\right\}^{1/2}} \tag{4.35}$$

where,

$$\alpha_n^a = a\left[J_0(K_{\rho_n}^a b)N_1(K_{\rho_n}^a a) - N_0(K_{\rho_n}^a b)J_1(K_{\rho_n}^a a)\right] \tag{4.36}$$

and

$$\beta_n^a = b\left[J_0(K_{\rho_n}^a b)N_1(K_{\rho_n}^a b) - N_0(K_{\rho_n}^a b)J_1(K_{\rho_n}^a b)\right] \tag{4.37}$$

With P_n^a defined in equations (4.35) - (4.37) and for $n > 0$ $e_n^a(\rho)$ is given by,

$$e_n^a(\rho) = P_n^a\left[J_0(K_{\rho_n}^a b)N_1(K_{\rho_n}^a \rho) - N_0(K_{\rho_n}^a b)J_1(K_{\rho_n}^a \rho)\right] \quad , \quad n > 0 \tag{4.38}$$

Equations (4.19) and (4.20) can be rewritten as,

$$E_\rho^a(M) = A_0^a e_0^a(\rho)e^{jk_0 z} + \sum_{n=1}^{\infty} A_n^a e_n^a(\rho)e^{jK_{z_n}^a z} \tag{4.39}$$

and

$$H_\phi^a(M) = -\frac{A_0^a}{\eta_0^a} e_0^a(\rho)e^{jk_0 z} - \sum_{n=1}^{\infty} \frac{A_n^a}{\eta_n^a} e_n^a(\rho)e^{jK_{z_n}^a z} \tag{4.40}$$

where $e_0^a(\rho)$ is given by,

$$e_0^a(\rho) = \frac{1}{\rho\sqrt{2\pi \ln(a/b)}} \quad , \tag{4.41}$$

$e_n(\rho)$ for $n > 0$ is given by equation (4.38), and constants A_0^a and A_n^a (which have different definitions than the ones in equations (4.19) and (4.20)) are evaluated by applying the remaining boundary condition. This condition is, the tangential component of the electric field over the aperture equals the magnetic current distribution on the aperture, M,

$$M = u_z \times E_t^a(M) \tag{4.42}$$

where (×) stands for vector cross product.

Let us evaluate the tangential components of the electric and magnetic fields over the aperture as,

$$E_t^a(M) = E_\rho^a(M)\,|_{z=0} = A_0^a e_0^a(\rho)u_\rho + \sum_{n=1}^{\infty} A_n^a e_n^a(\rho)u_\rho \tag{4.43}$$

and

$$H_t^a(M) = H_\phi^a(M)\,|_{z=0} = -\frac{A_0^a}{\eta_0^a} e_0^a(\rho)u_\phi - \sum_{n=1}^{\infty} \frac{A_n^a}{\eta_n^a} e_n^a(\rho)u_\phi \tag{4.44}$$

Now we can evaluate M from equations (4.42) and (4.43) as,

$$\begin{aligned} M &= A_0^a e_0^a(\rho)u_\phi + \sum_{n=1}^{\infty} A_n^a e_n^a(\rho)u_\phi \\ &= M_\phi u_\phi \end{aligned} \tag{4.45}$$

Solving for the coefficients in the first equality of the last equation can be done by multiplying both sides of the equality by e_m^* ($m = 0,1,2,\ldots$) and integrating over the line cross section. With the aid of the orthonormality relationship given in equation (4.23) we end up with the following definition for the constants A_n^* , $n \geq 0$,

$$A_n^a = 2\pi \int_b^a M_\phi e_n^a(\rho)\rho d\rho \quad , \quad n = 0,1,2,\ldots \tag{4.46}$$

Now, the tangential component of the magnetic field over the aperture in region (a), $H_t^a(M)$, is given by equation (4.44) with the constants defined in equation (4.46).

(2) Coaxial Cavity Region, (b)

Applying the procedure used in part (1), we choose the following scalar function, Ψ^b, to derive $H_t^b(M)$ interms of M,

$$\Psi^b = (B_0 + C_0 \ln \rho) \cos K_0^b(z-d) + \sum_{n=1}^{\infty} D_n\left[N_0(K_{\rho_n}^b b)J_0(K_{\rho_n}^b \rho) - J_0(K_{\rho_n}^b b)N_0(K_{\rho_n}^b \rho)\right] \cos K_{z_n}^b(z-d) \tag{4.47}$$

K_0^b, $K_{\rho_n}^b$, and $K_{z_n}^b$ are related to each other by the separation equation,

$$(K_{z_n}^b)^2 + (K_{\rho_n}^b)^2 = (K_0^b)^2 = \omega^2 \varepsilon_r^* \mu_r^* \varepsilon_0 \mu_0 \tag{4.48}$$

Ψ^b is chosen such that it satisfies the first boundary condition, zero tangential component of the electric field at $\rho = R$ and $\rho = b$. This condition is satisfied when the wave number in region (b), $K_{\rho_n}^b$, is given by,

$$K_{\rho_n}^b = \frac{x_n^b}{b} \quad , \quad n > 0 \tag{4.49}$$

where x_n^b is the solution of,

$$N_0(x)J_0\left(\frac{R}{b}x\right) - J_0(x)N_0\left(\frac{R}{b}x\right) = 0 \tag{4.50}$$

Using equations (4.5), (4.7), and (4.47), the magnetic and electric fields duo to $-M$ can be written as,

$$E_\rho^b(-M) = \frac{A_0^b}{\rho}\sin K_0^b(z-d) + \sum_{n=1}^{\infty} A_n^b f_n^b(\rho)\sin K_{z_n}^b(z-d) \tag{4.51}$$

and

$$H_\phi^b(-M) = \frac{A_0^b}{\eta_0^b\,\rho}\cos K_0^b(z-d) + \sum_{n=1}^{\infty}\frac{A_n^b}{\eta_n^b} f_n^b(\rho)\cos K_{z_n}^a(z-d) \tag{4.52}$$

where

$$\eta_n^b = \frac{K_{z_n}^b}{j\omega\varepsilon_r^{\,*}\varepsilon_0}\quad , \tag{4.53}$$

$$\eta_0^b = -j\sqrt{\frac{\mu_r^{\,*}\mu_0}{\varepsilon_r^{\,*}\varepsilon_0}}\quad , \tag{4.54}$$

and

$$f_n^b(\rho) = J_0(K_{\rho_n}^b b)N_1(K_{\rho_n}^b\rho) - N_0(K_{\rho_n}^b b)J_1(K_{\rho_n}^b\rho) \tag{4.55}$$

The coefficients A_0^b and A_n^b will be evaluated later.

Using the orthonormality criterion as in part (1), we will get the following results,

$$f_n^b(\rho) = \frac{e_n^b(\rho)}{P_n^b} \tag{4.56}$$

where,

$$\iint_{\text{cavity cross section}} e_n^b(\rho) \cdot e_m^b(\rho) ds = \begin{cases} 1 & , \quad n = m \\ 0 & , \quad n \neq m \end{cases} \tag{4.57}$$

and

$$P_n^b = \frac{1}{\left\{\pi\left[(\alpha_n^b)^2 - (\beta_n^b)^2\right]\right\}^{1/2}} \tag{4.58}$$

where,

$$\alpha_n^b = R\left[J_0(K_{\rho_n}^b b) N_1(K_{\rho_n}^b R) - N_0(K_{\rho_n}^b b) J_1(K_{\rho_n}^b R)\right] \tag{4.59}$$

and

$$\beta_n^b = b\left[J_0(K_{\rho_n}^b b) N_1(K_{\rho_n}^b b) - N_0(K_{\rho_n}^b b) J_1(K_{\rho_n}^b b)\right] \tag{4.60}$$

Equations (4.51) and (4.52) can be rewritten as,

$$E_\rho^b(-M) = A_0^b e_0^b(\rho) \sin K_0^b(z-d) + \sum_{n=1}^{\infty} A_n^b e_n^b(\rho) \sin K_{z_n}^b(z-d) \tag{4.61}$$

and

$$H_\phi^b(-M) = \frac{A_0^b}{\eta_0^b} e_0^b(\rho) \cos K_0^b(z-d) + \sum_{n=1}^{\infty} \frac{A_n^b}{\eta_n^b} e_n^b(\rho) \cos K_{z_n}^a(z-d) \tag{4.62}$$

where,

$$e_0^b(\rho) = \frac{1}{\rho\sqrt{2\pi \ln(R/b)}} \tag{4.63}$$

while e_n^b , $n > 0$ can be evaluated from equation (4.56). The coefficients A_0^b and A_n^b are evaluated by applying the remaining boundary condition. This condition is, the tangential component of the electric field over the aperture equals the magnetic current distribution on the aperture, $-M$,

$$\begin{aligned} -M &= -u_z \times E_t^b(-M) \\ &= -M_\phi u_\phi \end{aligned} \tag{4.64}$$

The tangential component of the electric field over the aperture is given by,

$$E_t^b(-M) = E_\rho^b(-M)\,|_{z=0} = -A_0^b e_0^b(\rho)\sin(K_0^b d)\,u_\rho - \sum_{n=1}^{\infty} A_n^b e_n^b(\rho)\sin(K_{z_n}^b d)\,u_\rho \tag{4.65}$$

Equations (4.64) and (4.65) yield,

$$M_\phi = -A_0^b e_0^b(\rho)\sin(K_0^b d) - \sum_{n=1}^{\infty} A_n^b e_n^b(\rho)\sin(K_{z_n}^b d) \tag{4.66}$$

Multiply both sides of equation (4.65) by e_m^b ($m = 0,1,2, \ldots$) and integrate over the cavity cross section to get,

$$\begin{aligned} \int_0^{2\pi}\int_b^R M_\phi e_m^b(\rho)\rho d\rho d\phi = &-\int_0^{2\pi}\int_b^R A_0^b e_0^b(\rho) e_m^b(\rho)\sin(K_0^b d)\rho d\rho d\phi \\ &-\sum_{n=1}^{\infty}\int_0^{2\pi}\int_b^R A_n^b e_n^b(\rho) e_m^b(\rho)\sin(K_{z_n}^b d)\rho d\rho d\phi \end{aligned} \tag{4.67}$$

The last equation will be simplified with the aid of two facts. The orthonormality relationship given in equation (4.57). The other fact is that M is defined only on the aperture which means that $M = 0$ for $\rho > a$. The coefficients A_0^b and A_n^b will be given by,

$$A_0^b = \frac{-2\pi}{\sin K_0^b d} \int_b^a M_\phi e_0^b(\rho) \rho d\rho \tag{4.68}$$

and

$$A_n^b = \frac{-2\pi}{\sin K_{z_n}^b d} \int_b^a M_\phi e_n^b(\rho) \rho d\rho \quad , \quad n \geq 1 \tag{4.69}$$

Now, the tangential component of the magnetic field over the aperture in region (b), $H_t^b(M)$, is given by,

$$H_t^b(M) = -H_\phi^b(-M)\,|_{z=0} = -\frac{A_0^b}{\eta_0^b} e_0^b(\rho) \cos(K_0^b d) u_\phi - \sum_{n=1}^{\infty} \frac{A_n^b}{\eta_n^b} e_n^b(\rho) \cos(K_{z_n}^a d) u_\phi \tag{4.70}$$

with the coefficients A_0^b and A_n^b given by equations (4.68) and (4.69)

(3) Solution by Method of Moments

Method of moments is used to obtain an approximate solution for equation (4.3) which is rewritten here for convenience,

$$H_t^a(M) + H_t^b(M) = -2H_t^I \tag{4.3}$$

The quantities in this equation are obtained as functions of M in the last two parts (equations (4.44), (4.71), and (4.9)). The exact solution of M from this equation is impossible to obtain, hence the method of moments is used. The method of moments starts with writing M as a sum of an independent set of expansion functions $\{M_i,\ i = 1,2, \ldots, N_1\}$,

$$M = \sum_{i=1}^{N_1} V_i M_i \tag{4.72}$$

with the coefficients V_i to be determined later. Equation (4.3) is rewritten using equation (4.72) and linearity of the magnetic field as,

$$\sum_{i=1}^{N_1} V_i H_t^a(M_i) + \sum_{i=1}^{N_1} V_i H_t^b(M_i) = -2H_t^i \tag{4.73}$$

The symmetric product defined as,

$$<A,B> = \iint_{aperture} A \bullet B \, ds \tag{4.74}$$

is used to simplify the notation throughout this part. The next step is to take the symmetric product of equation (4.73) with each function, W_j, of an independent set of weighting functions $\{W_j,\ j = 1,2, \ldots, N_2\}$. Using the linearity of the symmetric product, one can write,

$$\sum_{i=1}^{N_1} V_i <W_j, H_t^a(M_i)> + \sum_{i=1}^{N_1} V_i <W_j, H_t^b(M_i)> = -2<W_j, H_t^i> \quad , \ j = 1,2, \ldots, N_2 \tag{4.75}$$

The last set of linear equations are solved to determine the coefficients V_i which are used to evaluate M using equation (4.72). Using Galerkin's method, the set of weighting functions is chosen to be identical to the set of expansion functions, or, $\{W_j \equiv M_i,\ i=j=1,2,\ldots,N\}$. With this choice, the last set of linear equations can be written in matrix form as,

$$[Y^a + Y^b]\vec{V} = \vec{I} \tag{4.76}$$

where $[Y^a]$ is the admittance matrix representing region (a),

$$[Y^a] = [< -M_j, H_t^a(M_i) >]_{N\times N} \tag{4.77}$$

and $[Y^b]$ is the admittance matrix representing region (b),

$$[Y^b] = [< -M_j, H_t^b(M_i) >]_{N\times N} \tag{4.78}$$

while $\vec{I}$ is the source vector given by

$$\vec{I} = [< 2M_j, H_t^i >]_{N\times 1} \tag{4.79}$$

and $\vec{V}$ is the coefficient vector given by

$$\vec{V} = [V_i]_{N\times 1} \tag{4.80}$$

The only unknown in equation (4.76) is the vector $\vec{V}$.

The next step is to choose a set of expansion functions that best approximates the actual magnetic current distribution over the aperture, M. A good choice is the modes of the transmission line region. Thus, let

$$M_i = e^a_{i-1} \quad , \quad i = 1,2, \ldots ,N \tag{4.81}$$

where e^a_i , $i \geq 0$ is given in equations (4.38) and (4.41). The elements of the matrix equation (4.76) can be evaluated by taking each expansion function M_j individually across the aperture. Let's start computing the elements of the admittance matrix $[Y^a]$. This computation starts with rewriting equation (4.46) to account for the added subscript on M as,

$$A^a_{ni} = 2\pi \int_b^a M_i e^a_n(\rho)\rho d\rho \quad , \quad n = 0,1,2, \ldots ,\infty \quad , \quad i = 0,1,2, \ldots ,N \tag{4.82}$$

From equation (4.81) and the orthonormality relationship given in equation (4.23), equation (4.82) is reduced to,

$$A^a_{ni} = \begin{cases} 1 & , \quad n = i \\ 0 & , \quad n \neq i \end{cases} \tag{4.83}$$

Thus, using equations (4.44), (4.77), (4.81), (4.82), and (4.83) the elements of the admittance matrix $[Y^a]$ are given by,

$$Y^a_{ij} = \begin{cases} \dfrac{1}{\eta^a_{i-1}} & , \quad i = j \\ 0 & , \quad i \neq j \end{cases} \quad , \quad i,j = 1,2, \ldots ,N \tag{4.84}$$

Now we start computing the elements of the admittance matrix in region (b), Y^b_{ij}, with rewriting equations (4.68) and (4.69) as,

$$A^b_{0i} = \frac{-2\pi}{\sin K^b_0 d} \int_b^a M_i e^b_0(\rho)\rho d\rho \quad , \quad i = 1,2, \ldots ,N \tag{4.85}$$

and

$$A_{ni}^{b} = \frac{-2\pi}{\sin K_{z_n}^{b} d} \int_{b}^{a} M_i e_n(\rho)\rho d\rho \quad , \quad n \geq 1 \ , \quad i = 1,2, \ldots ,N \tag{4.86}$$

These equations can be evaluated using the general formula given in equation (4.31) and the following general formulas,

$$\int_{a1}^{a2} X_1(K\rho)d\rho = -X_0(K\rho)\Big|_{a1}^{a2} \tag{4.87}$$

where X can be a first or second kind Bessel function, and

$$\int_{a1}^{a2} X_1(K_1\rho)Y_1(K_2\rho)\rho d\rho = \frac{1}{K_1^2 - K_2^2}\left[K_2\rho X_1(K_1\rho)Y'_1(K_2\rho) - K_1\rho X'_1(K_1\rho)Y_1(K_2\rho)\right]_{a1}^{a2} \tag{4.88}$$

Equation (4.85) is evaluated for $i = 1$ and $i = 2,3, \ldots ,N$ using equations (4.63), orthonormality relationship (4.57), and (4.81) as follows,

$$A_{01}^{b} = \frac{-\sqrt{\ln(a/b)}}{\sin(K_0^{b} d)\ln(R/b)} \tag{4.89}$$

and

$$A_{0i}^{b} = 0 \quad , \quad i = 2,3, \ldots ,N \tag{4.90}$$

Equation (4.86) is evaluated for $i = 1$ using equations (4.41) and (4.56) to get,

$$A_{n1}^{b} = \frac{P_n^{b} Q_n^{b}}{K_{\rho_n}^{b} \sin(K_{z_n}^{b} d)} \sqrt{\frac{2\pi}{\ln(a/b)}} \quad , \quad n = 1,2, \ldots ,\infty \tag{4.91}$$

where

$$Q_n^b = J_0(K_{\rho_n}^b b)N_0(K_{\rho_n}^b a) - N_0(K_{\rho_n}^b b)J_1(K_{\rho_n}^b a) \tag{4.92}$$

For $i = 2,3, \ldots, N$ equation (4.86) is evaluated using equations (4.38) and (4.56) to get,

$$A_{ni}^b = -\frac{2\pi P_i^a P_n^b K_{\rho_n}^b \alpha_i^a Q_n^b}{\sin(K_{z_n}^b d)\left[(K_{\rho_i}^a)^2 - (K_{\rho_n}^b)^2\right]} \quad , \; n = 1,2, \ldots, \infty \; , \; i = 2,3, \ldots, N \tag{4.93}$$

If $K_{\rho_i}^a$ equals $K_{\rho_n}^b$, then A_{ni}^b is evaluated as,

$$A_{ni}^b = \frac{\pi P_i^a P_n^b\left[\beta_n^b \beta_i^a - (\alpha_i^a)^2\right]}{\sin(K_{z_n}^b d)} \quad , \; n = 1,2, \ldots, \infty \; , \; i = 2,3, \ldots, N \tag{4.94}$$

Thus, using equations (4.70), (4.78), (4.81), (4.85), and (4.86) the elements of the admittance matrix $[Y^b]$ are evaluated as,

$$\begin{aligned} Y_{ij}^b &= -2\pi \int_b^a M_j H^{bt}(M_i)\rho d\rho \\ &= 2\pi \frac{A_{0i}^b}{\eta_0^b} \cos(K_0^b d) \int_b^a M_j e_0^b(\rho)\rho d\rho + 2\pi \sum_{n=1}^{\infty} \frac{A_{ni}^b}{\eta_n^b} \cos(K_{z_n}^b d) \int_b^a M_j e_n^b(\rho)\rho d\rho \end{aligned}$$

Thus

$$Y_{ij}^b = -\frac{\cos(K_0^b d)\sin(K_0^b d)}{\eta_0^b} A_{0i}^b A_{0j}^b - \sum_{n=1}^{\infty} \frac{\cos(K_{z_n}^b d)\sin(K_{z_n}^b d)}{\eta_n^b} A_{ni}^b A_{nj}^b \quad , \; i,j = 1,2, \ldots, N \tag{4.95}$$

The elements of the source vector $\vec{I}$ are evaluated using equations (4.9), (4.79), and (4.81) as,

$$\vec{I}_j = \begin{Bmatrix} \frac{2}{\eta_0^a} & , & j=1 \\ 0 & , & j>1 \end{Bmatrix} \tag{4.96}$$

Equations (4.70), (4.84), (4.95), and (4.96) are used to evaluate the coefficient vector, $\vec{V}$, and then the magnetic current, M, is evaluated using equation (4.72).

To evaluate the reflection coefficient, S_{11}, we first write the tangential electric field over the aperture as,

$$E_\rho^a|_{z=0} = (1+S_{11})e_0^a(\rho)\,u_\rho + \sum_{n=1}^{\infty}\Gamma_n e_n^a(\rho)\,u_\rho \tag{4.97}$$

where Γ_i are the amplitudes of the higher order modes generated at the aperture (unity incident power is assumed) [29]. Using equations (4.42) and (4.97) and the fact that $M = M_\phi u_\phi$, one can write

$$M_\phi = (1+S_{11})e_0^a(\rho) + \sum_{n=1}^{\infty}\Gamma_n e_n^a(\rho) \tag{4.98}$$

To evaluate S_{11}, multiply both sides of equation (4.98) by $e_0^a(\rho)$ and integrate over the aperture to get,

$$S_{11} = \int_0^{2\pi}\int_b^a M_\phi e_0^a(\rho)\rho d\rho d\phi \; - 1 \tag{4.99}$$

The last equation is obtained after using the orthonormality relationship (4.23). Substituting equation (4.72) in equation (4.99) results in,

$$S_{11} = \sum_{i=1}^{N} V_i \int_0^{2\pi} \int_b^a M_i e_0^a(\rho) \rho d\rho d\phi - 1 \tag{4.100}$$

Using equations (4.23) and (4.81), the last equation is reduced to,

$$S_{11} = V_1 - 1 \tag{4.101}$$

The equations obtained in this subsection are implemented in a Fortran program given in Appendix 1. This program is used to study the effect of varying the dimensions of the sample holder as well as the dielectric and magnetic properties of the material on the reflection coefficient. This study is performed in section 4.3.

4.2.3 COMPUTATION OF μ_r^* FROM $S_{11}(j\omega)$ MEASUREMENT

In this subsection, the permeability of the ferrite is computed assuming S_{11} is known. Equation (4.101) is rewritten as the difference between two quantities,

$$S_{11} - (V_1 - 1) = 0 \tag{4.102}$$

Equation (4.95) is a nonlinear one in μ_r^* and it is used to arrive to equation (4.102). This necessitates an iterative solution to equation (4.102). This is achieved by minimizing the real and imaginary parts of the following function,

$$f(\mu_r^*) = S_{11} - (V_1 - 1) \tag{4.103}$$

To do this an initial value of μ_r^* is assumed, then V_1 is evaluated as described in the preceding subsection. The function given in equation (4.103) is evaluated and used to update μ_r^* using a nonlinear optimization method [33]. The updated value of μ_r^* is

used again in the same procedure to get a newer value of μ_r^*. This procedure is repeated until a desired value of $f(\mu_r^*)$ is obtained. The equations obtained in this subsection are implemented in a Fortran program given in Appendix 2. This program is used to estimate the relative permeability and magnetic loss of ferrite materials.

4.3 COMPUTER SIMULATION RESULTS

The effect of varying the electric and magnetic properties of the sample as well as the dimensions of the cavity on the reflection coefficient is studied in this section. Throughout this section these values are assumed unless otherwise mentioned, cavity radius of 1 cm, sample thickness of 0.005 cm, magnetic loss of 0, real part of permeability, μ'_r, of 5, real part of permittivity, ε'_r, of 5, and dielectric loss of 0. The assumption of zero dielectric and magnetic losses results in unity reflection coefficient magnitude. Then the effect of varying different parameters is studied through the phase of the reflection coefficient.

4.3.1 VARYING THE REAL PART OF PERMITIVITY ε'_r

Three values of ε'_r are used in this subsection, 1, 10, and 20. The corresponding phase of S_{11} for each value of ε'_r is illustrated in Figure (4.3). The conclusion that can be drawn from Figure (4.3) is that, varying the real part of permittivity will not have major effect on the phase of $S_{11}(j\omega)$, or the resonance of the cavity. This proves that assuming a reasonable value for the real part of permittivity in obtaining μ_r^* from $S_{11}(j\omega)$ measurements will not effect the accuracy of μ_r^* values.

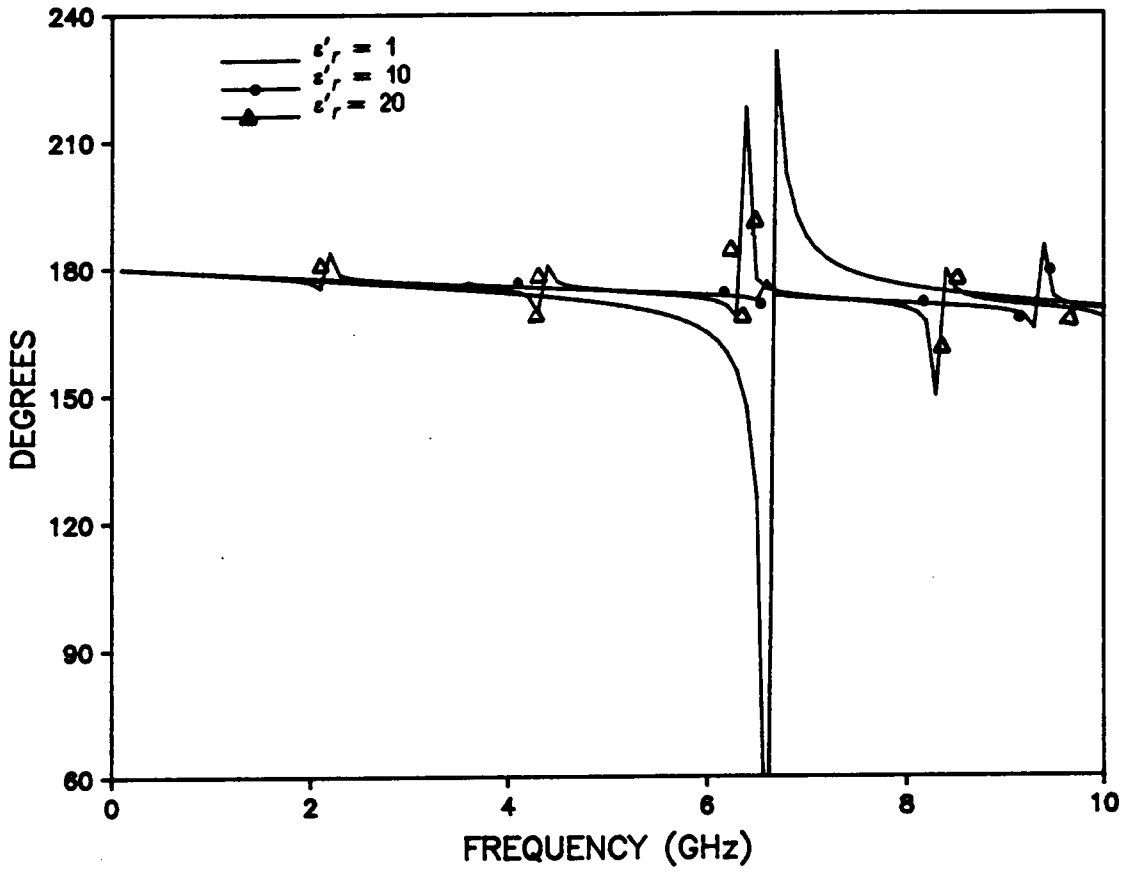

Figure (4.3). Phase of S_{11} corresponding to different values of real part of permittivity ε'_r.

4.3.2 VARYING THE REAL PART OF PERMEABILITY μ'_r

In this subsection, the value of μ'_r is assumed to be, 1, 10, and 20. Figure (4.4) illustrates the effect of using these values of μ'_r,on the the phase of the reflection coefficient. It is observed that varying μ'_r changes the phase as well as the resonant frequencies of the cavity. Hence it is obvious that it is feasible to estimate μ'_r over a very wide band of frequencies.

4.3.3 VARYING THE MAGNETIC LOSS μ''_r

Figures (4.5) and (4.6) illustrates the effect of varying the magnetic loss on the magnitude and phase of reflection coefficient. The values of μ''_r used in this subsection are, 0.1, 1, 10. The conclusion from these two figures is that varying the magnetic loss effects the magnitude of the reflection coefficient more than it does to the phase.

4.3.4 VARYING THE OUTER RADIUS OF THE CAVITY

Three values of the outer radius are used in this subsection, 0.5 cm, 1 cm, 1.5 cm. Figure (4.7) illustrates the effect of varying the outer radius of the outer radius of the cavity on the reflection coefficient. It is obvious from Figure (4.7) that the only effect of varying the outer radius is on the number and locations of resonances. It is concluded that the larger the outer radius the more resonances are produced in the bandwidth of interest.

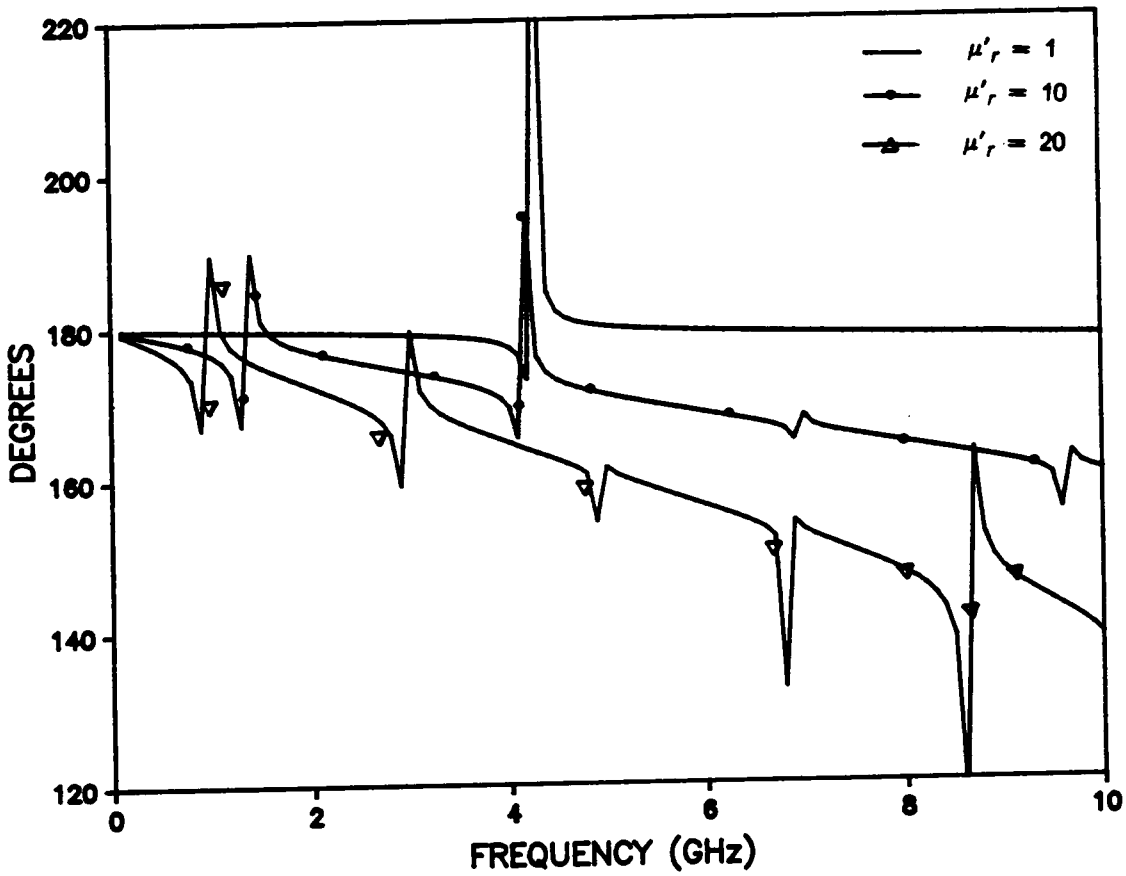

Figure (4.4). Phase of S_{11} corresponding to different values of real part of permeability μ'_r.

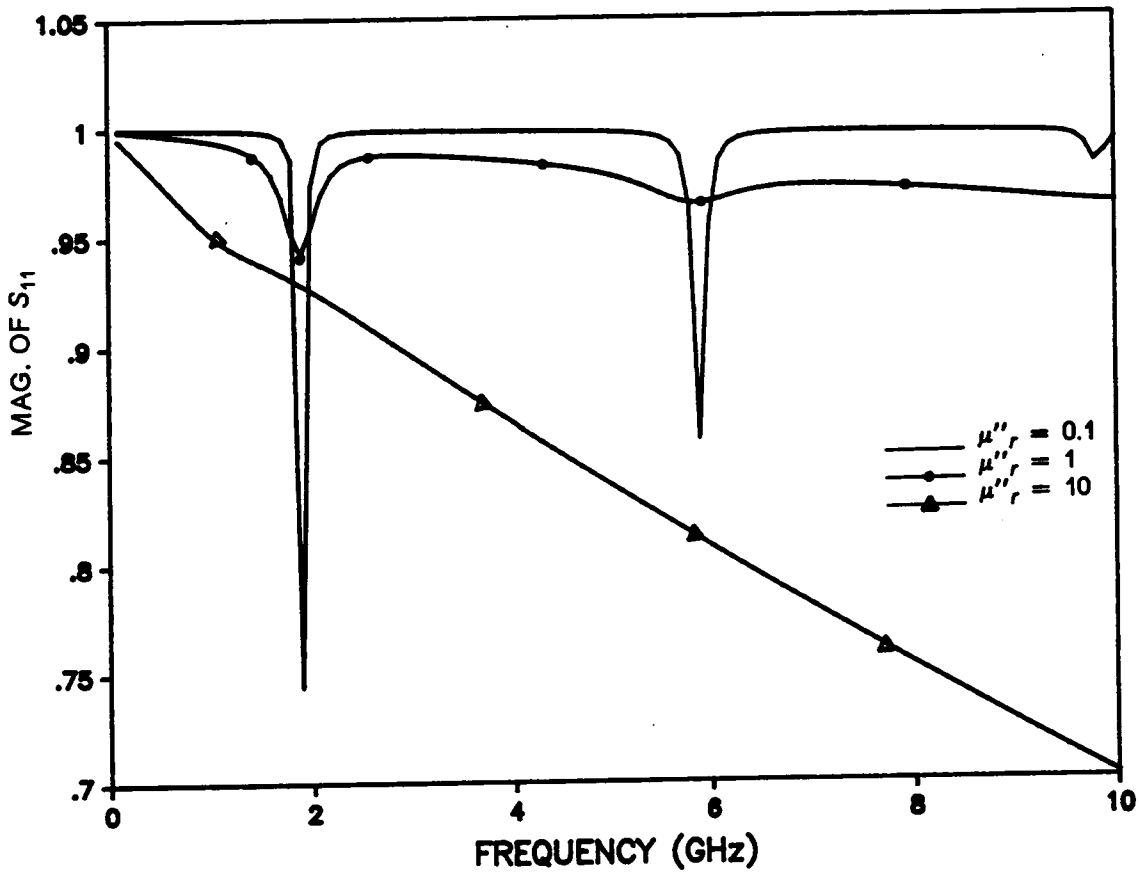

Figure (4.5). Effect of varying the magnetic loss, μ''_r, on the magnitude of S_{11}

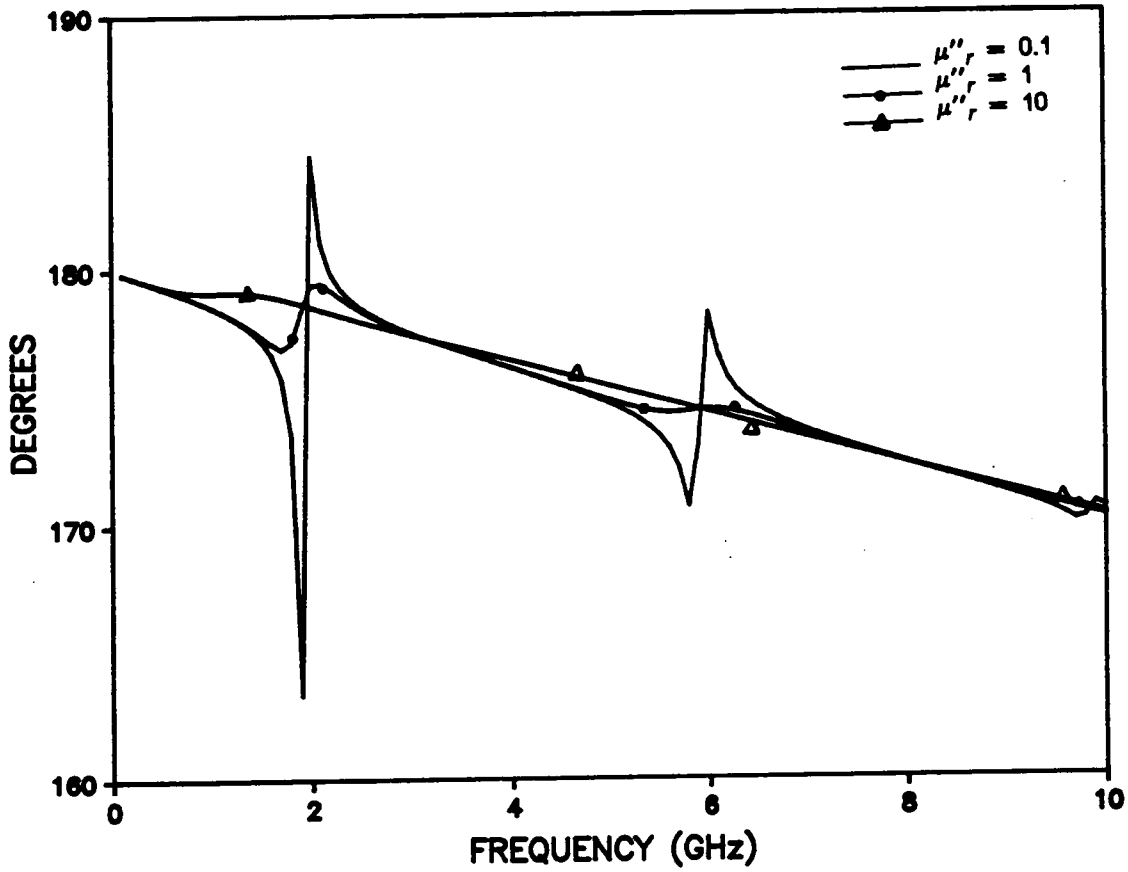

Figure (4.6). Effect of varying the magnetic loss, μ''_r, on the phase of S_{11}

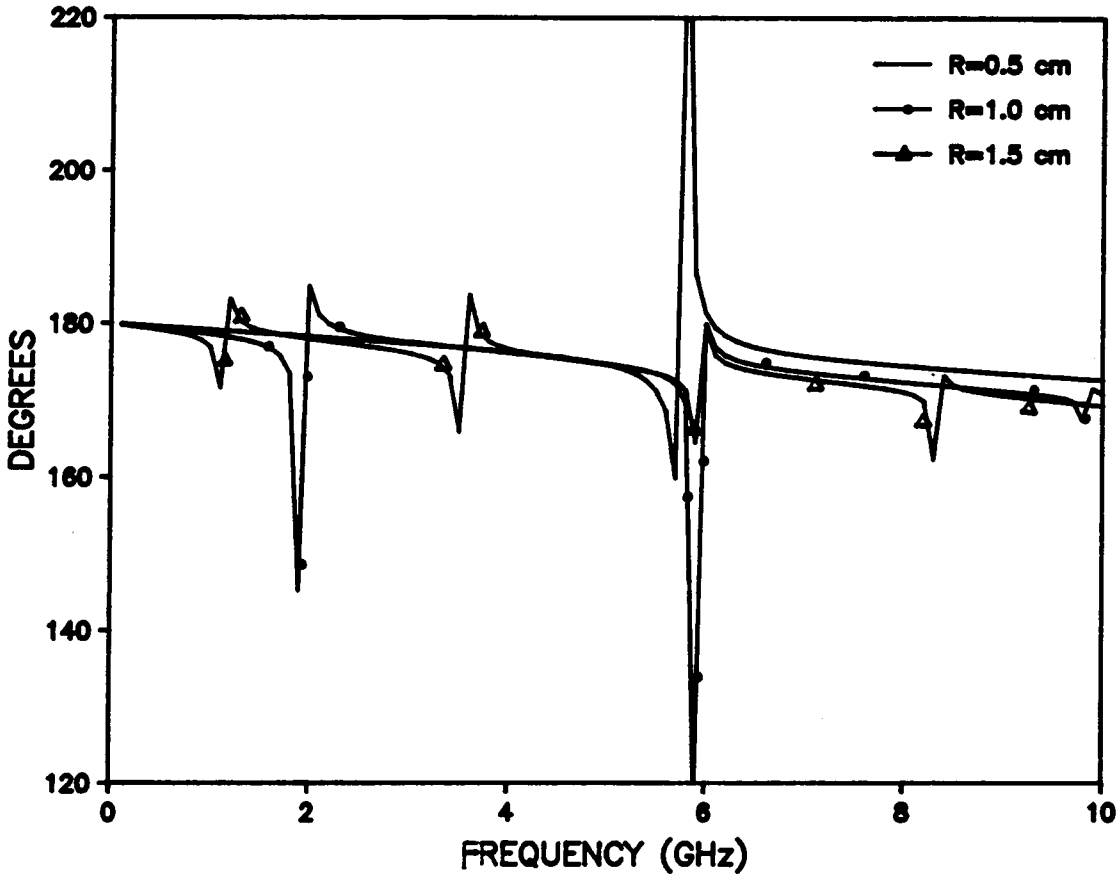

Figure (4.7). Effect of varying the outer radius of the cavity on the phase of S_{11}

4.3.5 VARYING THE SAMPLE THICKNESS

In this subsection, ε'_r equals to 1.0 and μ'_r equals to 10.0, while thicknesses of 0.0025 cm, 0.005 cm, and 0.0075 cm are assumed. Figure (4.8) illustrates the effect of using these thicknesses on the the phase of the reflection coefficient. It is observed from Figure (4.8) that thicker samples can yield more accurate results because the sensitivity of the reflection coefficient to frequency is greater for thicker samples, or, the rate of change of the phase with respect to frequency is higher for thicker samples.

4.4 EQUIPMENT, MATERIALS, AND ELEMENTS STRUCTURE

Thick film technology equipment and materials used in the construction of the cavity is the subject of the first subsection. The next subsection concerns with the cavity structure and construction to be used in the wideband characterization. TDR and Frequency Domain measurement equipment will be fully described in section 4.5.

4.4.1 EQUIPMENT AND MATERIALS

An AMI Presco automatic screen printer machine model 435 is used in the printing operation using the single print mode. A screen breakaway distance of 20 mils is used in the printing process. The metalization as well as the ferrite materials are printed using a 325 screen mesh size with a 90° angle, and overall dimensions of 5″ × 5″. The samples are dried in a Blue M oven POM-206B-1 for 15 minutes at

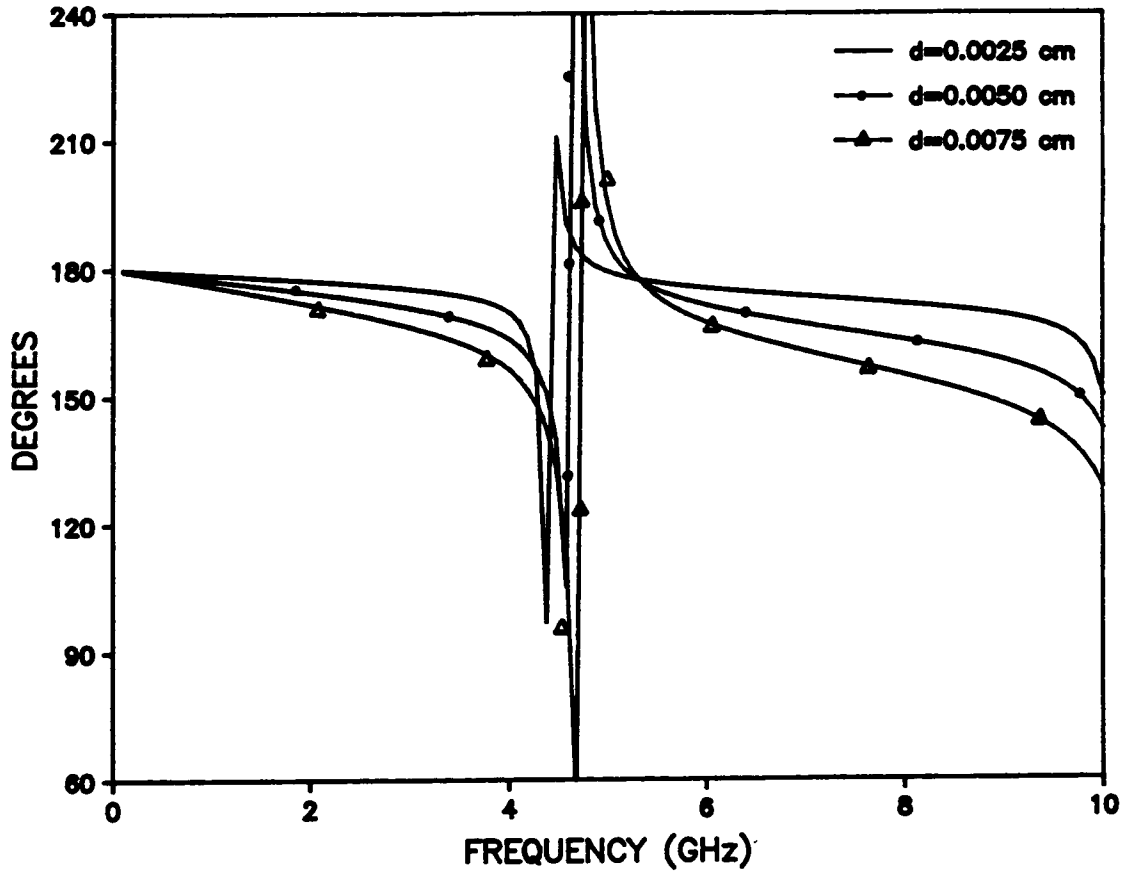

Figure (4.8). Effect of varying the sample thickness on the phase of S_{11}

150° C, and then they are fired in a BTU four-zone belt furnace. The total firing cycle is of the order of 60 minutes, with a 10 minutes at a peak temperature of 850°C.

Electro Scientific Laboratories (ESL) and Remex thick film pastes are utilized in the construction of two groups of cavities. In the first group, ESL ferrite paste EX-2000 and Silver (Ag) conductor paste D9912-F are used. The second group uses Remex ferrite paste 4920 and Palladuim-Silver (Pd-Ag) conductor paste 2042. 3″ × 3″ × 0.025″ , 96% alumina substrates manufactured by Coors Porcelain are used to produce these cavity structures.

4.4.2 CAVITY STRUCTURE AND CONSTRUCTION

The process sequence in manufacturing the sample configuration to characterize the thick film ferrite material consists of constructing a coaxial cavity completely filled with ferrite material. The process sequence consists of four or more printings. This can be summarized as the following,

1. The first layer of metalization is printed directly on the substrate. The metalization is dried and fired.

2. The first layer of ferromagnetic material of the form of coaxial structure is printed on top of the the first metalization layer. The ferrtie layer is dried and fired.

3. The second layer of ferromagnetic material is printed, dried, and fired.

4. The second metalization layer for the coaxial cavity formation is printed last, thus forming the top metalization. The metalization layer is dried and fired.

Step 3 may be repeated as many times as needed to achieve the desired thickness of the ferrite material. Figure (4.1) illustrates the configuration used in the study and analysis. The inner and outer diameters of the cavity are 0.15 &cm. and 1.0 &cm., respectively.

4.5 MEASUREMENT TECHNIQUES

4.5.1 TIME DOMAIN REFLECTOMETRY TECHNIQUE

Time Domain Reflectometry technique is used in this work to acquire the reference and response waveforms needed to compute the reflection coefficient from the cavity under test. Figure (4.9) illustrates the TDR setup used for the measurement of the reference and reflected waveforms. This setup consists of a digitizing oscilloscope interfaced for data acquisition to a personal computer and a TDR unit which has a pulse generator and a feedthrough sampling head. The sample holder is attached to the output port of the TDR unit. The pulse generator used has a spectral contents covering the band from DC to 18 GHz.

In order to measure the reflection coefficient $S_{11}(j\omega)$, two waveforms are acquired. The response waveform $v_{resp}(t)$ which is the reflection from the cavity. The reference waveform $v_{ref}(t)$ which is the negative of the reflection from a precision short. The negative sign results from the fact that an ideal short circuit has a reflection coefficient $S_{11}(j\omega)$ equals to -1. Both reflections are acquired after exciting the termination with a wideband pulse launched from the pulse generator. Both the reference and response waveforms are stored in a form suitable for later use in the

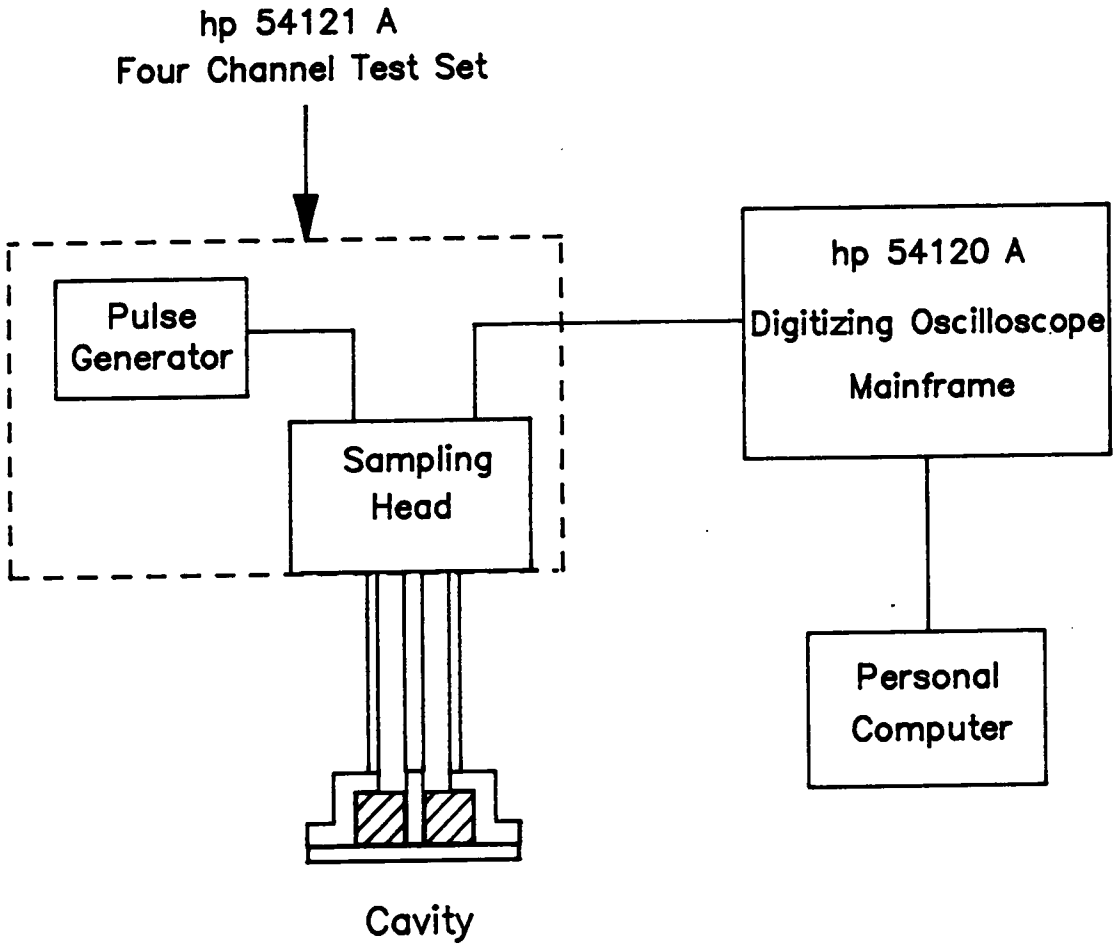

Figure (4.9). TDR setup.

computer simulation program. Figure (4.10) shows a typical reference waveform, $v_{ref}(t)$, while Figure (4.11) shows a reflected waveform, $v_{resp}(t)$, of one the cavities studied by the author.

The reference waveform, $v_{ref}(t)$, is then deconvolved from the response waveform, $v_{resp}(t)$ to compute the reflection coefficient [34]. The two acquired waveforms are transformed into the frequency domain using the Complete Fast Fourier Transform method, CFFT [35]. The reflection coefficient $S_{11}(j\omega)$ is computed as the ratio between the two Fourier Transforms,

$$S_{11}(j\omega) = \frac{V_{resp}(j\omega)}{V_{ref}(j\omega)} \tag{4.104}$$

where $V_{ref}(j\omega)$ and $V_{resp}(j\omega)$ are the Fourier transforms of $v_{ref}(t)$ and $v_{resp}(t)$, respectively. Figures (4.12) and (4.13) illustrate the phase and magnitude of $S_{11}(j\omega)$, respectively, that was computed using the waveforms $v_{ref}(t)$ and $v_{resp}(t)$ shown in Figures (4.10) and (4.11).

4.5.2 FREQUENCY DOMAIN TECHNIQUE

Frequency Domain technique is used in this work as an alternative to the Time Domain measurements. In TDR, computation is needed to obtain the reflection coefficient, $S_{11}(j\omega)$, while this technique measures the reflection coefficient, $S_{11}(j\omega)$, from the cavity under test. An hp 8410 network analyzer is used to perform the measurements. Some calibration steps are performed before making the reflection coefficient measurements. The cavity under test is attached to the S_{11} port of the network analyzer and a sweep measurement is performed for the frequency band of interest.

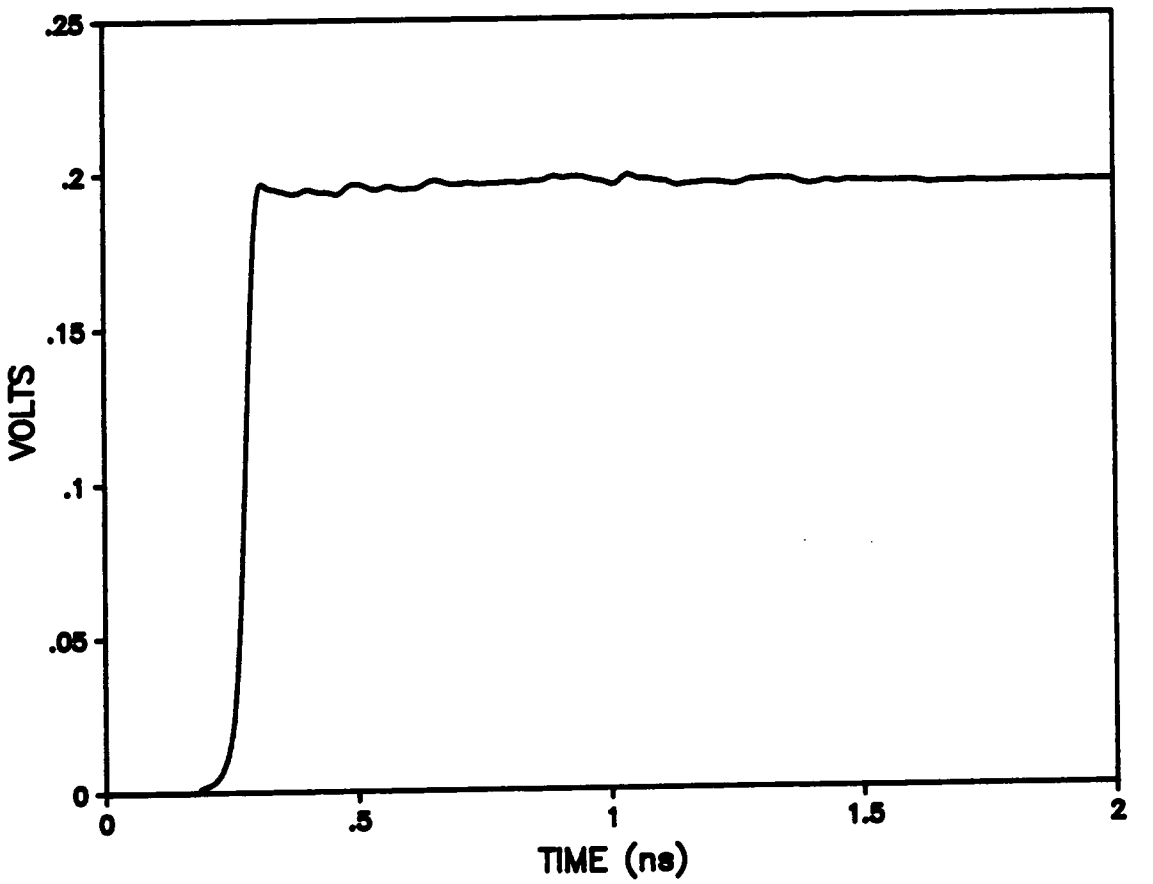

Figure (4.10). A typical reference waveform.

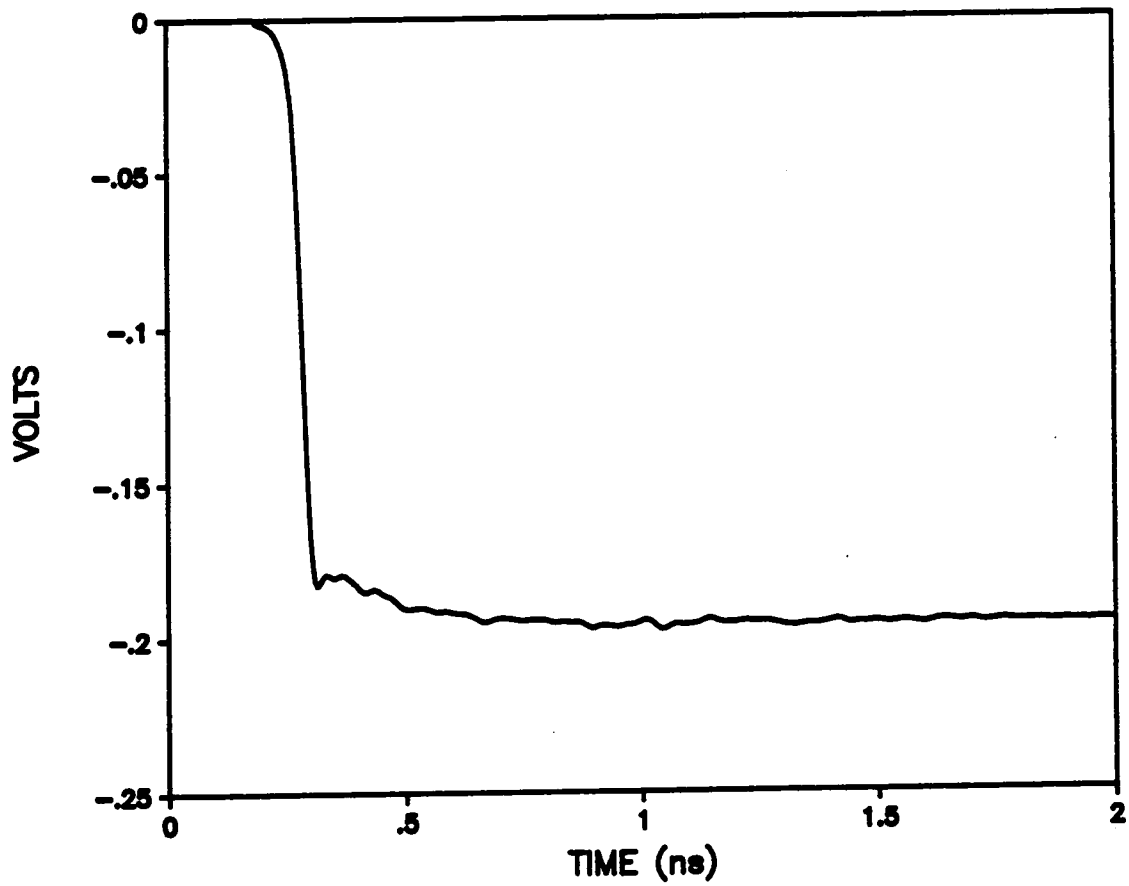

Figure (4.11). Response waveform from one of the cavities.

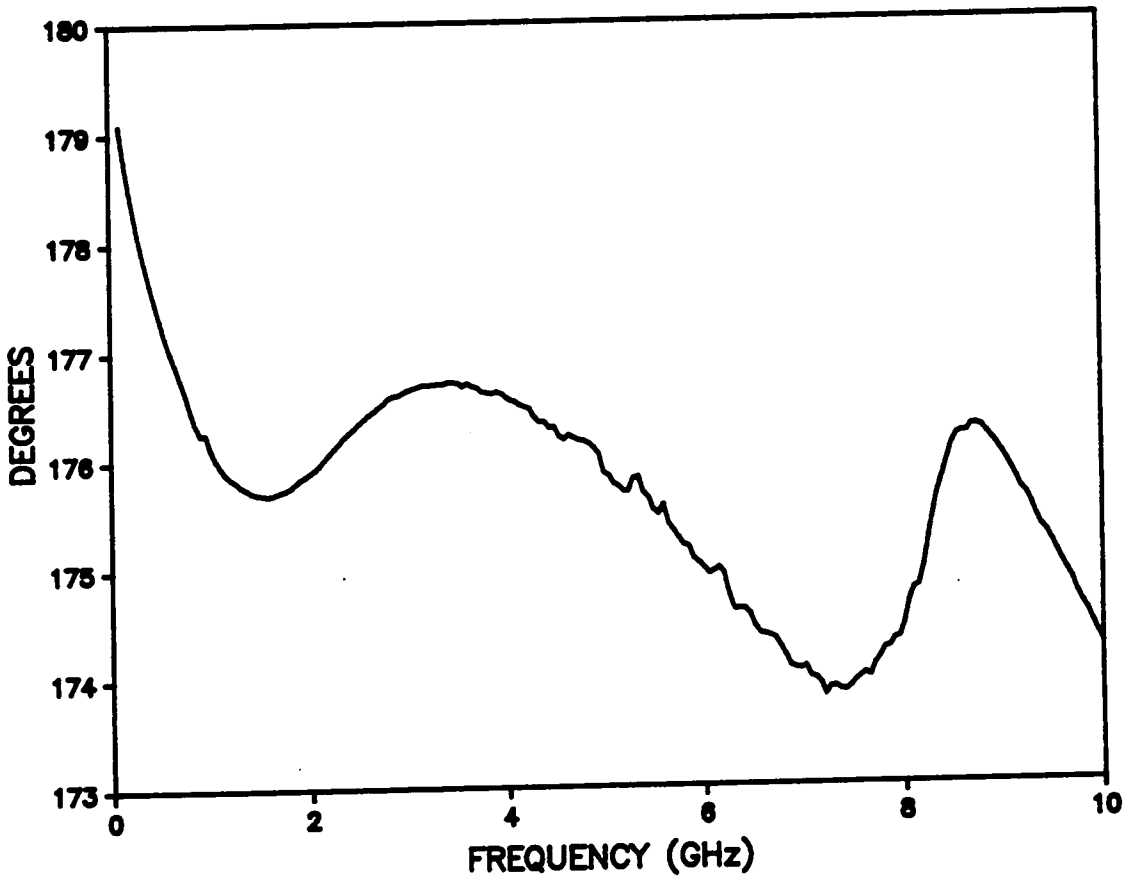

Figure (4.12). Phase of $S_{11}(j\omega)$.

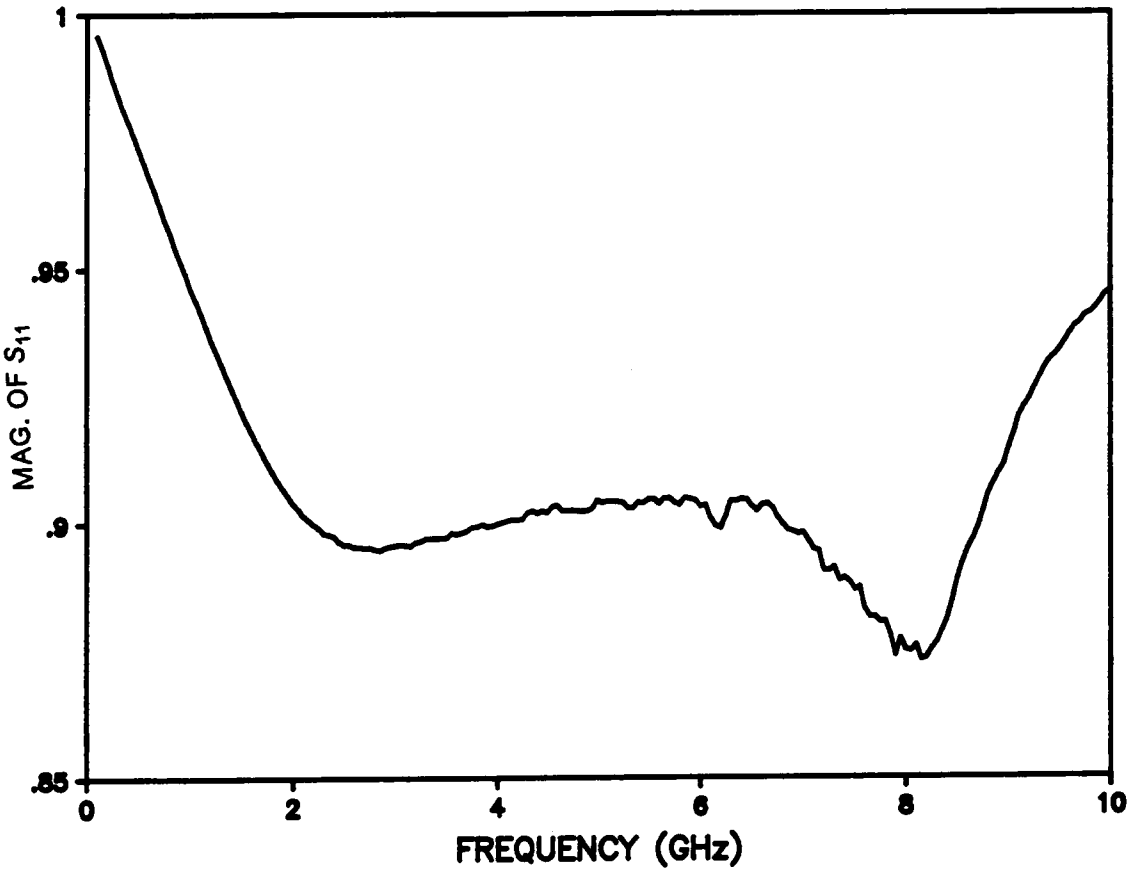

Figure (4.13). Magnitude of $S_{11}(j\omega)$.

4.6 EXPERIMENTAL RESULTS

This section consists of two subsections, the first one presents the characterization results of two ferrite materials. The second subsection concerns with the verification of the technique used to characterize the ferrite materials as well as the computer program used to obtain the characterization results.

4.6.1 CHARACTERIZATION RESULTS

Characterization results for two thick film ferrite materials are presented in this section. These results consist of some graphs illustrating the relative complex permeability, $\mu_r^*(j\omega)$, versus frequency. Separate graphs for the real part of permeability, μ'_r, and the magnetic loss, μ''_r, are shown for the two ferrites. TDR and Frequency Domain measurements are presented in every case. Figures (4.14) and (4.15) illustrate μ'_r and μ''_r, respectively, for the ESL EX-2000 thick film ferrite paste. These results agree with the manufacturer's approximate specifications of the ferrite. Figures (4.16) and (4.17), which show results of two different samples of the same material (ESL EX-2000), illustrate the repeatability of the characterization results. Figures (4.18) and (4.19) illustrate the corresponding results for the Remex 4920 thick film ferrite paste.

4.6.2 VERIFICATION

Two verification methods for the characterization results were performed. These methods are based upon the resonance and the impedance. The first verifi-

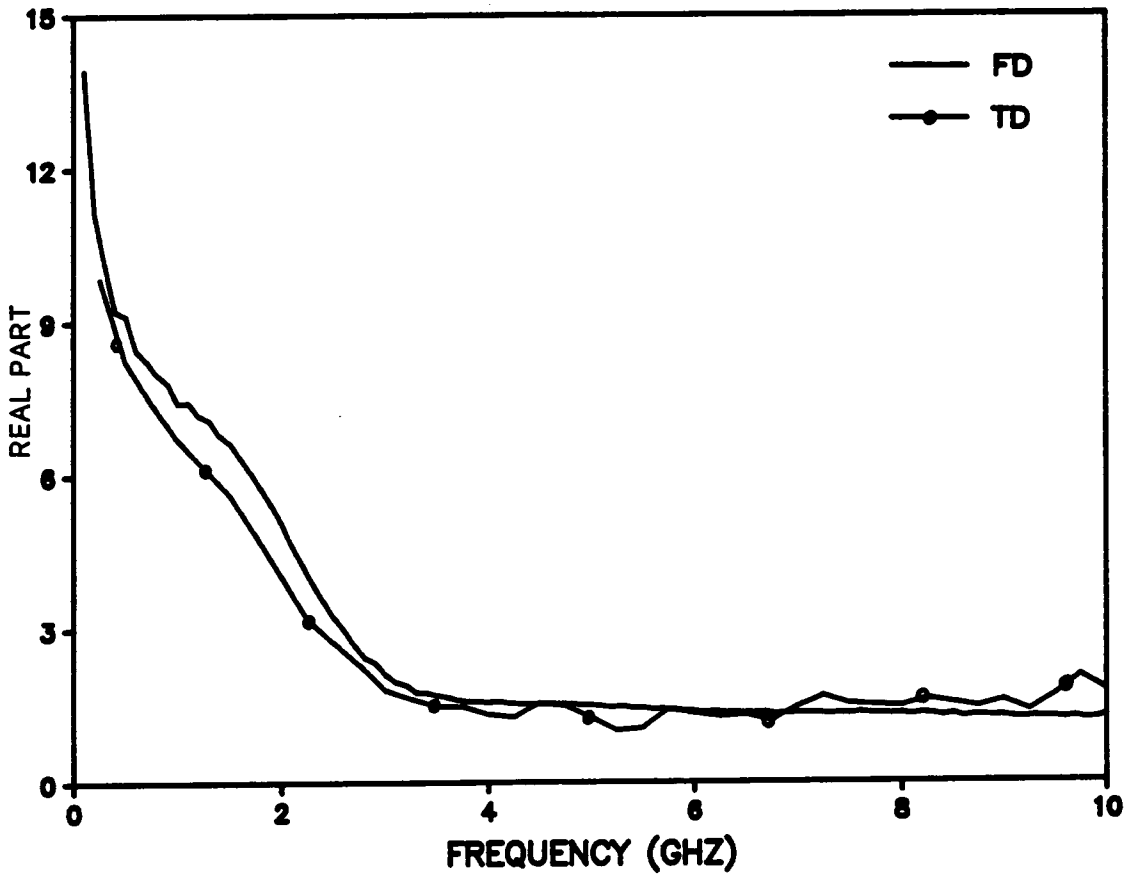

Figure (4.14). Real part of relative permeability, μ'_r, of the ESL EX-2000 thick film ferrite paste.

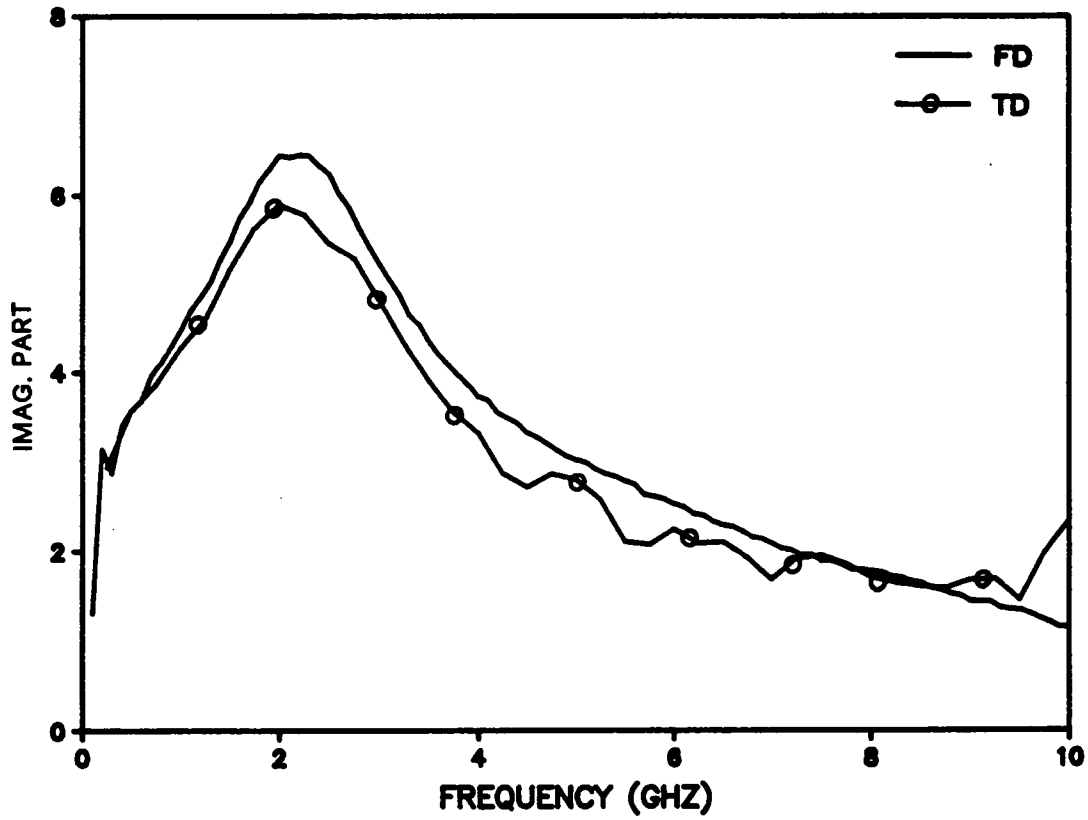

Figure (4.15). Relative magnetic loss, μ''_r, of the ESL EX-2000 thick film ferrite paste.

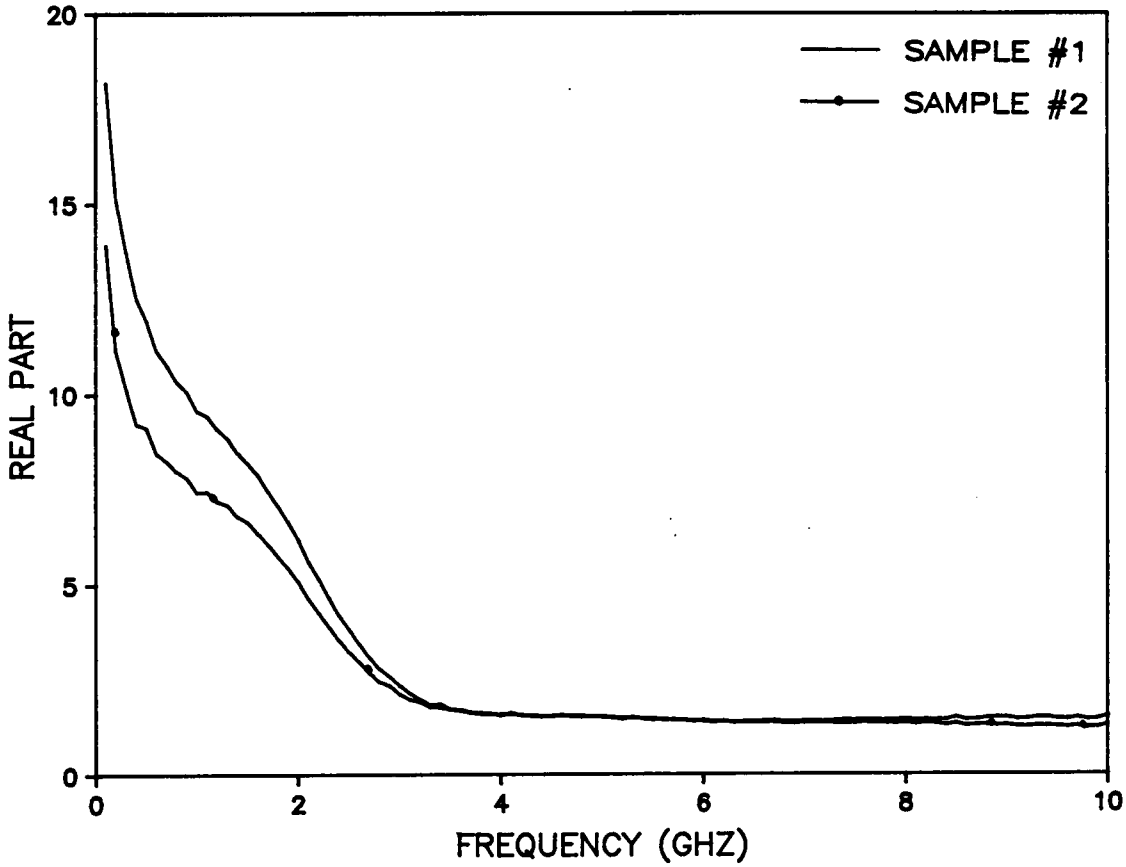

Figure (4.16). Real part of relative permeability, μ'_r, of two different samples where ESL EX-2000 ferrite paste was used.

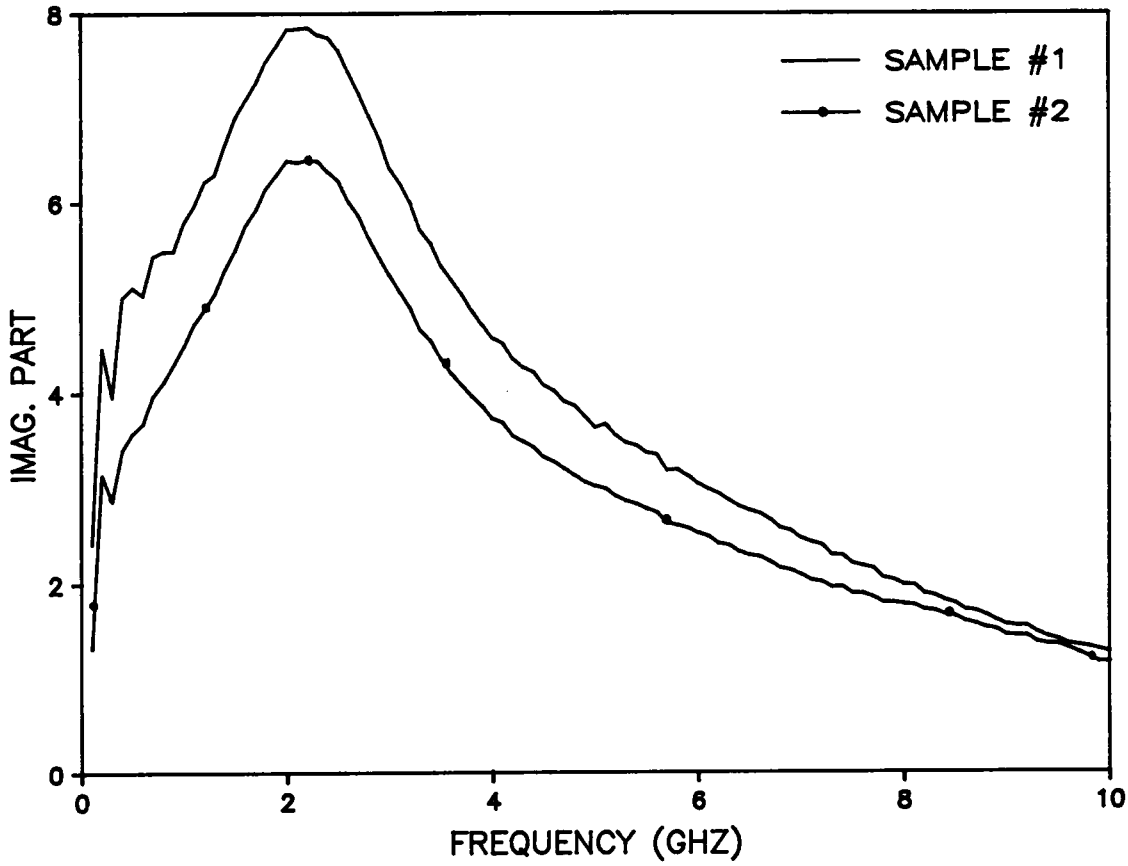

Figure (4.17). Relative magnetic loss, μ''_r, of two different samples where ESL EX-2000 ferrite paste was used.

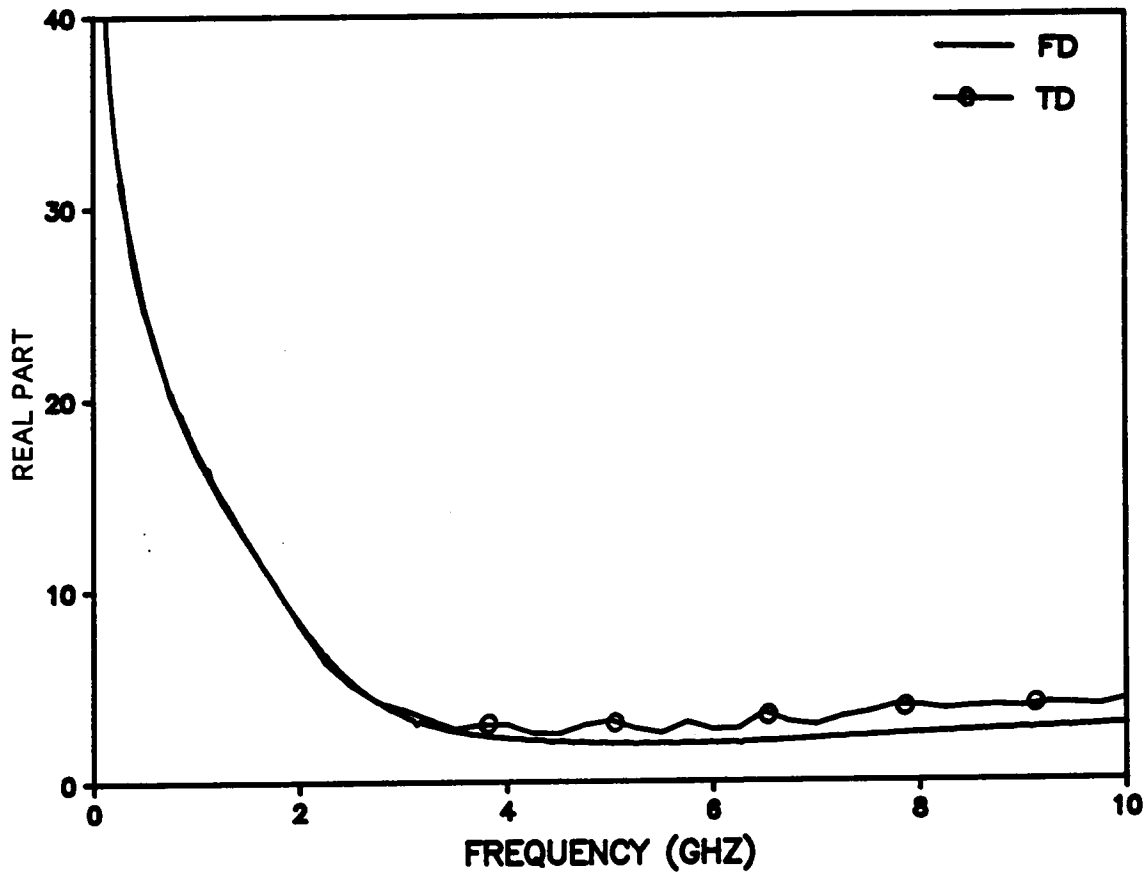

Figure (4.18). Real part of relative permeability, μ'_r, of the Remex 4920 thick film ferrite paste.

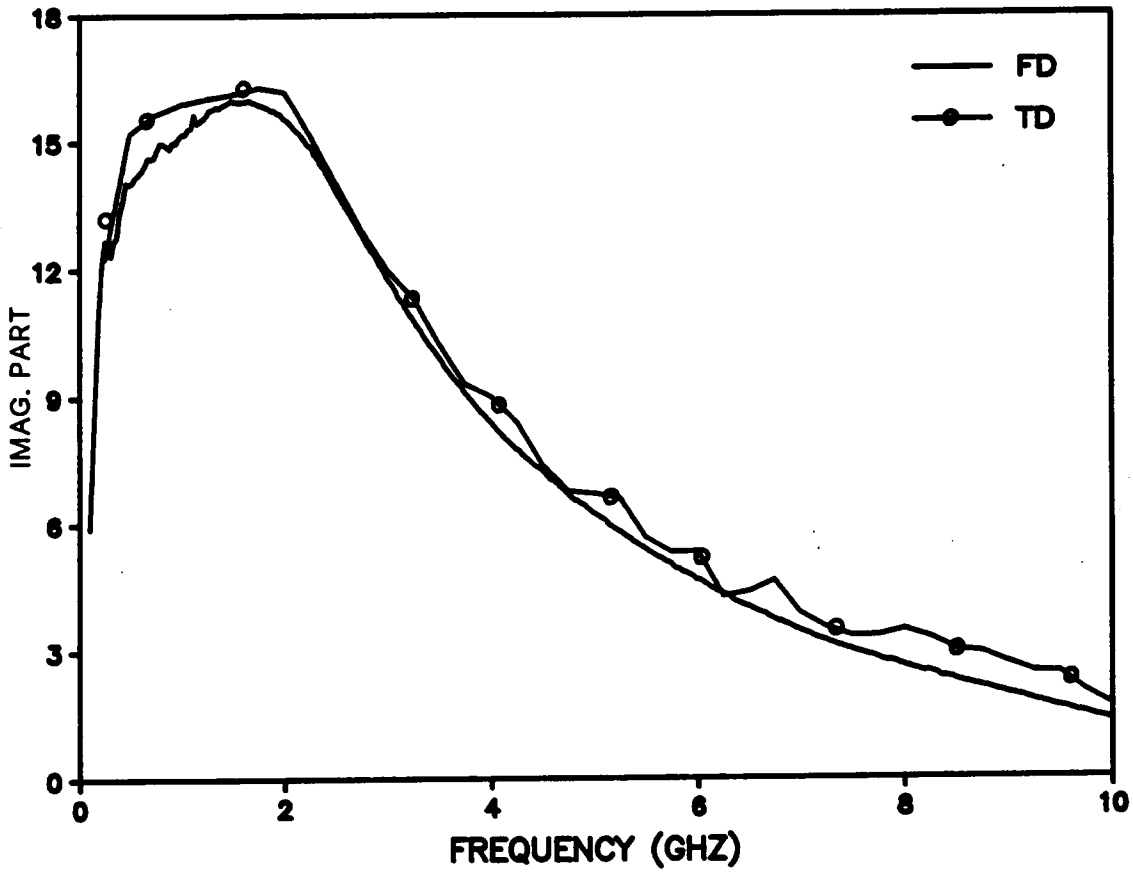

Figure (4.19). Relative magnetic loss, μ''_r, of the Remex 4920 thick film ferrite paste.

cation experiment was achieved by matching the resonances of a simulated reflection coefficient with the resonances of the measured reflection coefficient, S_{11}, from the cavity. The simulated reflection coefficient was computed using the same verification program used in section 4.3. Two dimensions sets of cavities are constructed, one set was constructed with an outer radius of 1 cm and the other set of 2 cm. The ESL EX-2000 ferrite paste was utilized for both sets. For the 1 cm outer radius cavities, the measured reflection coefficient has a resonance at about 15 GHz. By extrapolating the curve shown in Figure (4.14), one can assume the measured value of μ', at 15 GHz to be about 1.43. A value of μ', of 1.37 produces the simulated resonance at 15 GHz. Figure (4.20) illustrates both the simulated and the experimental magnitude of $S_{11}$with resonance at 15 GHz. For the 2 cm outer radius cavities, the resonances of the measured reflection coefficient are occurring at lower frequencies as expected. The resonances occur at about 5 and 11 GHz, respectively. The measured value of μ', at both frequencies is about 1.48 as one can observe from Figure (4.14). The simulated reflection coefficient with resonances at 5 and 11 GHz was obtained with a μ', of 1.57 which is close to the measured value. Figure (4.21) illustrates the experimental and the simulated magnitude of S_{11} with resonances at 5 and 11 GHz,respectively.

The second verification experiment was achieved by matching two calculated impedances. The first impedance is computed using the equation,

$$Z_{in} = Z_0 \frac{1 + S_{11}(j\omega)}{1 - S_{11}(j\omega)} \tag{4.105}$$

where Z_0 is the characteristic impedance of the transmission line to which the cavity is adapted and $S_{11}(j\omega)$ is the measured reflection coefficient. To compute the second

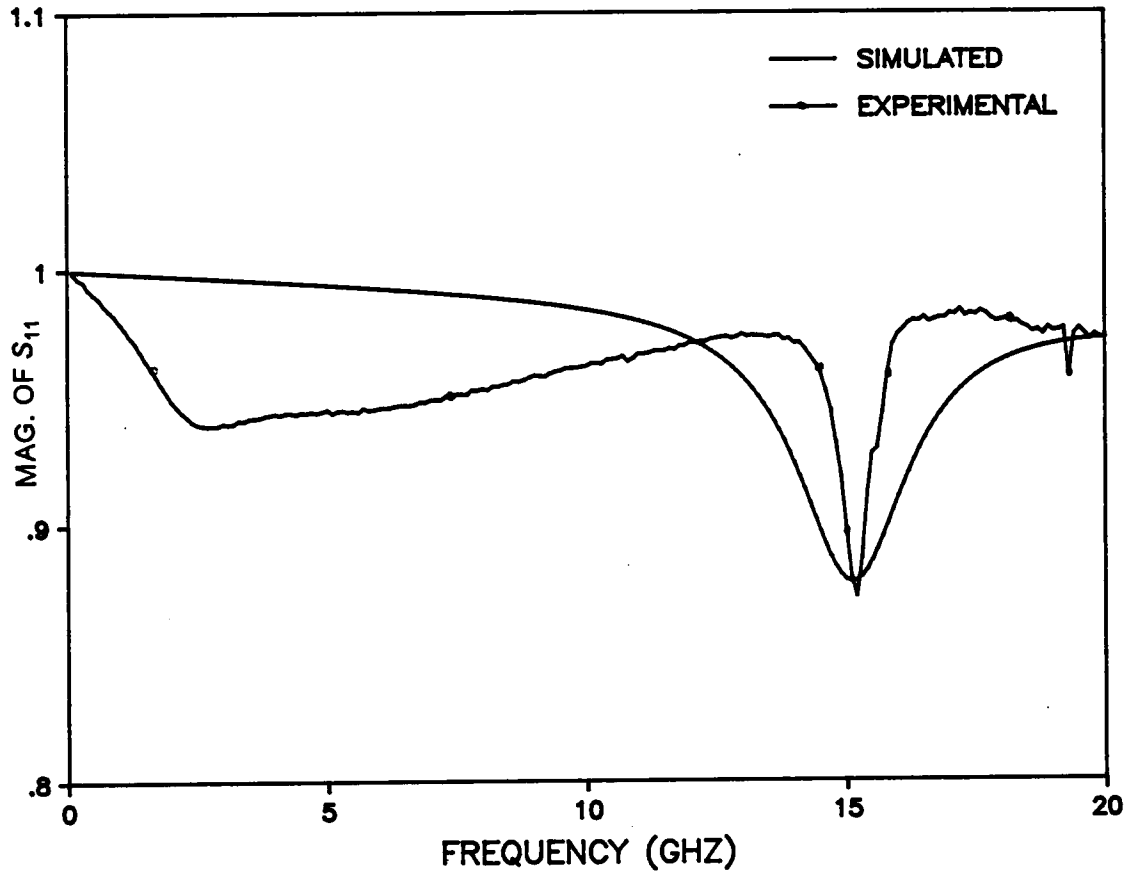

Figure (4.20). Simulated and experimental magnitude of S_{11} of the 1 cm cavities.

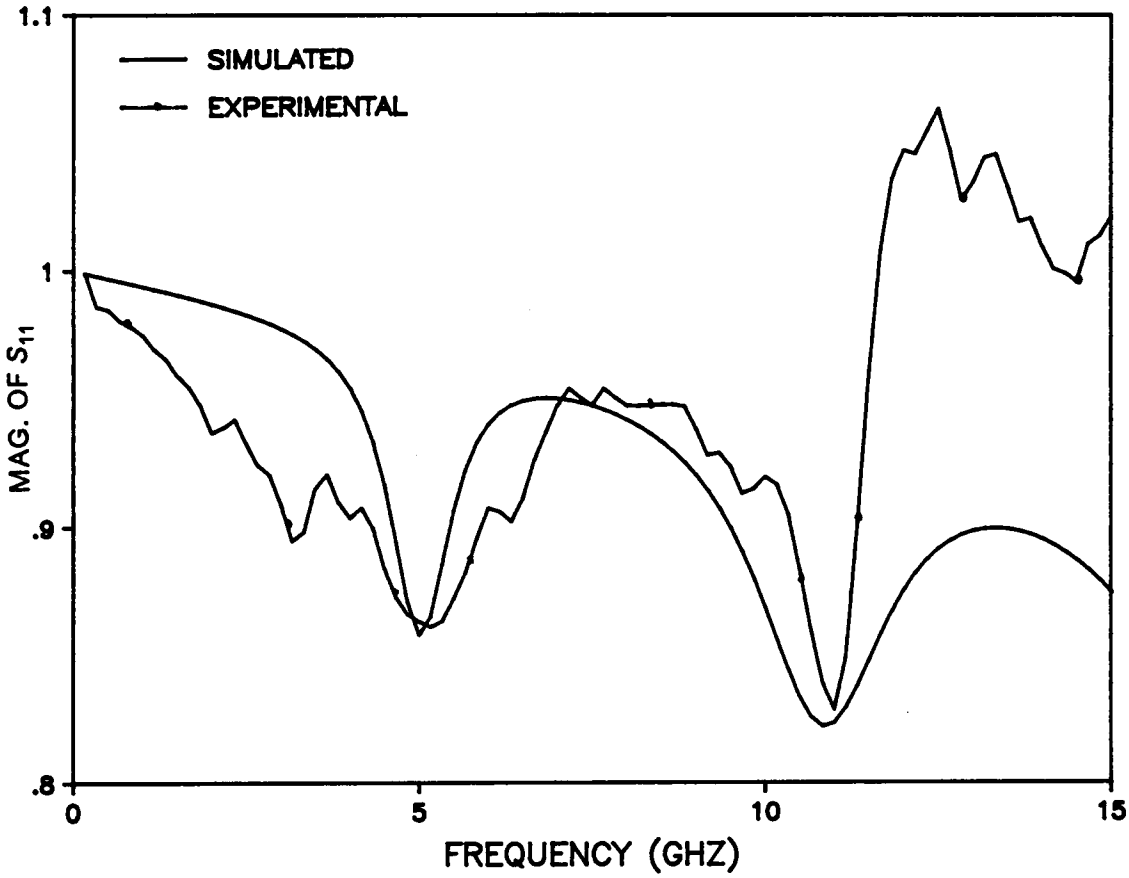

Figure (4.21). Simulated and experimental magnitude of S_{11} of the 2 cm cavities.

impedance, the cavity is modeled by a coaxial transmission line terminated by a short circuit. The characteristic impedance of the line modeling the cavity is given by,

$$Z'_0 = \frac{\ln(R/b)}{2\pi}\sqrt{\frac{\overset{*}{\mu_r}\mu_0}{\overset{*}{\varepsilon_r}\varepsilon_0}} \tag{4.106}$$

where R and b are the outer and inner radii of the cavity, respectively, μ_0 and ε_0 are the permeability and permittivity of air, respectively, and μ_r^* is the measured relative permeability of the ferrite utilized in this experiment (Remex 4920). The second impedance is given by,

$$Z'_{in} = jZ'_0 \tan\left(\frac{\omega}{c}\sqrt{\overset{*}{\mu_r}\overset{*}{\varepsilon_r}}\right)d \tag{4.107}$$

where c and d are the speed of light and the thickness of the ferrite, respectively. The two impedances are computed and their real and imaginary parts are both plotted. Figures (4.22) and (4.23) illustrate the two impedances. A close match occurs as observed from these figures. The sensitivity of Z'_{in} due to a change in μ_r^* is also verified. The value of μ'_r is increased by 10% and Z'_{in} is computed. Figure (4.24) shows the change in the imaginary part of Z'_{in} due to the change in μ'_r. Figures (4.25) and (4.26) illustrate the measured μ'_r and μ''_r in addition to the ones producing an exact match between Z_{in} and Z'_{in}.

4.7 CONCLUSION

A simple configuration was proposed in this chapter for the characterization of ferrite pastes. The proposed configuration consisted of a cavity like sample holder attached to the end of a transmission line. In this new configuration, there was no

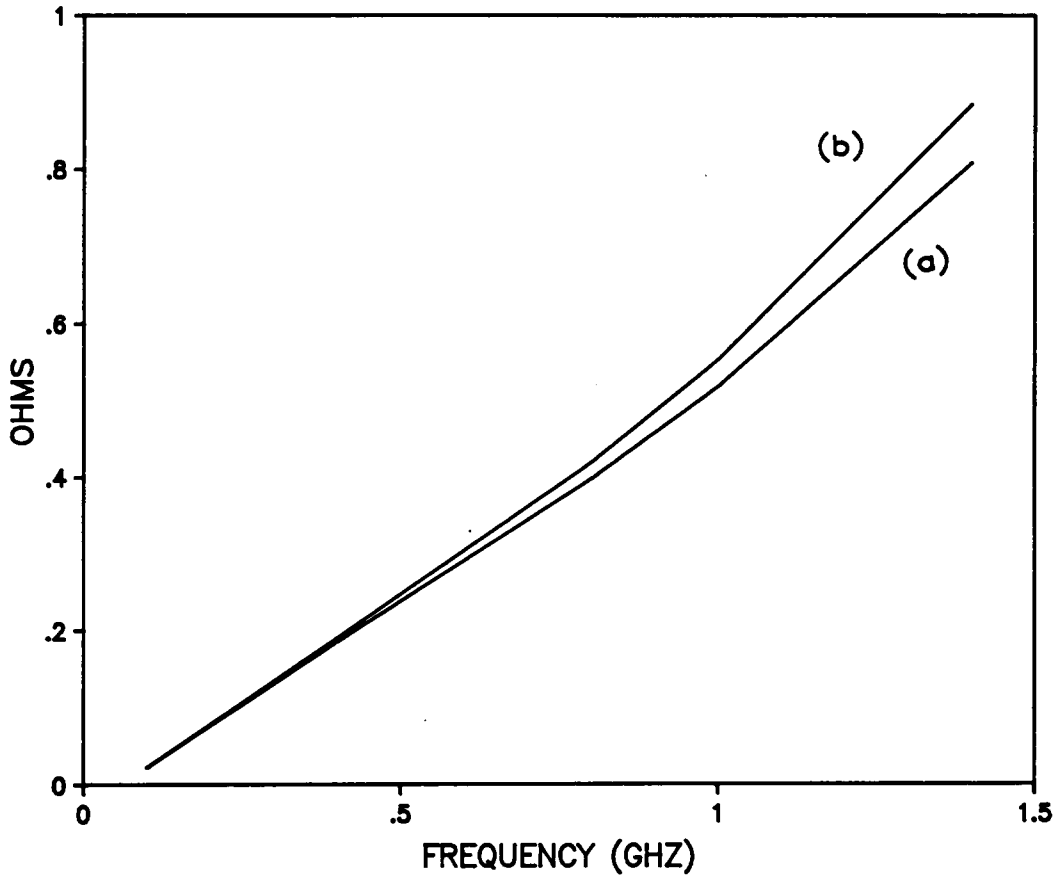

Figure (4.22). Real part of impedances from (a) measured S_{11} and (b) measured μ_r^*.

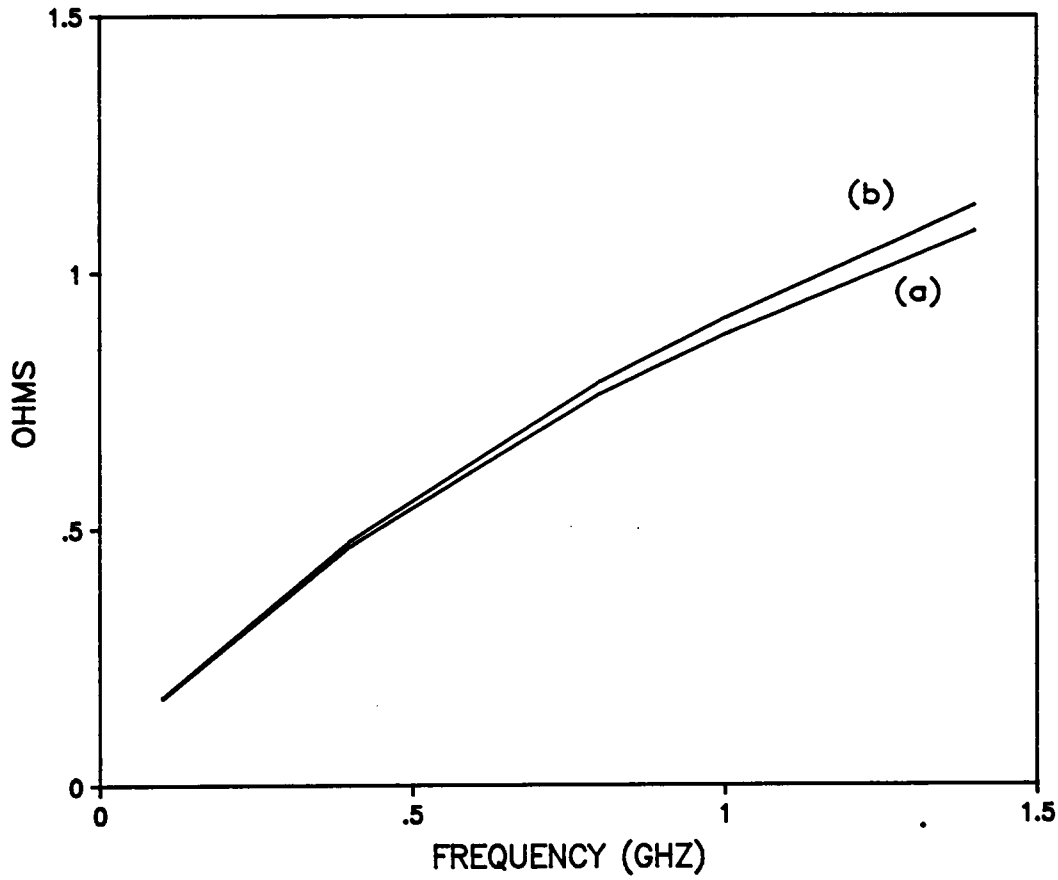

Figure (4.23). Imaginary part of impedances from (a) measured S_{11} and (b) measured $\hat{\mu}_r$.

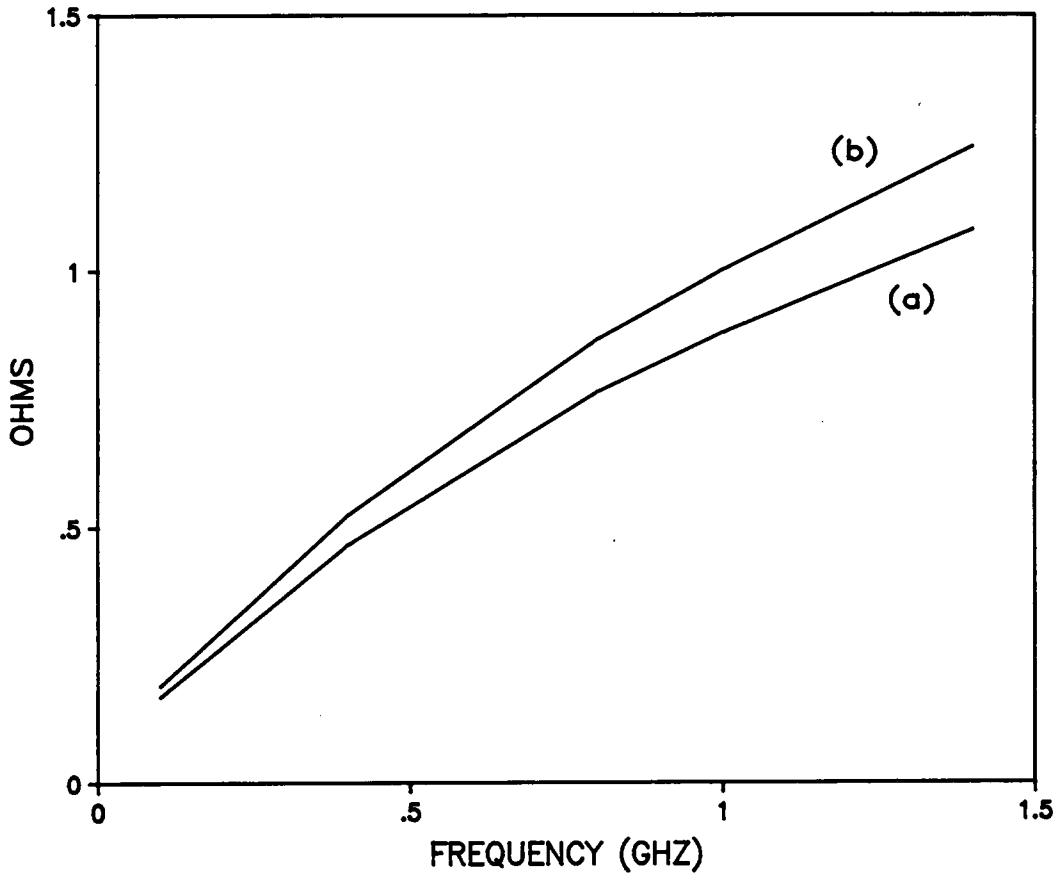

Figure (4.24). Sensitivity of the second computed impedance to change in μ'_r, (a) measured μ'_r and (b) 1.1 measured μ'_r.

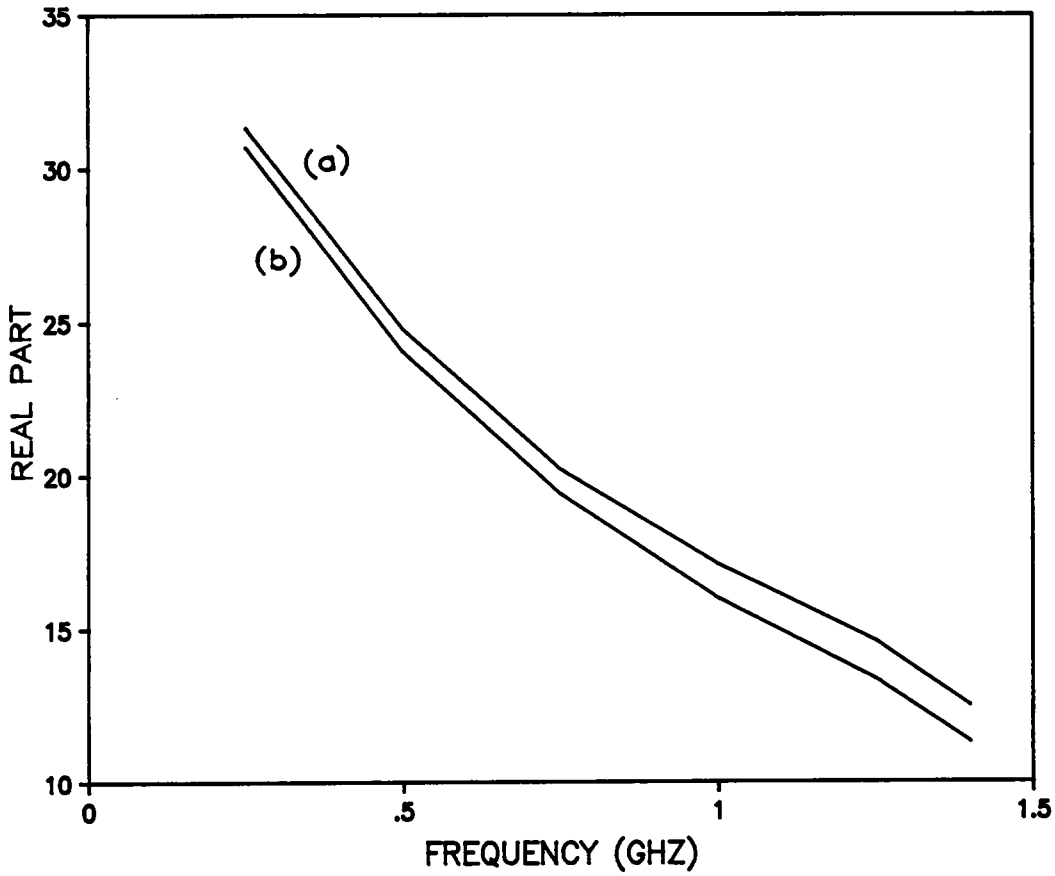

Figure (4.25). Real part of relative permeability μ'_r, (a) measured μ', and (b) verified μ'_r.

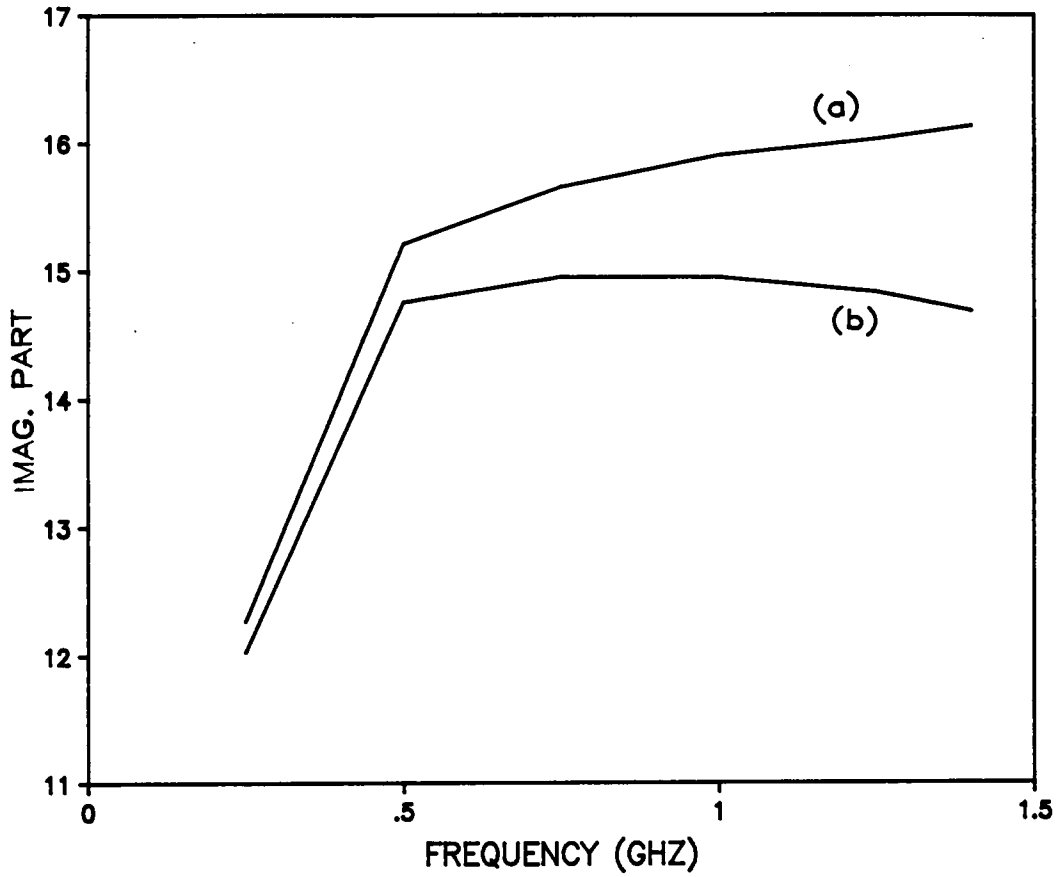

Figure (4.26). Relative magnetic loss μ''_r, (a) measured μ''_r and (b) verified μ''_r.

need to cut or shape the sample precisely to fit in an existing structure, rather, the cavity walls were deposited on a coaxially shaped sample. As it was explained in section 4.4, the top metalization was printed on top of the ferrite sample eliminating any chance of air gaps creation. This new structure was well suited for thick film materials where the ferrite layers as well as the cavity walls were printed on a ceramic substrate.

Full field analysis of this new configuration was explained thoroughly. Results of the analysis were written in the form of a computer program utilized in some simulation experiments presented in this chapter. The experiments mentioned above were used to reach some conclusions such as, the value of ε'_r used in obtaining μ^*_r from $S_{11}(j\omega)$ measurements had little effect on the accuracy of μ^*_r values. It was also concluded that varying the magnetic loss effects the magnitude of the reflection coefficient more than it does to the phase. Another conclusion was that the larger the outer radius the more resonances were produced in the bandwidth of interest. It was also concluded that thicker samples can yield more accurate results due to the fact that the rate of change of the phase with respect to frequency is higher for thicker samples.

Time Domain Reflectometry (TDR) technique was used in the data acquisition. TDR waveforms were acquired and used to calculate $S_{11}(j\omega)$, the termination's reflection coefficient. The relative complex permeability, μ^*_r, was derived from the calculated reflection coefficient. Frequency Domain measurements were also used to obtain the reflection coefficient. Verification experiments were performed to check the technique and computer program used to characterize the ferrite materials.

Characterization results for two ferrite materials were also presented. These results were obtained using TDR and Frequency Domain measurements.

CHAPTER V

CONCLUSION

Wideband characterization and modeling of thick film magnetic materials and structures at high frequencies were discussed in this dissertation. A review covering the development of the techniques used to characterize and model thick film magnetic materials and structures was discussed also. Three thick film inductor structures were modeled. These three structures were the single layer coil, the multilayer coil separated with dielectric material, and multilayer coil separated by ferrite material. A simple configuration was proposed in this dissertation for the characterization of ferrite pastes. The proposed configuration consisted of a cavity like sample holder attached to the end of a transmission line.

The thick film inductor under test was printed and located at the end of a reference transmission line. A model for the single layer coil was constructed in the Frequency Domain. The impedance of the model as well as an experimentally measured one of the inductor under test were compared and brought to a close match. For the other two structures, a model for the inductor under test was constructed using TDR. The modeling was performed through an iterative approach. MTCAP was used to produce a simulated response waveform with the model as the

termination of a transmission line. The simulated and measured response waveforms were compared and a good match between them was achieved. It was obvious from the modeling results that the models were getting more complex as the inductor structure became more complex. TDR technique was used in the data acquisition and modeling of the inductor under test over the frequency range from DC to few GHz.

To check the accuracy of the modeling process, comparison between the model's driving point impedance as well as the actual one measured using a Vector Impedance Meter was performed. It was concluded that the model was accurate enough to create a good match between the two impedances. Validity of the modeling process was also discussed. The conclusion was that different valid models for a particular circuit can be reached. It was also concluded that the model is valid for any type of excitation.

In the new configuration used for the characterization of the ferrite pastes, the cavity walls were deposited on a coaxially shaped sample. As a result, there was no need to cut or shape the sample precisely to fit in an existing structure. The top metallization was printed on top of the ferrite sample eliminating any chance of air gaps creation. This new structure was well suited for thick film materials where the ferrite layers as well as the cavity walls were printed on a ceramic substrate.

Full field analysis of this new configuration was used to find a relationship between the complex permeability of the ferrite and the reflection coefficient. Method of moments was used to achieve this task. Computer simulation of the cavity was performed to reach some conclusions such as, the value of ε', used in obtaining μ_r^*

from $S_{11}(j\omega)$ measurements had little effect on the accuracy of μ_r^* values. The magnitude of the reflection coefficient was more affected than the phase by changing the magnetic loss. Another conclusion was that the larger the outer radius the more resonances were produced in the bandwidth of interest. The rate of change of the phase with respect to frequency was found to be higher for thicker samples. This result led to the conclusion that thicker samples can yield more accurate results.

TDR waveforms were acquired and used to calculate $S_{11}(j\omega)$, the termination's reflection coefficient. The relative complex permeability, μ_r^*, was derived from the calculated reflection coefficient. Frequency Domain measurements were also used to obtain the reflection coefficient. The technique and computer program used to characterize the ferrite materials are verified by comparing resonances in the simulated and experimental reflection coefficients. Characterization results for two ferrite materials were also presented. These results were obtained using Time Domain and Frequency Domain measurements.

APPENDIX I

This Fortran program computes the reflection coefficient assuming that one knows the permittivity and permeability of the ferrite material used to construct the cavity which is adapted to the end of a transmission line. It implements the equations derived in chapter IV. The computer simulation demonstrated in section (4.3) was performed using this program.

```
      IMPLICIT REAL*8 (A-H,O-Z)
      COMPLEX*16 EPSCMX,EPSJ,AMUCMX,EPMUCX,EITAB1,EITAB0,YA(50,50),
     *           Y(50,50),V(50),AI(50),AMUOEP
      DIMENSION WNA(50),ALPHA(50),PN(50),BETA(50),BETB(100),
     *          AA(50,50),AB(100,50),WNB(100),QTERM(100),PNB(100)
      WRITE(6,*) 'ENTER THE OUTER RADIUS (IN CM) OF THE SAMPLE HOLDER'
      READ(6,*) R
      WRITE(6,*) 'ENTER THE MATERIAL SAMPLE THICKNESS (IN CM)'
      READ(6,*) D
      WRITE(6,*) 'ENTER THE STARTING FREQUENCY IN HZ'
      READ(6,*) SFREQ
      WRITE(6,*) 'ENTER THE FREQUENCY STEP IN HZ'
      READ(6,*) FREQST
      WRITE(6,*) 'ENTER THE FINAL FREQUENCY IN HZ'
      READ(6,*) EFREQ
      WRITE(6,*) 'ENTER THE DIELECTRIC CONSTANT'
      READ(6,*) EPSR
      WRITE(6,*) 'ENTER THE DIELECTRIC LOSS'
      READ(6,*) EPSI
      WRITE(6,*) 'ENTER THE MAGNETIC CONSTANT'
      READ(6,*) AMUR
      WRITE(6,*) 'ENTER THE MAGNETIC LOSS'
      READ(6,*) AMUI
```

```
C
C ***************************************************************************
C * THESE ARE THE DIMENSIONS OF THE LINE CONNECTED TO THE CAVITY *
C ***************************************************************************
C
      A=0.35D0
      B=0.15D0
C
C ***************************************************************************
C * THESE ARE THE NUMBER OF MODES IN THE TRANSMISSION LINE AND *
C * CAVITY REGIONS AND THE NUMBER OF EXPANSION FUNCTIONS      *
C ***************************************************************************
C
      NMDA=5
      NEXPF=NMDA
      NMDB=15
C
C ***************************************************************************
C * LET US INITIALIZE THE ENTREES OF THE AA AND AB MATRICES  *
C ***************************************************************************
C
      DO 44 I=1,NMDA
      DO 44 J=1,NEXPF
        AA(I,J)=0.0D0
 44   CONTINUE
      DO 66 I=1,NMDB
      DO 66 J=1,NEXPF
        AB(I,J)=0.0D0
 66   CONTINUE
C
C ***************************************************************************
C * LET US COMPUTE THE 1,1 ENTREES OF THE AA AND AB MATRICES *
C ***************************************************************************
C
      ALRB=DLOG(R/B)
      ALAB=DLOG(A/B)
      AA(1,1)=1.0D0
      ALAR=ALAB/ALRB
      AB(1,1)=-1.0D0*DSQRT(ALAR)
C
C ***************************************************
C * THESE ARE THE VALUES OF PI, MU0, AND EPSELON0 *
C ***************************************************
C
      PI=DARCOS(-1.0D0)
      AMU0=PI*4.0D-9
      EPSL0=1.0D0/(PI*36.0D11)
```

```
C
C ************************************************************
C * LET US COMPUTE THE WAVE NUMBERS FOR BOTH REGIONS *
C * AND THE BESSEL AND NEUMANN FUNCTIONS NEEDED TO   *
C * COMPUTE THE ENTREES OF THE AA AND AB MATRICES    *
C ************************************************************
C
      DO 2 I=2,NMDA
        I1=I-1
        CALL ZEROS(I1,A,B,ZARO)
        BWNA=ZARO
        WNA(I)=BWNA/B
        AWNA=WNA(I)*A
        CALL BESSEL(0,BWNA,AJ0B)
        CALL BESSEL(1,AWNA,AJ1A)
        CALL ANEUM(0,BWNA,AN0B)
        CALL ANEUM(1,AWNA,AN1A)
        ALPHA(I)=A*(AJ0B*AN1A-AN0B*AJ1A)
        ALPSQ=ALPHA(I)*ALPHA(I)
        CALL BESSEL(1,BWNA,AJ1B)
        CALL ANEUM(1,BWNA,AN1B)
        BETA(I)=B*(AJ0B*AN1B-AN0B*AJ1B)
        BETASQ=BETA(I)*BETA(I)
        PIA=PI*(ALPSQ-BETASQ)
        PN(I)=1.0D0/(DSQRT(PIA))
        AA(I,I)=1.0D0
    2 CONTINUE
C
C
      DO 5 K=2,NMDB
        K1=K-1
        CALL ZEROS(K1,R,B,ROOT)
        BWNB=ROOT
        WNB(K)=BWNB/B
        AWNB=A*WNB(K)
        RWNB=R*WNB(K)
        CALL BESSEL(0,BWNB,BJ0B)
        CALL BESSEL(0,AWNB,BJ0A)
        CALL ANEUM(0,AWNB,BN0A)
        CALL ANEUM(0,BWNB,BN0B)
        CALL ANEUM(1,BWNB,BN1B)
        CALL ANEUM(1,RWNB,BN1R)
        CALL BESSEL(1,BWNB,BJ1B)
        CALL BESSEL(1,RWNB,BJ1R)
        ALPHB=R*(BJ0B*BN1R-BN0B*BJ1R)
        BETB(K)=B*(BJ0B*BN1B-BN0B*BJ1B)
        BAL=PI*(ALPHB*ALPHB-BETB(K)*BETB(K))
        PNB(K)=1.0D0/(DSQRT(BAL))
        QTERM(K)=BJ0B*BN0A-BN0B*BJ0A
        TPI=2.0D0*PI/ALAB
```

```
        AB(K,1)=DSQRT(TPI)*PNB(K)*QTERM(K)/WNB(K)
  5   CONTINUE
C
C
      DO 6 N=2,NMDB
        WNBB=WNB(N)
        QTERMM=QTERM(N)
        PNBB=PNB(N)
        BETBB=BETB(N)
        DO 7 J=2,NEXPF
          WNAA=WNA(J)
          WND=WNAA-WNBB
          ABSWND=DABS(WND)
          IF(ABSWND.LT.1.0D-06) GO TO 8
          AB(N,J)=-2.0D0*PI*PN(J)*PNBB*WNBB*ALPHA(J)*QTERMM/
     *     (WNAA**2-WNBB**2)
          GO TO 7
  8       AB(N,J)=PI*PN(J)*PNBB*(BETBB*BETA(J)-ALPHA(J)*ALPHA(J))
  7     CONTINUE
  6   CONTINUE
C
C
      EPSCMX=DCMPLX(EPSR,-EPSI)*EPSL0
      EPSJ=DCMPLX(EPSI,EPSR)*EPSL0
      AMUCMX=DCMPLX(AMUR,-AMUI)*AMU0
      EPMUCX=EPSCMX*AMUCMX
      AMUOEP=AMUCMX/EPSCMX
      EITAB1=CDSQRT(AMUOEP)
      REALE=DREAL(EITAB1)
      AIEIT=DIMAG(EITAB1)
      EITAB0=DCMPLX(AIEIT,-REALE)
      AMUOES=AMU0/EPSL0
      EITA0=DSQRT(AMUOES)
      E0M0=AMU0*EPSL0
      DO 9 M=1,NEXPF
        AI(M)=0.0D0
  9   CONTINUE
      AI(1)=2.0D0/EITA0
C
C ***************************************************************
C * NOW WE START CHANGING THE FREQUENCY AND CALCULATING THE      *
C * THE REFLECTION COEFFICIENT S11.                             *
C ***************************************************************
C
      NP=1.0001+(EFREQ-SFREQ)/FREQST
      DO 11 NW=1,NP
        FREQ=SFREQ+(NW-1)*FREQST
        RFREQ=FREQ*1.0D-09
        W=2.0D0*PI*FREQ
        CALL CALCYA(AA,NMDA,NEXPF,EITA0,W,E0M0,WNA,EPSL0,YA)
```

```
        CALL CALCYB(YA,AB,NMDB,D,NEXPF,EITABO,EPSJ,EPMUCX,W,WNB,Y)
        CALL GAUSS(NEXPF,Y,AI,V)
        RHOR=DREAL(V(1))-1.0D0
        RHOI=DIMAG(V(1))
        RHOMAG=DSQRT(RHOR**2+RHOI**2)
        RH=DATAN2(RHOI,RHOR)
        RHOPHS=180.0D0*RH/PI
        WRITE(3,10) RFREQ,RHOMAG,RHOPHS
 10     FORMAT(3(2X,F15.8))
 11   CONTINUE
      STOP
      END
C
C ***************************************************************
C * THIS SUBROUTINE, CALCYA, CALCULATES THE ENTREES OF THE *
C * YA MATRIX WHICH REPRESENTS THE TRANSMISSION LINE REGION*
C ***************************************************************
C
      SUBROUTINE CALCYA(AA,NMDA,NEXPF,EITAO,W,EOMO,WNA,EPSLO,YA)
      IMPLICIT REAL*8 (A-H,O-Z)
      COMPLEX*16 YA(50,50),SUM,AKZN,AKZNSQ,EITAN(50)
      DIMENSION WNA(50),AA(50,50)
      DO 101 I=2,NMDA
        AKZCMX=W*W*EOMO-WNA(I)*WNA(I)
        AKZNSQ=DCMPLX(AKZCMX,0.0D0)
        AKZN=CDSQRT(AKZNSQ)
        EITAN(I)=AKZN/(W*EPSLO)
101   CONTINUE
      DO 102 I=1,NEXPF
        DO 103 J=1,NEXPF
          SUM=0.0D0
          DO 104 N=2,NMDA
            SUM=SUM+AA(N,I)*AA(N,J)/EITAN(N)
104       CONTINUE
          YA(I,J)=AA(1,I)*AA(1,J)/EITAO+SUM
103     CONTINUE
102   CONTINUE
      RETURN
      END
C
C ***********************************************************
C * THIS SUBROUTINE, CALCYB, CALCULATES THE ENTREES OF*
C * THE YB MATRIX WHICH REPRESENTS THE CAVITY REGION. *
C * IT ALSO CALCULATES THE TOTAL Y MATRIX.          *
C ***********************************************************
C
      SUBROUTINE CALCYB(YA,AB,NMDB,D,NEXPF,EITABO,EPSJ,EPMUCX,W,WNB,Y)
      IMPLICIT REAL*8 (A-H,O-Z)
      DIMENSION WNB(100),AB(100,50)
      COMPLEX*16 YB(50,50),SUM,AKZNB,EITANB,EITTAN(100),TANKNB,TANKOB
```

```
     *,AK0,EPMUCX,EPSJ,AK02,EITAB0,YA(50,50),Y(50,50),AK0D,AKZNBD,AKSQ
      AK02=W*W*EPMUCX
      AK0=CDSQRT(AK02)
      AK0D=AK0*D
      TANK0B=CDSIN(AK0D)/CDCOS(AK0D)
C
      DO 201 I=2,NMDB
        AKSQ=AK02-WNB(I)*WNB(I)
        AKZNB=CDSQRT(AKSQ)
        EITANB=AKZNB/(W*EPSJ)
        AKZNBD=AKZNB*D
        TANKNB=CDSIN(AKZNBD)/CDCOS(AKZNBD)
        EITTAN(I)=EITANB*TANKNB
201   CONTINUE
C
      DO 202 I=1,NEXPF
        DO 203 J=1,NEXPF
          SUM=0.0D0
          DO 204 N=2,NMDB
            SUM=SUM+AB(N,I)*AB(N,J)/EITTAN(N)
204       CONTINUE
          YB(I,J)=-(AB(1,I)*AB(1,J)/(EITAB0*TANK0B))-SUM
203     CONTINUE
202   CONTINUE
      DO 205 J=1,NEXPF
        DO 205 L=1,NEXPF
          Y(J,L)=YA(J,L)+YB(J,L)
205   CONTINUE
      RETURN
      END
```

APPENDIX II

This Fortran program computes the relative complex permeability of a ferrite material used to construct a cavity which is adapted to the end a transmission line. This program implements the equations derived in chapter IV. The experimental results demonstrated in section (4.6) was performed using this program.

```
      IMPLICIT REAL*8 (A-H,O-Z)
      COMPLEX*16 EPSCMX,EPSJ,AMUCMX,EPMUCX,EITAB1,EITAB0,YA(50,50),
     *           Y(50,50),V(50),AI(50),AMUOEP
      COMPLEX*16 EPSCMX,EPSJ,AMUCMX,EPMUCX,EITAB1,EITAB0,YA(50,50),
     *           Y(50,50),V(50),AI(50),AMUOEP
      DIMENSION WNA(50),ALPHA(50),PN(50),BETA(50),BETB(100),
     *          AA(50,50),AB(100,50),WNB(100),QTERM(100),PNB(100)
      WRITE(6,*) 'ENTER THE OUTER RADIUS (IN CM) OF THE SAMPLE HOLDER'
      READ(6,*) R
      WRITE(6,*) 'ENTER THE MATERIAL SAMPLE THICKNESS (IN CM)'
      READ(6,*) D
      WRITE(6,*) 'ENTER THE NUMBER OF DATA POINTS'
      READ(6,*) NP
      WRITE(6,*) 'ENTER THE DIELECTRIC CONSTANT'
      READ(6,*) FEPSR
      WRITE(6,*) 'ENTER THE DIELECTRIC LOSS'
      READ(6,*) FEPSI
      WRITE(6,*) 'ENTER AN ESTIMATE OF THE MAGNETIC CONSTANT'
      READ(6,*) EMUR
      WRITE(6,*) 'ENTER AN ESTIMATE OF THE MAGNETIC LOSS'
      READ(6,*) EMUI
C
C ***************************************************************
C * THESE ARE THE DIMENSIONS OF THE LINE CONNECTED TO THE CAVITY *
C ***************************************************************
C
      A=0.35D0
      B=0.15D0
```

```
C
C ***************************************************************
C * THESE ARE THE NUMBER OF MODES IN THE TRANSMISSION LINE AND *
C * CAVITY REGIONS AND THE NUMBER OF EXPANSION FUNCTIONS       *
C ***************************************************************
C
      NMDA=5
      NEXPF=NMDA
      NMDB=15
C
C ***************************************************************
C * LET US INITIALIZE THE ENTREES OF THE AA AND AB MATRICES *
C ***************************************************************
C
      DO 44 I=1,NMDA
      DO 44 J=1,NEXPF
        AA(I,J)=0.0D0
 44   CONTINUE
      DO 66 I=1,NMDB
      DO 66 J=1,NEXPF
        AB(I,J)=0.0D0
 66   CONTINUE
C
C ***************************************************************
C * LET US COMPUTE THE 1,1 ENTREES OF THE AA AND AB MATRICES *
C ***************************************************************
C
      ALRB=DLOG(R/B)
      ALAB=DLOG(A/B)
      AA(1,1)=1.0D0
      ALAR=ALAB/ALRB
      AB(1,1)=-1.0D0*DSQRT(ALAR)
C
C ********************************************************
C * THESE ARE THE VALUES OF PI, MU0, AND EPSELON0 *
C ********************************************************
C
      PI=DARCOS(-1.0D0)
      AMU0=PI*4.0D-9
      EPSL0=1.0D0/(PI*36.0D11)
C
C ********************************************************
C * LET US COMPUTE THE WAVE NUMBERS FOR BOTH REGIONS *
C * AND THE BESSEL AND NEUMANN FUNCTIONS NEEDED TO   *
C * COMPUTE THE ENTREES OF THE AA AND AB MATRICES    *
C ********************************************************
C
      DO 2 I=2,NMDA
        I1=I-1
        CALL ZEROS(I1,A,B,ZARO)
```

```
        BWNA=ZARO
        WNA(I)=BWNA/B
        AWNA=WNA(I)*A
        CALL BESSEL(0,BWNA,AJ0B)
        CALL BESSEL(1,AWNA,AJ1A)
        CALL ANEUM(0,BWNA,AN0B)
        CALL ANEUM(1,AWNA,AN1A)
        ALPHA(I)=A*(AJ0B*AN1A-AN0B*AJ1A)
        ALPSQ=ALPHA(I)*ALPHA(I)
        CALL BESSEL(1,BWNA,AJ1B)
        CALL ANEUM(1,BWNA,AN1B)
        BETA(I)=B*(AJ0B*AN1B-AN0B*AJ1B)
        BETASQ=BETA(I)*BETA(I)
        PIA=PI*(ALPSQ-BETASQ)
        PN(I)=1.0D0/(DSQRT(PIA))
        AA(I,I)=1.0D0
  2   CONTINUE
C
C
      DO 5 K=2,NMDB
        K1=K-1
        CALL ZEROS(K1,R,B,ROOT)
        BWNB=ROOT
        WNB(K)=BWNB/B
        AWNB=A*WNB(K)
        RWNB=R*WNB(K)
        CALL BESSEL(0,BWNB,BJ0B)
        CALL BESSEL(0,AWNB,BJ0A)
        CALL ANEUM(0,AWNB,BN0A)
        CALL ANEUM(0,BWNB,BN0B)
        CALL ANEUM(1,BWNB,BN1B)
        CALL ANEUM(1,RWNB,BN1R)
        CALL BESSEL(1,BWNB,BJ1B)
        CALL BESSEL(1,RWNB,BJ1R)
        ALPHB=R*(BJ0B*BN1R-BN0B*BJ1R)
        BETB(K)=B*(BJ0B*BN1B-BN0B*BJ1B)
        BAL=PI*(ALPHB*ALPHB-BETB(K)*BETB(K))
        PNB(K)=1.0D0/(DSQRT(BAL))
        QTERM(K)=BJ0B*BN0A-BN0B*BJ0A
        TPI=2.0D0*PI/ALAB
        AB(K,1)=DSQRT(TPI)*PNB(K)*QTERM(K)/WNB(K)
  5   CONTINUE
C
C
      DO 6 N=2,NMDB
        WNBB=WNB(N)
        QTERMM=QTERM(N)
        PNBB=PNB(N)
        BETBB=BETB(N)
        DO 7 J=2,NEXPF
```

```
          WNAA=WNA(J)
          WND=WNAA-WNBB
          ABSWND=DABS(WND)
          IF(ABSWND.LT.1.0D-06) GO TO 8
          AB(N,J)=-2.0D0*PI*PN(J)*PNBB*WNBB*ALPHA(J)*QTERMM*PI/
     *            (WNAA**2-WNBB**2)
          GO TO 7
    8     AB(N,J)=PI*PN(J)*PNBB*(BETBB*BETA(J)-ALPHA(J)*ALPHA(J))
    7   CONTINUE
    6 CONTINUE
C
C
      AMUOES=AMU0/EPSL0
      EITA0=DSQRT(AMUOES)
      E0M0=AMU0*EPSL0
      DO 9 M=1,NEXPF
        AI(M)=0.0D0
    9 CONTINUE
      AI(1)=2.0D0/EITA0
C
C ***************************************************************************
C * NOW WE START READING THE FREQUENCY AND MAGNITUDE AND PHASE OF *
C * THE REFLECTION COEFFICIENT S11.  THEN START COMPUTING THE     *
C * REAL AND IMAGINARY PARTS OF THE PERMEABILITY.                 *
C ***************************************************************************
C
      N=2
      DO 11 NF=1,NP
        READ(4,*) FREQ,RHOMAG,RHOPHS
        WRITE(6,*) 'FREQUENCY (GHZ)=',FREQ
        W=2.0D0*PI*FREQ*1.0D9
        RHOPHS=RHOPHS*PI/180.0D0
        RHOR=RHOMAG*DCOS(RHOPHS)
        RHOI=RHOMAG*DSIN(RHOPHS)
        CALL CALCYA(AA,NMDA,NEXPF,EITA0,W,E0M0,WNA,EPSL0,YA)
        CALL EPSMU(N,W,FMUR,FMUI,IER)
        WRITE(3,77) FREQ,FMUR,FMUI,IER
   77   FORMAT(F15.8,2(2X,1PE16.6),I4)
   11 CONTINUE
      STOP
      END
C
C ***************************************************************************
C * THIS SUBROUTINE CALCYA CALCULATES THE ENTREES OF THE YA MATRIX *
C * WHICH REPRESENTS THE TRANSMISSION LINE REGION                 *
C ***************************************************************************
C
      SUBROUTINE CALCYA(AA,NMDA,NEXPF,EITA0,W,E0M0,WNA,EPSL0,YA)
      IMPLICIT REAL*8 (A-H,O-Z)
      COMPLEX*16 YA(10,10),SUM,AKZN,AKZNSQ,EITAN(10)
```

```
      DIMENSION WNA(10),AA(10,10)
      DO 101 I=2,NMDA
        AKZCMX=W*W*E0M0-WNA(I)*WNA(I)
        AKZNSQ=DCMPLX(AKZCMX,0.0D0)
        AKZN=CDSQRT(AKZNSQ)
        EITAN(I)=AKZN/(W*EPSL0)
101   CONTINUE
      DO 102 I=1,NEXPF
        DO 103 J=1,NEXPF
          SUM=0.0D0
          DO 104 M=2,NMDA
            SUM=SUM+AA(M,I)*AA(M,J)/EITAN(M)
104       CONTINUE
          YA(I,J)=AA(1,I)*AA(1,J)/EITA0+SUM
103     CONTINUE
102   CONTINUE
      RETURN
      END
C
C ***************************************************************************
C * THIS SUBROUTINE CALCYB CALCULATES THE ENTREES OF THE YB MATRIX *
C * WHICH REPRESENTS THE CAVITY REGION. IT ALSO CALCULATES THE     *
C * TOTAL Y MATRIX.                                                *
C ***************************************************************************
C
      SUBROUTINE CALCYB(W,FMUR,FMUI,Y)
      IMPLICIT REAL*8 (A-H,O-Z)
      COMMON / BLOCK / WNB(25),AB(25,10),YA,RHOR,RHOI,D,
     *                 NEXPF,EPSL0,AMU0,EMUR,EMUI,FEPSR,FEPSI
      COMMON / BLK / NMDB
      COMPLEX*16 YB(10,10),SUM,AKZNB,EITANB,EITTAN(25),TANKNB,TANK0B
     *,AK0,EPMUCX,EPSJ,AK02,EITAB0,YA(10,10),Y(10,10),AK0D,AKZNBD,AKSQ
     *,AMU0EP,EITAB1,EPSCMX,AMUCMX
      EPSCMX=DCMPLX(FEPSR,-FEPSI)*EPSL0
      EPSJ=DCMPLX(FEPSI,FEPSR)*EPSL0
      AMUCMX=DCMPLX(FMUR,-FMUI)*AMU0
      EPMUCX=EPSCMX*AMUCMX
      AMU0EP=AMUCMX/EPSCMX
      EITAB1=CDSQRT(AMU0EP)
      REALE=DREAL(EITAB1)
      AIEIT=DIMAG(EITAB1)
      EITAB0=DCMPLX(AIEIT,-REALE)
      AK02=W*W*EPMUCX
      AK0=CDSQRT(AK02)
      AK0D=AK0*D
      TANK0B=CDSIN(AK0D)/CDCOS(AK0D)
C
      DO 2Q1 I=2,NMDB
        AKSQ=AK02-WNB(I)*WNB(I)
        AKZNB=CDSQRT(AKSQ)
```

```
        EITANB=AKZNB/(W*EPSJ)
        AKZNBD=AKZNB*D
        TANKNB=CDSIN(AKZNBD)/CDCOS(AKZNBD)
        EITTAN(I)=EITANB*TANKNB
201   CONTINUE
C
      DO 202 I=1,NEXPF
        DO 203 J=1,NEXPF
          SUM=0.0D0
          DO 204 M=2,NMDB
            SUM=SUM+AB(M,I)*AB(M,J)/EITTAN(M)
204       CONTINUE
          YB(I,J)=-(AB(1,I)*AB(1,J)/(EITAB0*TANK0B))-SUM
203     CONTINUE
202   CONTINUE
      DO 205 J=1,NEXPF
        DO 205 L=1,NEXPF
          Y(J,L)=YA(J,L)+YB(J,L)
205   CONTINUE
      RETURN
      END
C
C ***************************************************************************
C * THIS SUBROUTINE CALLS SUBROUTINE NONLIN TO SOLVE A NONLINEAR *
C * SYSTEM OF EQUATIONS TO YIELD THE COMPLEX PERMEABILITY.       *
C ***************************************************************************
C
      SUBROUTINE EPSMU(N,OMEGA,FMUR,FMUI,IER)
      IMPLICIT REAL*8(A-H,O-Z)
      COMPLEX*16 YA(10,10)
      COMMON / BLOCK / WNB(25),AB(25,10),YA,RHOR,RHOI,D,
     *                 NEXPF,EPSL0,AMU0,EMUR,EMUI,FEPSR,FEPSI
      DIMENSION X(2)
      X(1)=EMUR
      X(2)=EMUI
      N=2
      CALL NONLIN(OMEGA,N,6,30,2,X,1.0D-10,IER)
      FMUR=X(1)
      FMUI=X(2)
      RETURN
      END
C
C ***************************************************************
C * THIS SUBROUTINE, NONLIN, IMPLEMENTS BROWN'S METHOD TO *
C * SOLVE A SYSTEM OF N SIMULTANEOUS NONLINEAR EQUATIONS. *
C ***************************************************************
C
      SUBROUTINE NONLIN(W,N,NUMSIG,MAXIT,IPRINT,X,EPS,IER)
      IMPLICIT REAL*8 (A-H,O-Z)
      DIMENSION X(30),PART(30),TEMP(30),ISUB(30),LOOKUP(30,30)
```

```
     *          ,COE(30,31)
      DELTA=1.0D-7
      RELCON=10.0D0**(-NUMSIG)
      JTEST=1
      IF(IPRINT .EQ. 1) PRINT 48
  48  FORMAT(1H1)
      DO 700 M=1,MAXIT
        IQUIT=0
        FMAX=0.0D0
        M1=M-1
        IF (IPRINT .NE. 1) GO TO 9
        PRINT 49,M1,(X(I),I=1,N)
  49    FORMAT(I5,10E18.8)
   9    DO 10 J=1,N
  10    LOOKUP(1,J)=J
 C
        DO 500 K=1,N
          IF (K-1) 134,134,131
 131      KMIN=K-1
          CALL BACK (KMIN,N,X,ISUB,COE,LOOKUP)
 134      CALL FUN C (W,X,F,K)
          FMAX=DMAX1 (FMAX,DABS(F))
          IF (DABS(F) .GE. EPS) GO TO 1345
          IQUIT=IQUIT+1
          IF(IQUIT .NE. N) GO TO 1345
          GO TO 725
1345      FACTOR=0.001D0
 135      ITALLY=0
          DO 200 I=K,N
            ITEMP=LOOKUP(K,I)
            HOLD=X(ITEMP)
            PREC=5.0D-13
 C
            ETA=FACTOR*DABS(HOLD)
            H=DMIN1(FMAX,ETA)
            IF (H .LT. PREC) H=PRE C
            X(ITEMP)=HOLD+H
            IF(K-1) 161,161,151
 151        CALL BACK (KMIN,N,X,ISUB,COE,LOOKUP)
 161        CALL FUNC(W,X,FPLUS,K)
            PART(ITEMP)=(FPLUS-F)/H
            X(ITEMP)=HOLD
            IF(DABS(PART(ITEMP)) .LT. DELTA) GO TO 190
            IF(DABS(F/PART(ITEMP)) .LE. 1.0D15)GO TO 200
 190        ITALLY=ITALLY+1
 200      CONTINUE
          IF(ITALLY .LE. N-K) GO TO 202
          FACTOR=FACTOR*10.0D0
          IF (FACTOR .GT. 11.0D0) GO TO 775
          GO TO 135
```

```
202       IF(K .LT. N) GO TO 203
          IF(DABS(PART(ITEMP)) .LT. DELTA) GO TO 775
          COE(K,N+1)=0.0D0
          KMAX=ITEMP
          GO TO 500
C
203       KMAX=LOOKUP(K,K)
          DERMAX=DABS(PART(KMAX))
          KPLUS=K+1
          DO 210 I=KPLUS,N
            JSUB=LOOKUP(K,I)
            TEST=DABS(PART(JSUB))
            IF(TEST .LT. DERMAX) GO TO 209
            DERMAX=TEST
            LOOKUP(KPLUS,I)=KMAX
            KMAX=JSUB
            GO TO 210
209         LOOKUP(KPLUS,I)=JSUB
210       CONTINUE
          IF(DABS(PART(KMAX)) .EQ. 0.0D0) GO TO 775
C
          ISUB(K)=KMAX
          COE(K,N+1)=0.0D0
          DO 220 J=KPLUS,N
            JSUB=LOOKUP(KPLUS,J)
            COE(K,JSUB)=-PART(JSUB)/PART(KMAX)
            COE(K,N+1)=COE(K,N+1)+PART(JSUB)*X(JSUB)
220       CONTINUE
500     COE(K,N+1)=(COE(K,N+1)-F)/PART(KMAX)+X(KMAX)
C
        X(KMAX)=COE(N,N+1)
        IF (N .EQ. 1) GO TO 610
        CALL BACK(N-1,N,X,ISUB,COE,LOOKUP)
610     DO 630 I=1,N
          IF(DABS(TEMP(I)-X(I)) .GT. DABS(X(I))*RELCON) GO TO 649
630     CONTINUE
        JTEST=JTEST+1
        IF(JTEST-3) 650,725,725
649     JTEST=1
650     DO 660 I=1,N
660     TEMP(I)=X(I)
700   CONTINUE
      IER=1
      PRINT 1753
1753  FORMAT(/' NO CONVERGENCE. MAXIMUM NUMBER OF ITERATIONS USED.')
      IF(IPRINT .NE. 1) GO TO 800
      PRINT 1763
1763  FORMAT(/'FUNCTION VALUES AT THE LAST APPROXIMATION FOLLOW:'/)
      IFLAG=1
      GO TO 7777
```

```
 725  IER=0
      IF(IPRINT .NE. 1) GO TO 800
7777  DO 750 K=1,N
        CALL FUNC(W,X,PART(K),K)
 750  CONTINUE
      IF(IFLAG .NE. 1) GO TO 8777
      PRINT 7788,(PART(K),K=1,N)
7788  FORMAT(3E20.8)
      GO TO 800
8777  PRINT 751
 751  FORMAT(//' CONVERGENCE HAS BEEN ACHIEVED. THE FUNCTION VALUES')
      PRINT 7515,(PART(K),K=1,N)
7515  FORMAT(' AT THE FINAL APPROXIMATION FOLLOW:'//(3E20.8))
      GO TO 800
 775  IER=2
      PRINT 752
 752  FORMAT(//'MODIFIED JACOBIAN IS SINGULAR. TRY A DIFFERENT')
      PRINT 7525
7525  FORMAT('INITIAL APPROXIMATION')
 800  MAXIT=MAXIT
      RETURN
      END
 C
 C
 C
      SUBROUTINE BACK(KMIN,N,X,ISUB,COE,LOOKUP)
      IMPLICIT REAL*8 (A-H,O-Z)
      DIMENSION X(30),COE(30,31),ISUB(30),LOOKUP(30,30)
      DO 200 KK=1,KMIN
        KM=KMIN-KK+2
        KMAX=ISUB(KM-1)
        X(KMAX)=0.0D0
        DO 100 J=KM,N
          JSUB=LOOKUP(KM,J)
          X(KMAX)=X(KMAX)+COE(KM-1,JSUB)*X(JSUB)
 100    CONTINUE
        X(KMAX)=X(KMAX)+COE(KM-1,N+1)
 200  CONTINUE
      RETURN
      END
```

APPENDIX III

These Fortran subroutines are being called by both programs given in appendices I and II.

```
C
C ************************************************************
C * THIS SUBROUTINE, GAUSS, SOLVES SYSTEMS OF EQUATIONS      *
C * USING GAUSSIAN ELIMINATION AND COMPUTES ERROR BOUNDS     *
C ************************************************************
C
      SUBROUTINE GAUSS(N,A,B,X)
      IMPLICIT REAL*8(A-H,O-Z)
      COMPLEX*16 A(50,50),B(50),X(50),RES(50),AA(50,50)
      DIMENSION IPIVOT(50),IC(50)
      CALL FACTOR(A,N,AA,IPIVOT)
      CALL CONDNO(A,AA,N,IPIVOT,CNDN,IC,AINV)
      CALL SOLVE(AA,N,B,IPIVOT,X)
      DO 70 I=1,N
        RES(I)=0.0D0
70    CONTINUE
      DO 4 I=1,N
      DO 5 J=1,N
        RES(I)=RES(I)+A(I,J)*X(J)
5     CONTINUE
4     CONTINUE
      DO 6 I=1,N
        RES(I)=RES(I)-B(I)
6     CONTINUE
      ANORMR=0.0D0
      ANORMB=0.0D0
      DO 7 I=1,N
        ANORMB=ANORMB+CDABS(B(I))
        ANORMR=ANORMR+CDABS(RES(I))
7     CONTINUE
      RETURN
      END
```

```
C
C ***********************************************************
C * THIS SUBROUTINE, FACTOR, IS CALLED BY SUBROUTINE *
C * GAUSS TO PERFORM GAUSSIAN ELIMINATION            *
C ***********************************************************
C
      SUBROUTINE FACTOR(A,N,AA,IPIVOT)
      IMPLICIT REAL*8(A-H,O-Z)
      COMPLEX*16 A(50,50),AA(50,50),TR
      DIMENSION IPIVOT(50),D(50)
      DO 27 I=1,N
      DO 27 J=1,N
        AA(I,J)=A(I,J)
27    CONTINUE
      IS=N-1
      DO 29 IP=1,IS
        J=IP
        DO 20 I=IP,N
          AMAX=0.0D0
          DO 21 LJ=IP,N
            RAA=CDABS(AA(I,LJ))
            IF(RAA.GT.AMAX) AMAX=RAA
21        CONTINUE
          SAA=CDABS(AA(I,IP))
          D(I)=SAA/AMAX
20      CONTINUE
        BMAX=0.0D0
        DO 22 I=IP,N
          IF(D(I).LE.BMAX) GO TO 22
          BMAX=D(I)
          J=I
22      CONTINUE
        IPIVOT(IP)=J
        DO 23 I=IP,N
          TR=AA(IP,I)
          AA(IP,I)=AA(J,I)
          AA(J,I)=TR
23      CONTINUE
        NP=IP+1
        DO 25 J=NP,N
          AA(J,IP)=-AA(J,IP)/AA(IP,IP)
        DO 25 I=NP,N
            AA(J,I)=AA(J,I)+AA(J,IP)*AA(IP,I)
25      CONTINUE
29    CONTINUE
      RETURN
      END
```

```
C
C ***************************************************************
C * THIS SUBROUTINE, SOLVE, IMPLEMENTS THE BACK SUBSTITUTION *
C * STEP IN SOLVING THE LINEAR SYSTEM OF EQUATIONS           *
C ***************************************************************
C
      SUBROUTINE SOLVE(AA,N,B,IPIVOT,X)
      IMPLICIT REAL*8(A-H,O-Z)
      COMPLEX*16 AA(50,50),X(50),B(50),SB(50),BT,SUM
      DIMENSION IPIVOT(50)
      DO 130 LL=1,N
        SB(LL)=B(LL)
130   CONTINUE
      MM=N-1
      DO 40 I=1,MM
        J=IPIVOT(I)
        BT=SB(I)
        SB(I)=SB(J)
        SB(J)=BT
        KK=I+1
        DO 41 K=KK,N
          SB(K)=SB(K)+AA(K,I)*SB(I)
41      CONTINUE
40    CONTINUE
      X(N)=SB(N)/AA(N,N)
      DO 42 I=2,N
        SUM=0.0D0
        II=N+1-I
        IJ=II+1
        DO 43 J=IJ,N
          SUM=SUM+AA(II,J)*X(J)
43      CONTINUE
        X(II)=(SB(II)-SUM)/AA(II,II)
42    CONTINUE
      RETURN
      END
```

```
C
C ****************************************
C * THIS SUBROUTINE, CONDNO, COMPUTES *
C * THE CONDITION NUMBER OF A MATRIX  *
C ****************************************
C
      SUBROUTINE CONDNO(A,AA,N,IPIVOT,CNDN,IC,AINV)
      IMPLICIT REAL*8(A-H,O-Z)
      COMPLEX*16 A(50,50),AA(50,50),Z(50),
     *Y(50),XX(50),SUM,ZT
      DIMENSION IPIVOT(50),IC(50)
      IC(1)=1
      Z(1)=1.DO/AA(1,1)
      DO 50 I=2,N
        SUM=0.0DO
        IJ=I-1
        DO 51 J=1,IJ
          SUM=SUM+AA(J,I)*Z(J)
51      CONTINUE
        IF(CDABS(SUM).EQ.0.DO) THEN
          IC(I)=1
        ELSE
          IC(I)=-SUM/CDABS(SUM)
        ENDIF
        Z(I)=(IC(I)-SUM)/AA(I,I)
50    CONTINUE
      KN=N-1
      DO 52 I=1,KN
        II=N-I
        IJ=II+1
        DO 53 K=IJ,N
          Z(II)=Z(II)+AA(K,II)*Z(K)
53      CONTINUE
        J=IPIVOT(II)
        ZT=Z(II)
        Z(II)=Z(J)
        Z(J)=ZT
52    CONTINUE
      CALL SOLVE(AA,N,Z,IPIVOT,XX)
      ANORMX=0.0DO
      ANORMY=0.0DO
      DO 54 I=1,N
        ANORMX=ANORMX+CDABS(XX(I))
        ANORMY=ANORMY+CDABS(Z(I))
54    CONTINUE
      AINV=ANORMX/ANORMY
      ANORMA=0.0DO
      DO 55 I=1,N
        SUMR=0.0DO
        DO 56 J=1,N
```

```
          SUMR=SUMR+CDABS(A(J,I))
56      CONTINUE
        IF(SUMR.GT.ANORMA) ANORMA=SUMR
55    CONTINUE
      CNDN=ANORMA*AINV
      RETURN
      END
```

```
C
C ***********************************************************
C * THIS SUBROUTINE, ZEROS, COMPUTES THE SOLUTIONS OF *
C * THE STANDARD EQUATION (4.16) GIVEN IN CHAPTER IV  *
C ***********************************************************
C
      SUBROUTINE ZEROS(I,R,H,ROOT)
      IMPLICIT REAL*8(A-H,O-Z)
      EXTERNAL BSNM
      COMMON /B1/  C
      PI=DARCOS(-1.D0)
      TOL=1.D-12
      C=R/H
      ROOT=DSQRT(I*I*PI*PI/((C-1.D0)*(C-1.D0))-1.D0/((C+1)*(C+1)))
      XN=ROOT-.2D0
      XP=ROOT+.2D0
      CALL BISECT(XN,XP,BSNM,ANS,TOL)
      ROOT=ANS
      RETURN
      END
C
C
      SUBROUTINE BISECT(A,B,F,ROOT,TOL)
      IMPLICIT REAL*8(A-H,O-Z)
      COMMON /B1/  C
      FA=F(A)
1     HALF=(A+B)/2.D0
      FM=F(HALF)
      IF(FA*FM.LE.0.D0) GOTO 2
      A=HALF
      FA=FM
      GO TO 3
2     B=HALF
3     IF((B-A).LE.TOL) GO TO 4
      GO TO 1
4     ROOT=(A+B)/2.D0
      RETURN
      END
C
      FUNCTION BSNM(X)
      IMPLICIT REAL*8(A-H,O-Z)
      COMMON /B1/  C
      CALL BESSEL(0,X,TJ0)
      ARG=C*X
      CALL BESSEL(0,ARG,TJX)
      CALL ANEUM(0,X,TN0)
      CALL ANEUM(0,ARG,TNX)
      BSNM=TJX*TN0-TNX*TJ0
      RETURN
      END
```

```
C
C ********************************************************
C * THIS SUBROUTINE, BESSEL, COMPUTES THE ZEROTH OR  *
C * FIRST ORDER BESSEL FUNCTION OF THE FIRST KIND.   *
C ********************************************************
C
      SUBROUTINE BESSEL(NORD,ARG,VALJ)
      IMPLICIT REAL*8(A-H,O-Z)
      IF(ARG.GT.20.D0) THEN
        X=3.D0/ARG
        IF(NORD.EQ.0) THEN
          F0=.79788456D0-.00000077D0*X-.0055274D0*X*X-.00009512D0*(X**3)
     *       +.00137237D0*(X**4)-.00072805D0*(X**5)+.00014476D0*(X**6)
          TH0=ARG-.78539816D0-.04166397D0*X-.00003954D0*X*X
     *       +.00262573D0*(X**3)-.00054125D0*(X**4)-.00029333D0*(X**5)
     *       +.00013558D0*(X**6)
          VALJ=F0*DCOS(TH0)/DSQRT(ARG)
          RETURN
        ENDIF
         IF(NORD.EQ.1) THEN
         F1=.79788456D0+.00000156D0*X+.01659667D0*X*X+.00017105D0*(X**3)
     *       -.00249511D0*(X**4)+.00113653D0*(X**5)-.00020033D0*(X**6)
          TH1=ARG-2.35619449D0+.12499612D0*X+.00005650D0*X*X
     *       -.00637879D0*(X**3)+.00074348D0*(X**4)+.00079824D0*(X**5)
     *       -.00029166D0*(X**6)
          VALJ=F1*DCOS(TH1)/DSQRT(ARG)
          RETURN
        ENDIF
      ELSE
      FT=(ARG/2.D0)**NORD
      SUM=0.D0
      DO 1 I=1,100
        J=I-1
        JNORD=J+NORD
        F11=(-ARG/2.D0)**J
        F12=(ARG/2.D0)**J
        RIF=1.D0
        RIMFAC=1.D0
        IF(J.EQ.0) GO TO 3
        DO 2 K=1,J
          RIF=RIF*K
2       CONTINUE
3       IF(NORD.NE.0) GO TO 4
        RIMFAC=RIF
        GO TO 6
4       DO 5 K=1,JNORD
          RIMFAC=RIMFAC*K
5       CONTINUE
6       F2=(F11/RIF)*(F12/RIMFAC)
        IF(DABS(F2).LE.1.D-10) GO TO 7
```

```
        SUM=SUM+F2
1     CONTINUE
      IF(DABS(F2).GT.1.D-10) WRITE(7,8) F2
8     FORMAT(/,5X,'DESIRED ACCURACY IN CALCULATING A BESSEL FUNCTION
     *IS NOT OBTAINED.  THE LAST TERM OF THE SERIES ADDED =',F15.8)
7     VALJ=FT*SUM
      ENDIF
      RETURN
      END
```

```
C
C ********************************************************
C * THIS SUBROUTINE, ANEUM, COMPUTES THE ZEROTH OR  *
C * FIRST ORDER BESSEL FUNCTION OF THE SECOND KIND. *
C ********************************************************
C
      SUBROUTINE ANEUM(NORDER,ARG,VALN)
      IMPLICIT REAL*8(A-H,O-Z)
      IF(ARG.GT.20.D0) THEN
        X=3.D0/ARG
        IF(NORDER.EQ.0) THEN
          F0=.79788456D0-.00000077D0*X-.0055274D0*X*X-.00009512D0*(X**3)
     *       +.00137237D0*(X**4)-.00072805D0*(X**5)+.00014476D0*(X**6)
          TH0=ARG-.78539816D0-.04166397D0*X-.00003954D0*X*X
     *       +.00262573D0*(X**3)-.00054125D0*(X**4)-.00029333D0*(X**5)
     *       +.00013558D0*(X**6)
          VALN=F0*DSIN(TH0)/DSQRT(ARG)
          RETURN
        ENDIF
         IF(NORDER.EQ.1) THEN
         F1=.79788456D0+.00000156D0*X+.01659667D0*X*X+.00017105D0*(X**3)
     *       -.00249511D0*(X**4)+.00113653D0*(X**5)-.00020033D0*(X**6)
          TH1=ARG-2.35619449D0+.12499612D0*X+.00005650D0*X*X
     *       -.00637879D0*(X**3)+.00074348D0*(X**4)+.00079824D0*(X**5)
     *       -.00029166D0*(X**6)
          VALN=F1*DSIN(TH1)/DSQRT(ARG)
          RETURN
        ENDIF
      ELSE
      PI=DARCOS(-1.D0)
      GAMMA=0.5772156649D0
      CALL BESSEL(0,ARG,VALJ0)
      ARLG=ARG/2.0
      C=2.D0*DLOG(ARLG)/PI
      C1=2.D0*GAMMA/PI
      FT0=(C+C1)*VALJ0
      CALL BESSEL(1,ARG,VALJ1)
      FT1=(C+C1)*VALJ1
      SUM1=0.D0
      SUM2=0.D0
      DSUM1=0.D0
      DSUM2=0.D0
      AFACQ=1.D0
      AFACQ1=1.D0
      DO 14 I=1,100
        AFACQ=AFACQ*FLOAT(I)
        AI2=2.D0*FLOAT(I)
        AN1=((-1)**I)*(ARG**I)
        DSUM1=DSUM1+1.D0/FLOAT(I)
        TTQ=2.D0**AI2
```

```
      TER1=(AN1/AFACQ)*(DSUM1/(AFACQ*TTQ))*(ARG**I)
      SUM1=SUM1+TER1
      AFACQ1=AFACQ*(FLOAT(I)+1.D0)
      DSUM2=2.D0*DSUM1+1.D0/(FLOAT(I)+1.D0)
      TTQ1=TTQ*2.D0
      TER2=(AN1/AFACQ)*(DSUM2/(AFACQ1*TTQ1))*ARG*(ARG**I)
      IF(DABS(TER1).LE.1.D-10.AND.DABS(TER2).LE.1.D-10) GO TO 15
      SUM2=SUM2+TER2
14    CONTINUE
      IF(DABS(TER1).GT.1.D-10.OR.DABS(TER2).GT.1.D-10)
     *WRITE(7,16) TER1,TER2
16    FORMAT(/,5X,'DESIRED ACCURACY IN CALCULATING NEUMANN FUNCTIONS
     *IS NOT OBTAINED.  THE LAST TERMS OF THE SERIES ADDED =',2F15.8)
15    VALN0=FT0-2.D0*SUM1/PI
      VALN1=FT1-(ARG/2.D0+SUM2)/PI-2.D0/(PI*ARG)
      ENDIF
      IF(NORDER.EQ.0) GO TO 1
      IF(NORDER.EQ.1) GO TO 2
      IF(NORDER.EQ.-1) GO TO 3
      NEG=NORDER
      IF(NEG.LT.0) NEG=-NEG
      T1=VALN0
      T2=VALN1
      DO 4 I=2,NEG
        I1=I-1
        T3=2.D0*I1*T2/ARG-T1
        T1=T2
        T2=T3
4     CONTINUE
      VALN=T3
      IF(NORDER.LT.0) VALN=VALN*((-1)**NEG)
      GO TO 7
1     VALN=VALN0
      GO TO 7
2     VALN=VALN1
      GO TO 7
3     VALN=-VALN1
7     RETURN
      END
```

BIBLIOGRAPHY

1. Weir, W. B.,"Automatic Measurement of Complex Dielectric Constant and Permeability at Microwave Frequencies," Proc. IEEE, Vol. 62, No. 1, pp. 33-36, 1974.

2. Ramo, S. and Whinnery, J., "Fields and Waves in Modern Radio," 2nd. ed., New York, Wiley, ch. 8, 1953.

3. Barry, W.,"A Broad-Band, Automated, Stripline Technique for the Simultaneous Measurement of Complex Permittivity and Permeability," IEEE Trans. Mic. Th. Tech., Vol. MTT-34, No. 1, pp. 80-84, 1986.

4. Rado, G. T.,"Magnetic Spectra of Ferrites," Reviews of Modern Physics, Vol. 25, No. 1, pp. 81-89, 1953.

5. Nicolson, A. M., and Ross, G. F.,"Measurement of the Intrinsic Properties of Materials by Time-Domain Techniques," IEEE Trans. Inst. Meas., Vol. IM-19, No. 4, pp. 377-382, 1970.

6. Courtney, W. E.,"Analysis and Evaluation of a Method of Measuring the Complex Permittivity and Permeability of Microwave Insulators," IEEE Trans. Mic. Th. Tech., Vol. MTT-18, No. 8, pp. 476-485, 1970.

7. Ahmed, M. et. al.,"Wideband Characterization and Modeling of Thick-Film Printed Components," ISHM 85 Proceedings, pp. 99-106, 1985.

8. Elshabini-Riad, A. et. al.,"Wideband Characterization and Modeling of Thick-Film Inductors," ISHM 87 Proceedings, pp. 73-78, 1987.

9. Polder, D.,"Ferrite Materials," Proceedings of IEE, Vol. 97, No. II, pp. 246-256, 1950.

10. Rado, G. et. al.,"Ferromagnetism at Very High Frequencies. III. Two Mechanisms of Dispersion in a Ferrite," Physical Review, Vol. 80, No. 2, pp. 273-280, 1950.

11. Waldron, R. A.,"Perturbation Theory of Resonant Cavities," Proceedings of IEE, pt. C, Vol. 107, pp. 272-274, 1960.

12. Afsar, M. N. et. al.,"The measurement of the Properties of Materials," Proceedings of IEEE, Vol. 74, No. 1, pp. 183-199, 1986.

13. Josyulu, O. S. et. al.,"A Method for the Evaluation of Dielectric Parameters of Solids at Microwave Frequencies," J. Phys. E Sci. Instrum., Vol. 15, pp. 318-321, 1982.

14. Miles, P. A. et. al.,"Dielctric Spectroscopy of Ferromagnetic Semiconductors," Rev. of Modern Phys., Vol. 29, No. 3, pp. 279-307, 1957.

15. Lax, B. and Button, K. J., "Microwave Ferrites and Ferrimagnetics," McGraw-Hill Book Co., Inc., New York, 1962.

16. Baden-Fuller, A. J., "Ferrites at Microwave Frequencies," Peter Peregrinus Ltd., London, 1987.

17. Smit, J. and Wijn, H. P., "Ferrites," John Wiley & Sons, New York, 1959.

18. Smit, J., "Magnetic Properties of Materials," McGraw-Hill Book Co., Inc., New York, 1971.

19. Barnwell, P.,"Thick Film Inductors at VHF," Electronic Components, Vol. 12, No. 5, pp. 681-684, 1970.

20. Barnwell, P.,"Thick Film Inductors and Their Use in Tuned Circuits at VHF," Electronic Components, Vol. 12, No. 11, pp. 749-758, 1971.

21. Corkhill, J. and Martin, M.,"Thick Film Filter Designed for Television Signals," Electronic Engineering Journal, Vol. 43, No. 519, pp. 65-69, 1971.

22. Barnwell, P.,"100 MHz Tuned Amplifier with Thick Film Inductors," Electronic Components, Vol. 14, No. 15, pp. 723-724, 1972.

23. Williamson, G.,"Micro-Inductors and Transformers for RF Use," Electron, pp. 16-21, 1976.

24. Olschewski, W.,"The Hybrid Compatible Transformers," IEEE Trans. Comp., Hyb., and Manuf. Tech. (CHMT), Vol CHMT-2, No. 4, pp. 487-489, December 1979.

25. Elshabini-Riad, A., et al,"Improved Properties of Thick Film Inductors Using Ferromagnetic Pastes," Proc. of the 1987 Electronic components Conf., pp. 214-219, May 1987.

26. Hewlett-Packard Co.,"Time Domain Reflectometry," Application Note AN62, 1964.

27. Riad, S. M. and Nahman, N.,"Applications of the Homomorphic Transformation to Time Domain Measurement Problems," NBSIR 78-881: National Bureau of Standards, Boulder, Co., June 1978.

28. Toscano, J. C., "Wideband Characterization of Thick Film Inductors", M.Sc. Thesis, Virginia Polytechnic Institute and State University, 1988.

29. Saed, M. A., "Dielectric Characterization Using a Wideband Dielectric Filled Cavity," Ph.D. Dissertation, Virginia Polytechnic Institute and State University, November 1987.

30. Harrington, R. F., "Field Computation by Moment Methods," Macmillan Company, New York, 1968.

31. Harrington, R. F., "Time Harmonic Electromagnetic Fields," McGraw Hill, 1961.

32. Waldron, R. A., "Theory of Guided Electromagnetic Waves," Van Nostrand Reinhold Company Ltd., London, 1969.

33. Brown, K. M., "Computer Oriented Algorithms for Solving Systems of Simultaneous Nonlinear Algebraic Equations," In "Numerical Solution of Systems of Nonlinear Algebraic Equations", Edited by Bryne, G. D. and Hall, C. A., Academic Press, pp. 281-348, 1973.

34. Riad, S. M.,"The Deconvolution Problem: an Overview," Proceedings of the IEEE, Vol. 74, No. 1, pp. 896-898, January 1986.

35. Shaarawi, A. M. and Riad, S. M.,"Computing the Complete FFT of a Step-Like Waveform," IEEE Trans. on Inst. and Meas., Vol IM-35, No. 1, March 1986.

The vita has been removed from the scanned document